

ABSTRACT

TURNER, CHRISTOFFER HEATH. Computer Simulation of Chemical Reactions in Porous Materials. (Under the direction of Keith E. Gubbins.)

Understanding reactions in nanoporous materials from a purely experimental perspective is a difficult task. Measuring the chemical composition of a reacting system within a catalytic material is usually only accomplished through indirect methods, and it is usually impossible to distinguish between true chemical equilibrium and metastable states. In addition, measuring molecular orientation or distribution profiles within porous systems is not easily accomplished. However, molecular simulation techniques are well-suited to these challenges. With appropriate simulation techniques and realistic molecular models, it is possible to validate the dominant physical and chemical forces controlling nanoscale reactivity. Novel nanostructured catalysts and supports can be designed, optimized, and tested using high-performance computing and advanced modeling techniques in order to guide the search for next-generation catalysts - setting new targets for the materials synthesis community.

We have simulated the conversion of several different equilibrium-limited reactions within microporous carbons and we find that the pore size, pore geometry, and surface chemistry are important factors for determining the reaction yield. The equilibrium-limited reactions that we have modeled include nitric oxide dimerization, ammonia synthesis, and the esterification of acetic acid, all of which show yield enhancements within microporous carbons. In conjunction with a yield enhancement of the esterification reaction, selective adsorption of

ethyl acetate within carbon micropores demonstrates an efficient method for product recovery.

Additionally, a new method has been developed for simulating reaction kinetics within porous materials and other heterogeneous environments. The validity of this technique is first demonstrated by reproducing the kinetics of hydrogen iodide decomposition in the gas phase, and then predictions are made within slit-shaped carbon pores and carbon nanotubes. The rate constant is found to increase by a factor of 47 in carbon nanotubes, as compared to the same reaction in the bulk gas phase. Overall, the results of these simulation studies demonstrate improvements in chemical reaction yield and chemical kinetics that are possible by understanding the nature of confined reactions, and applying this knowledge to catalyst design.

**COMPUTER SIMULATION OF CHEMICAL REACTIONS IN POROUS
MATERIALS**

by

CHRISTOFFER HEATH TURNER

A thesis submitted to the Graduate Faculty
of North Carolina State University in partial
fulfillment of the requirements for the
Degree of Doctor of Philosophy

CHEMICAL ENGINEERING

Raleigh

2002

APPROVED BY:

Keith E. Gubbins, Chair

Carol K. Hall

Gregory N. Parsons

George W. Roberts

BIOGRAPHY

Heath Turner was born in Birmingham, Alabama on November 15, 1973 to parents Gary and Cheryl Turner. Heath was raised in Birmingham, along with an older brother Bart and a younger sister Tiffany, and graduated from Mountain Brook High School in 1992.

After graduating from high school, Heath attended Auburn University in Auburn, Alabama to study chemical engineering, with a focus in biochemical engineering. While an undergraduate student, he was an intern in Monsanto's R&D Department in Decatur, Alabama, working with dyed acrylic fibers. In December of 1996, Heath graduated summa cum laude with a Bachelor of Science degree in chemical engineering from Auburn University. After a seven month position with Birmingham Steel, Heath began graduate school in the Fall of 1997 in the Chemical Engineering Department at North Carolina State University in Raleigh, North Carolina. While at NC State, Heath met his future wife, Christy Ann Smith, who was then a graduate student in the Industrial Engineering Department at NC State. They were married in Birmingham, Alabama on June 2, 2001 at Brookwood Baptist Church. After completing graduate school, Heath accepted a position with Trinity Consultants in Atlanta, Georgia.

ACKNOWLEDGMENTS

I would like to begin by thanking my wife, Christy, for her support, patience, and encouragement during my education. She has made my life enjoyable and fun, even when research wears me down. Most importantly, she has kept me well-fed day and night.

My parents also deserve much appreciation for their help. They have emphasized the importance of learning throughout my life, and have helped support me financially and otherwise, while I have been in school. I value my education second only to the things they have taught me.

My experience at NC State would not have been nearly as enjoyable or as enlightening without the diverse group of people that I have had the privilege to work with: Lev Gelb, Simon McGrother, Karl Travis, Ravi Radhakrishnan, Ken Thomson, Sandra Gavalda, Jorge Pikunic, Philip Llewellyn, Martin Lisal, John Brennan, Lauriane Scanu, Flor Siperstein, Alberto Striolo, Henry Bock, Coray Colina, Francisco Hung, Supriyo Bhattacharya, and Naresh Chennamsetty. I would especially like to thank Karl Travis for helping me work out my simulation kinks in the beginning, and John Brennan for many helpful discussions and manuscript editing along the way.

I would also like to thank several people outside of my research group that I have been able to work with. Jerry Whitten has given me a great deal of help and advice with quantum mechanical calculations. Also, I would like to thank Karl Johnson for the thoughtful criticisms and suggestions throughout my research. I have also been fortunate enough to discuss the experimental work related to my project with Katsumi Kaneko, Malgorzata Sliwinska-Bartkowiak, and John Yates. Additionally, I would like to thank Sandeep Tripathi and Walter Chapman for sharing their insights and knowledge.

Finally, I would like to thank my advisor, Keith Gubbins, and the rest of my thesis committee for their help and guidance. Keith has a talent for balancing many tasks, while at the same time maintaining a high standard of quality. He has done a great job of exposing me to a broad range of research, and he has provided me with many opportunities. Most of all, I will always be grateful to Keith for keeping my research experience enjoyable.

TABLE OF CONTENTS

LIST OF TABLES	vii
LIST OF FIGURES	viii
1. INTRODUCTION	1
1.1 Motivation	1
1.2 Defining the Research Agenda	4
1.3 Available Simulation Methods	6
1.4 Simulating Chemical Reaction Equilibria	9
1.5 Simulating Chemical Reaction Kinetics	18
1.6 Overview of our Work	28
References	30
2. NITRIC OXIDE DIMERIZATION	36
2.1 Introduction	36
2.2 Simulation Methods	39
2.3 Simulation Models	44
2.4 Results and Discussion	48
2.5 Conclusions	56
References	59
3. AMMONIA SYNTHESIS	76
3.1 Introduction	76
3.2 Simulation Methods	77

3.3 Simulation Models	83
3.4 Results and Discussion	88
3.5 Conclusions	100
References	103
4. ESTERIFICATION OF ACETIC ACID	122
4.1 Introduction	122
4.2 Simulation Methods	126
4.3 Simulation Models	130
4.4 Simulation Results	136
4.5 Conclusions	145
References	147
5. EFFECT OF CONFINEMENT ON REACTION KINETICS	162
5.1 Introduction	162
5.2 Methodology	165
5.3 Verification of the TS-RxMC Method	176
5.4 Effects of Strong Intermolecular Forces and Confinement	183
5.5 Discussion and Conclusions	189
References	193
6. CONCLUSIONS	206
6.1 Reaction Equilibria	206
6.2 Reaction Kinetics	207

LIST OF TABLES

CHAPTER 2

2.1 Summary of Lennard-Jones parameters.....	45
2.2 Conversion of nitric oxide dimerization in the bulk gas phase.....	54

CHAPTER 3

3.1 Summary of intermolecular potential parameters.....	84
3.2 Summary of potential parameters for –COOH sites.....	86
3.3 Adsorbate density within slit-pores at a pressure of 100 bar.....	91
3.4 Selectivity of N ₂ over H ₂ in a 0.83 nm wide pore at 573 K.....	93
3.5 Ammonia mole fraction corresponding to Figure 3.11.....	94

CHAPTER 4

4.1 Summary of intermolecular potential parameters.....	131
4.2 Coefficients for the intramolecular potentials.....	132
4.3 Rotation and vibrational constants used in the partition functions.....	134
4.4 Experimental yield of ethyl acetate in activated carbon.....	141
4.5 Yield of ethyl acetate at 473.15 K and 523.15 K.....	144

CHAPTER 5

5.1 Intermolecular parameters for the $2\text{HI} \leftrightarrow (\text{HI})_2^\ddagger \rightarrow \text{H}_2 + \text{I}_2$ reaction.....	177
5.2 Solvent parameters corresponding to the site-site LJ potential.....	184

LIST OF FIGURES

CHAPTER 1

1.1 Molecular Simulation Scales.....	35
--------------------------------------	----

CHAPTER 2

2.1 Snapshot of the (10,10) carbon nanotube bundle, without defects.....	62
2.2 Snapshot of the (10,10) carbon nanotube bundle, with 5% defects.....	63
2.3 Conversion of NO dimerization in the bulk saturated liquid.....	64
2.4 Conversion of NO dimerization within slit-shaped carbon pores.....	65
2.5 Potential energy profile of NO within slit-pores.....	66
2.6 Density profiles of NO and (NO) ₂ in the slit pore, H/σ _{NO} = 5.50.....	67
2.7 Density profiles of NO and (NO) ₂ in the slit-pore, H/σ _{NO} = 2.50.....	68
2.8 Effect of bulk gas pressure on the adsorption and reaction equilibrium..	69
2.9 Conversion of NO dimerization within slit-shaped pores from DFT.....	70
2.10 Conversion of NO dimerization in the perfect (10,10) nanotubes.....	71
2.11 Snapshots in (10,10) nanotubes at different loadings.....	72
2.12 Snapshots in (10,10) nanotubes with different separation distances.....	73
2.13 Conversion of NO dimerization in the defective (10,10) nanotubes.....	74
2.14 Adsorbate density within the (10,10) nanotubes during reaction.....	75

CHAPTER 3

3.1 Structure of the –COOH activation site used in simulation.....	105
3.2 Snapshot of the coconut shell carbon model.....	106

3.3 Radial distribution function of the coconut shell carbon model.....	107
3.4 Hexagonal packing of the carbon nanotubes used in simulation.....	108
3.5 Mole fraction of NH ₃ for the bulk phase reaction.....	109
3.6 Mole fraction of NH ₃ for the bulk phase reaction with inert gases.....	110
3.7 Nitrogen adsorption isotherm at 303 K in activated carbon fibers.....	111
3.8 Hydrogen adsorption isotherm at 293 K in AX21 carbon.....	112
3.9 Simulations of ammonia synthesis in carbon slit-pores.....	113
3.10 Conversion of ammonia synthesis at 573 K and 100 bar.....	114
3.11 Ammonia synthesis in carbon slit-pores with varying N ₂ :H ₂ ratios.....	115
3.12 Pore size distribution of the coconut shell carbon model.....	116
3.13 Snapshot of a carbon slit-pore, chemically activated by –COOH.....	117
3.14 Conversion of NH ₃ in chemically activated slit-pores ($H=1.6$ nm).....	118
3.15 Conversion of NH ₃ in chemically activated slit-pores ($H=1.0$ nm).....	119
3.16 Snapshot of ammonia synthesis in a chemically activated slit-pore.....	120
3.17 Conversion of NH ₃ in carbon nanotube bundles.....	121

CHAPTER 4

4.1 Conversion of acetic acid to ethyl acetate in the bulk gas phase.....	151
4.2 Smooth slit-pore and activated slit-pore models.....	152
4.3 Conversion of acetic acid to ethyl acetate in 90 mole % CO ₂	153
4.4 Snapshot of esterification in 90% CO ₂ at 450 K.....	154
4.5 Snapshot of esterification in 90% CO ₂ at 360 K.....	155
4.6 CO ₂ clustering during esterification at 360 K.....	156

4.7 Mole fraction of ethyl acetate in activated and unactivated carbon slit-pores.....	157
4.8 Total mole fraction of ethyl acetate in the two-phase system (bulk + pore) composed of a bulk gas phase and a carbon slit-pore (unactivated).....	158
4.9 Total mole fraction of ethyl acetate in the two-phase system (bulk + pore) composed of a bulk gas phase and a carbon slit-pore (activated).....	159
4.10 Total conversion of acetic acid in a pore width $H=2.0$ nm.....	160
4.11 Snapshot of esterification within the activated pore.....	161

CHAPTER 5

5.1 Structure of the $(\text{HI})_2^\ddagger$ transition state.....	195
5.2 TS-RxMC simulations for HI decomposition at 573.15 K.....	196
5.3 TS-RxMC simulations for HI decomposition at 594.55 K.....	197
5.4 Comparison of simulations with Eckert and Boudart.....	198
5.5 Equilibrium constant of the HI decomposition reaction at 573.15 K.....	199
5.6 Effect of adjusting the activation barrier for H_2 exchange reaction.....	200
5.7 Effect of adjusting the activation barrier for HI decomposition.....	201
5.8 TS-RxMC simulations of HI decomposition in inert solvents.....	202
5.9 TS-RxMC simulations of HI decomposition in carbon slit-pores.....	203
5.10 HI decomposition rate versus density in the bulk and in the pore.....	204
5.11 TS-RxMC simulations of HI decomposition in carbon nanotubes.....	205

CHAPTER 1

Introduction

1.1 Motivation

The research that we present is motivated by the need to understand reactions that are altered by strong intermolecular forces, such as reactions at high pressures, reactions in inert solvents, and most importantly, reactions occurring within microporous materials. There is a great deal of interest from a practical standpoint to understand the molecular level interactions and forces that dictate macroscopic level phenomena such as reactant selectivity, reaction conversion, and the kinetic properties of reacting systems. Knowledgeable design of porous catalysts and catalyst support materials can result in increased conversions, higher reaction rates, higher product selectivity, and many derivative environmental benefits.

There have been several recent examples from the literature demonstrating the role of strong intermolecular forces on chemical reactions. Regan and coworkers [1] have used both experiment and the RRKM (Rice-Ramsperger-Kassel-Marcus) statistical rate theory [2] to study the differing reaction rates in the gas phase and in solution for S_N2 reactions. The authors find that the activation barrier and reaction rate both change due to differential solvation of the transition state for the reactions in solution.

Another recent contribution [3] in this area has examined the effects of geometric confinement on the creation of self-assembled monolayers (SAMs) on gold surfaces. During a process that the authors term "nanografting", it is found that the development of thiol-derived SAMs are favored in the geometrically confined space between an atomic force microscopy (AFM) tip and a gold surface. It is suggested that spatial confinement between the surface and the AFM tip alters the mechanism and kinetics of the surface reactions by preventing alternative reaction pathways and stabilizing particular transition states or reaction intermediates. In addition, the authors find that the SAMs created at the tip of the AFM tend to be free of defects, in contrast to SAMs formed in otherwise unconstrained environments.

In another related area, Brunet has recently reviewed [4] applications of using confinement to determine the stereochemical outcome of a reaction through space constriction and molecular close contact, thus providing an alternative method for enantiomeric separation. In this work, Brunet reviews several potential methodologies for confinement-induced asymmetric induction of chemical reactions. One of these techniques is called molecular imprinting, which strives to imprint orifices within polymeric matrices having structures that mimic the transition state of enantioselective processes. This potentially lowers the activation barrier for a selected enantiomer and increases the selectivity. Another route to asymmetric induction is the development of temporary microscopic chiral molecular capsules or vessels with a complementary structure specific to the reactants [5,6]. It is envisioned that temporary confinement of pro-chiral reactants within these structures might lead to the production of nonracemic mixtures in solution. There is also the avenue of enclosing chiral

auxiliaries and pro-chiral molecules within cationic pores of zeolites in order to induce diastereoselectivity. It has been shown that confinement within the orifices of zeolites can dramatically enhance the transfer of chirality as compared to an unconfined system [7]. The last methodology reviewed [4] is the possibility of constructing hybrid organic-inorganic materials, and using the cavities within these frameworks as catalytic points for enantioselective reactions. The performance of these hybrid materials for enantioselective catalysis is still being evaluated.

The effects of confinement on other chemical reactions have also been studied on more fundamental levels, such as with hybrid density functional theory. Halls and Schlegel [8] have recently studied the Menshutkin S_N2 reaction within (8,0) and (9,0) carbon nanotubes, and find significant lowering of the activation energy and the reaction endothermicity as compared to the bulk gas phase. The reaction path for the Menshutkin S_N2 reaction involves an intermediate with a distinct separation of charge, and the formation of this intermediate is favored within the (8,0) and (9,0) carbon nanotubes due to their large polarizabilities. Additionally, it is found that similar activation energy lowering will occur near surfaces of planar graphite, and this effect tends to become more pronounced as the distance from the graphitic sheet decreases. It is suggested by the authors [8] that any reaction in which there is a large separation of charge along the reaction coordinate may be enhanced inside these fullerene-based materials due to their large polarizabilities.

The above examples clearly demonstrate the importance of understanding the phenomena contributing to reactivity in microscopically constrained environments. We have attempted to contribute to this area by expanding the understanding of chemical reaction equilibria and chemical reaction kinetics using molecular-level simulations. The next section will explain the specific focus that we have adopted for our work.

1.2 Defining the Research Agenda

The above examples demonstrate the significant effects and potential benefits for conducting chemical reactions in confined systems. We have attempted to contribute to this broad area, by again addressing the following question: how does the surrounding environment, and in particular, confinement within porous materials, influence a chemical reaction? In order to differentiate our investigation from previous studies, it is helpful to identify the most important questions that will define the scope of our project:

- (a) How does the equilibrium conversion of a reaction within a porous material compare to the same reaction in the bulk gas phase, at a given temperature and pressure of the bulk phase?
- (b) Does the selectivity of reactant and product molecules in a pore affect the conversion of a reaction?
- (c) Are the pore geometry or the pore dimensions important factors when trying to determine the extent of reaction in a pore?

- (d) Can the surface chemistry within a pore be modified in order to shift the equilibrium of the reacting system?
- (e) How is the heat of reaction affected within a porous material as compared to the bulk gas phase?
- (f) How are reaction rates influenced by the surrounding environment, such as inert solvents or confinement within porous materials?
- (g) Can the geometry of a micropore affect the kinetics of a chemical reaction?

Since we are primarily interested in learning about the fundamental nature of reactions within porous materials and other non-ideal environments, we start with simple reactions within well-defined pore structures having simple surface chemistries. While this research is intended to influence and shape the understanding of realistic reacting systems, an experimental investigation of this nature can produce ambiguous results. In experimental studies there are inevitable complications arising from competing side reactions, long-lived metastable states, uncertainties arising from the micropore characterization, uncertainties in determining the mean compositions and composition profiles in the pores, etc. Simulation methods allow precise control of these variables and determination of the true thermodynamic equilibrium state, and detailed measurements of the reaction can be easily performed. The next few sections lay the foundation for the main simulation tools that we have used in our studies of reaction equilibrium and kinetics.

1.3 Available Simulation Methods

Once it is apparent that simulations are best suited to this type of investigation, it is then necessary to decide which types of simulations to employ. The answers to the previous questions can be investigated from several different perspectives and length scales: quantum mechanical simulations, Monte Carlo (MC) simulations, molecular dynamics (MD), finite element simulations, all the way up to continuum approximations. There are unfortunate tradeoffs between accuracy and efficiency as the focus shifts from the quantum mechanical level all the way up to the continuum level. This is shown quantitatively in Figure 1.1, which illustrates the length and time scales accessible with each computational method. This Figure was constructed assuming that computations are performed for a maximum of one week on the Blue Horizon (SP3) supercomputer located at the San Diego Supercomputer Center (SDSC), which has a maximum speed of 1.728 Tflops (1 Tflop = 1×10^{12} floating point operations per second). As more approximations are introduced into the computational methods, the length and time scales accessible grow exponentially.

In general, we have addressed our previous list of questions from a semi-classical standpoint, while still incorporating perspectives and information from separate but related quantum mechanical studies. We have chosen this level of approximation since we are primarily interested in studying the influence of “physical” forces on chemical reactions. This differs from the majority of research on catalysis, which has focused on the “chemical” interaction of molecules with a catalyst surface. For the present discussion, it is convenient to refer to these “chemical” interactions as forces that are strong enough to change the electronic

structure of the atoms and molecules involved, and must be studied with quantum mechanical techniques.

However, in supported catalysis we anticipate a further significant effect of confinement on the reaction rate, due to the finite size and reduced dimensionality of the adsorbed phase, and to the strong interactions of the reacting species with the pore walls. We refer to these latter interactions (repulsion, dispersion, electrostatic, etc.) as "physical" forces to distinguish them from the chemical interactions with the catalyst itself. For these reasons, we have elected to use semi-classical Monte Carlo methods. This level of approximation allows us to simulate realistic molecular systems composed of millions of molecules, yet still accurately capture the physical effects on chemical reactions which we wish to understand.

By performing Monte Carlo simulations and accumulating statistical averages of the system, we can accurately measure quantities such as the number of molecules of various species adsorbed in a pore, the heats of adsorption, the density, the molecular arrangement within the pores, etc. We begin by assuming that a given system maintains a Boltzmann distribution of states. Then by applying the rules of statistical mechanics, an arbitrary observable system property $\langle A \rangle$ may be calculated according to the following equation:

$$\langle A \rangle = \frac{\int d\mathbf{r}^N \exp[-\beta U(\mathbf{r}^N)] A(\mathbf{r}^N)}{\int d\mathbf{r}^N \exp[-\beta U(\mathbf{r}^N)]} \quad (1.1)$$

In Eq. (1.1), $\mathbf{b}=1/k_{\text{B}}T$ is the reciprocal of the Boltzmann constant times the temperature, and U is the configurational energy of the system, which depends on the coordinates, $\mathbf{r}^N=\mathbf{r}_1 \mathbf{r}_2 \dots \mathbf{r}_N$, of the N molecules in the system. Although it is usually not possible to solve Eq. (1.1) analytically, it can be statistically approximated as an average over randomly generated system configurations, according to:

$$\langle A \rangle \approx \frac{\sum_{t=1}^{t=t_{\text{max}}} A(\mathbf{t}) \exp[-\mathbf{b}U(\mathbf{t})]}{\sum_{t=1}^{t=t_{\text{max}}} \exp[-\mathbf{b}U(\mathbf{t})]} \quad (1.2)$$

By generating many different system configurations, \mathbf{t} , and sampling the average value of the property $\langle A \rangle$ at each of these configurations, an accurate estimate of the integral, and thus the equilibrium value of A can be obtained. However, in practice it turns out that only a small number of randomly generated configurations make non-negligible contributions to the average, due to highly energetic overlaps encountered between the molecules in the system. Thus, the utility of the Monte Carlo method hinges on various algorithms to efficiently sample the most probable configurations for a given system.

The generation of trial configurations important to chemically reacting systems provides an excellent example of applying these Monte Carlo sampling techniques. Since bond breaking and bond formation between molecules involves high potential energy barriers, sampling techniques, such as the ones described in the following section, must be applied in order to

explore the most significant contributions to ensemble averages. The following sections give brief reviews of the development and application of Monte Carlo methods for predicting chemical reaction equilibria and kinetics in environments where intermolecular interactions are significant. For our applications, the simulations must be flexible enough to allow us to look at reactions between individual molecules, reactions occurring in multiple phases, and reactions in which the number of moles changes.

1.4 Simulating Chemical Reaction Equilibria

1.4.1 Available Methods

While the bond breaking and bond formations associated with forward and reverse reaction steps are statistically inaccessible in a typical Monte Carlo search, in 1981 Coker and Watts devised one of the first simulation methods which was able to deal with this challenge [9,10]. Their technique was based on grand canonical Monte Carlo (constant chemical potential, volume, and temperature), but was modified to directly sample forward and reverse reaction steps. Thus the high-energy process of bond breaking and bond formation is circumvented by directly simulating the equilibrium between the reactants and the final products. The total number of molecules was held fixed in their simulations, but the identities of the individual molecules were allowed to vary. However, in order to sample these identity changes, the chemical potential differences between the two species had to be specified. Coker and Watts used their method to simulate the equilibrium conversion of the reaction:



Their simulated mole fractions were found to agree closely with experimental measurements, within the small temperature range that they investigated. However, in addition to requiring the chemical potentials as a necessary input, their method was restricted to chemical reactions that preserve the total number of moles in the system.

In 1988, Kofke and Glandt proposed an improved simulation technique to model both reaction equilibria and phase equilibria [11]. They termed their new method the semigrand canonical ensemble MC method, and used it to study the same reaction as Coker and Watts, Eq. (1.3). This method was more versatile and corrected some of the errors in the method of Coker and Watts, such as mistakes in the equilibrium constant, the acceptance criteria, and an incorrect form of Widom's particle insertion method [12]. The semigrand ensemble samples forward and reverse reactions by using the ratios of the component fugacities to a reference fugacity in the acceptance criterion, instead of using chemical potentials. While this method was an improvement over the method of Coker and Watts, its application was still restricted to reactions in which the number of moles remained fixed.

Soon after Kofke and Glandt's work, Shaw devised a new simulation technique [13] to simulate chemical reaction equilibria that eliminated the requirement of specifying the chemical potentials or chemical potential difference between the reacting species. Shaw named the new technique the $N_{\text{atoms}}^{\text{PT}}$ ensemble, and applied it to the reaction:



Shaw's method was a significant improvement over previous methods, primarily because simulations could be performed in the more convenient isothermal-isobaric ensemble. Chemical equilibrium along with other thermodynamic quantities could be measured at constant pressure, temperature and total number of atoms, which allowed more natural comparison with experiments. In the $N_{\text{atoms}}PT$ ensemble, the acceptance criteria for the forward and reverse reaction steps involves only the ideal gas partition functions for the reaction components, and the method can, in principle, accommodate reactions that involve a change in the number of moles. However, due to its cumbersome nature, there have been no applications of this method to reactions that change in mole number.

In the years following Shaw's contribution, several new techniques were introduced which dealt with chemical reaction equilibria by biasing moves through configuration space to areas that are significant for chemical bond formation and breakage, instead of the direct sampling methods employed in the previously mentioned techniques. Instead of the random particle displacements included in traditional Metropolis Monte Carlo simulations, these techniques bias displacements towards areas of phase space which are significant for associations (i.e., the close approach of two molecules). One of these methods was named association biased Monte Carlo (ABMC) and was developed by Busch *et al.* [14,15]. This method was based on the work of Kranendonk and Frenkel [16]. ABMC was first applied to particles with one bonding site, which only allowed dimer molecules to form. The method was later extended

to accommodate particles with multiple binding sites that form higher order complexes. Their primary focus was studying antigen-antibody interactions. While the ABMC method efficiently samples the important regions of phase space, the calculations necessary for the biasing can become quite complicated.

Tsangaris and de Pablo developed a method that they named bond-bias Monte Carlo (BBMC) [17]. Similar to the ABMC method, their technique also biased Monte Carlo moves into areas of phase space significant to bond breaking and bond formation. The BBMC technique therefore avoids the high-energy activation barrier usually associated with strong associations and efficiently samples phase space. With BBMC simulations, Tsangaris and de Pablo studied the phase equilibria and energetics of acetic acid dimerization, Eq. (1.5), and achieved close agreement with experimental data and theoretical predictions.



However, defining the regions of phase space to explore is dependent on the specific system. Due to the sampling technique used in BBMC, small displacements and reorientations must be made to bonded complexes, which then limits the ability of the bonded species to explore phase space. In addition, the BBMC method is restricted to open systems such as the grand canonical or Gibbs ensemble.

Another Monte Carlo method was developed by Shew and Mills to simulate systems that involve high energy barrier crossings, such as chemical reactions [18-20]. Their method was named the subspace sampling method (SSM), and it works by partitioning configuration space into regions which are separated by potential energy barriers or by different hamiltonians. While they began with studies in one dimension [18,20], they later applied their method to simulate the thermodynamic and structural properties of a weak electrolyte solution in three-dimensional space [19]. Although reasonable results can be obtained with this method, an adjustable simulation parameter must be optimized in order to achieve convergence rates comparable with other methods.

The most powerful and flexible technique for simulating molecular reaction equilibria to date was developed simultaneously by two separate groups, Smith and Triska [21] and Johnson *et al.* [22], which we collectively refer to throughout this work as the Reactive Monte Carlo (RxMC) simulation method. The two methods are similar to the one developed by Shaw [13], except that the method can be easily applied to reactions that change in mole number. Additionally, multiple simultaneous reactions can easily be studied, as can reactions in multiple phases, and reactions within porous materials. Both renditions of this method [21,22] simulate reaction equilibria through trial attempts of complete forward and reverse reaction steps (in addition to the traditional Metropolis Monte Carlo moves), while conserving the total number of atoms in the system. Although the simulation technique of the two groups is virtually identical, the acceptance probability for a reaction step is formulated by Johnson and coworkers in terms of the molecular partition functions, while the

acceptance probability for a reaction step is formulated by Smith and Triska in terms of the Gibbs free energy of reaction. Consequently, the two methods are interchangeable, as the Gibbs free energy of reaction can be easily formulated in terms of the molecular partition functions.

1.4.2 Recent Applications of Reactive Monte Carlo

Aside from the research presented in the following chapters of this work, there have only been a few applications of the RxMC simulation technique. The first application of the RxMC method to a realistic molecular reaction was performed by Johnson et al. [22] in order to study the dimerization of nitric oxide in both the gas and liquid phases:



The equilibrium conversion of this reaction was simulated along the saturation line for the liquid phase through a temperature range of 110 K to 170 K, and the extent of dimerization was found to compare closely with both experiment [23] and theory [24]. The reaction shows a high degree of dimerization in the liquid phase, while the gas phase is almost entirely composed of monomers. Additionally, it was found that the simulation predictions were quite sensitive to the dimerization binding energy, D_0 , which is used in the Monte Carlo acceptance criteria for the forward and reverse reaction steps.

Subsequently, Lisal *et al.* published a series of papers applying the RxMC method (therein referred to as the reaction ensemble method) to realistic molecular reactions [25-27] and to complex phase equilibria [28,29]. Although chemical reactions are not considered in references [28] and [29], phase equilibrium is treated as a special case of chemical equilibrium. According to this treatment, the Gibbs ensemble technique is combined with the RxMC moves in order to predict accurate phase behavior of complex binary mixtures involving water, methanol, ethanol, carbon dioxide, isobutene, MTBE, and n-butane.

The first realistic reaction that this group studied was the equilibrium of the bromine-chlorine system, Eq. (1.3). This reaction has been modeled previously using other simulation methods, such as that of Coker and Watts [9,10] for a study of the liquid phase conversion and by Kofke and Glandt [11] for a study of simultaneous reaction and phase equilibrium. Lisal *et al.* [25] expanded upon the work of these previous studies to map out the complete simultaneous reaction and phase equilibrium diagram of the bromine-chlorine system. Their agreement with previous simulation and experimental results was good, and they were able to contribute additional information about this system where experimental data is inaccessible (due to the chemical instability of the system).

The second application of RxMC simulations by Lisal *et al.* [27] was to high temperature chemically reacting plasmas, in which the ionization reactions of helium were modeled:





These simultaneously occurring ionization reactions were studied at high temperatures (up to 100,000 K) and high pressures (10, 100, and 400 MPa), and the equilibrium results were compared with predictions from the classical Debye-Hückel (DH) macroscopic model [30]. The authors calculate the composition of the plasma, molar enthalpies, molar volumes, molar heat capacities, and coefficients of cubic expansion for this system. The predictions from the DH theory tend to slightly underpredict the amount of ionization in the plasma as the pressure is increased. Additionally, the DH predictions tend to be least accurate when calculating the coefficient of cubic expansion and the molar heat capacity, by up to 40% at the highest pressure (400 MPa).

The most recent contribution from Lisal *et al.* [26], is an extension of the RxMC method to constant enthalpy and constant internal energy simulations. The utility of this approach is demonstrated by simulating the conversion of ammonia synthesis within an adiabatic plug flow reactor. The enthalpy corresponding to the inlet composition, a stoichiometric feed of H₂ and N₂, is first calculated. Then, this value is used to perform a RxMC simulation at constant enthalpy and pressure to determine the exit composition and temperature.

Brennan and Rice have used RxMC to study the shock properties of liquid NO and liquid N₂ [31]. RxMC simulations were carried out at high pressures (2-90 GPa) and high temperatures (500-13,000K) and the shock properties of these systems were determined.

Excellent agreement was found with experimental measurements at these conditions. The RxMC method shows great promise in the development of novel energetic materials, in testing current detonation theories, and in furthering our understanding of materials under shock.

Reactive Monte Carlo simulations have also been used to study [32] the ammonia synthesis reaction at conditions characteristic of the deep atmosphere of Jupiter (temperatures between 500 and 2300 K and at pressures up to 10,000 bar):



In order to compare with experiments, simulations were also performed at 573 K and 873 K and in pressure ranges where experimental data is available (100 to 1,000 bar), and close agreement was found with the available data. We have performed similar simulations of the ammonia synthesis reaction, which will be presented later in Chapter 3 of this work.

With the exception of our work, we only know of one other application of the RxMC method to specifically study a reaction confined within a micropore. Borówko and Zagórski [33] have studied a simple dimerization reaction in slit-like pores, with A-type and B-type molecules assigned different Lennard-Jones diameters (σ) for the potential energy calculation:



(1.10)

They use the Reactive Monte Carlo method for their simulations, but they arbitrarily allow the ideal gas contribution of the equilibrium constant to vary with respect to distance from the pore walls. This is a quantity that we have not allowed to vary in our work for a given reaction. They find that the bulk phase composition favors the creation of B molecules at higher densities, according to LeChatlier's Principle, as the forward reaction results in a reduction in the number of moles. This effect is magnified within the pore phase, as the confinement tends to show an increased conversion due to preferential solvation within the adsorptive pore (in cases when the equilibrium constant is held fixed). When the equilibrium constant is allowed to vary, the confinement within the pore has a mixed effect on the reaction conversion, depending on the relative effects of the adsorption and the surface-mediated changes allowed in the equilibrium constant.

1.5 Simulating Chemical Reaction Kinetics

1.5.1 Available Methods

In addition to studying the equilibrium yield of chemical reactions in non-ideal environments, we are also interested in how kinetics can be influenced by these same environments. There are several different theories and simulation methods that are able to incorporate the physical interactions with the surrounding environment into the prediction of rate constants. In order to review the progress in this area, it is convenient to segregate these methods along the different applicable length scales, as depicted in Figure 1.1. This should

help give some perspective to the method that we have developed [34] and to the systems and forces that we are able to study with our method, which will be discussed in Chapter 5.

A. Continuum Methods

Starting with general expressions used for reaction rate constants at the highest level of approximation should give justification for the more fundamental research performed on the smaller length scales, such as our own. As an example, the rate (r_A) for an elementary binary chemical reaction, $A+B\rightarrow C$, can be expressed in terms of the reactant concentrations and a rate constant (k_{obs}), and this rate “constant” is typically assumed to only depend on the temperature according to Eq. (1.12):

$$r_A = \frac{d[A]}{dt} = k_{obs}[A][B] \quad (1.11)$$

$$k_{obs}(T) = A \exp(E_a/RT) \quad (1.12)$$

In Eq. (1.11) and (1.12) k_{obs} is the observed rate constant, where brackets denote the concentration of each species, t is time, A is the preexponential factor, E_a is the activation energy, and R is the gas constant. These two expressions can be easily incorporated into engineering design equations for stirred-tank reactors, plug flow reactors, batch, semi-batch, etc. in order to describe the spatial or temporal rate of a chemical reaction.

While determining the initial concentrations in Eq. (1.11) is a fairly routine measurement, predicting the rate constant for a reaction is not as simple, especially when the conditions of

the surrounding environment, the solvent, or the catalyst change. In order to quantify the change of a rate constant with respect to the environment, it is imperative to incorporate more details into the model than the simple temperature-dependent Arrhenius expression shown in Eq. (1.12). For example, additional expressions, such as Eq. (1.13) are available [35,36] which are able to roughly model the pressure dependence of rate constants:

$$\left(\frac{\partial \ln k_{obs}}{\partial P} \right) = \frac{-\Delta V^\ddagger}{RT} \quad (1.13)$$

In the above equation, P is the pressure and ΔV^\ddagger is the effective volume difference between the reactants and an assumed transition state. This estimate is based on the transition state theory method [37] and predicts that if the transition state for the reaction has a smaller effective volume than the reactants, then the reaction rate constant will increase with the pressure of the system. This is not generally applicable to a wide range of conditions, and the value for ΔV^\ddagger is not known *a priori* but must be inferred from experiments or calculated using quantum mechanical simulations. Little insight is gained from merely knowing the activation volume, since many sources contribute to its value, such as bond breaking, bond formation, charge creation, etc. There exist other approximations as well on this (continuum) length scale, which account for the change in the reaction rate with respect to the surrounding phase in an approximate way [38].

B. Classical Simulations

In order to more accurately predict the rate constant in non-ideal environments, it is necessary to increase the amount of detail in the model. Within the context of transition state theory (TST) [37,39], the interactions with the environment can be accounted for in simulation by calculating the free energy of solvation (ΔG_{sol}^\ddagger) of a reaction. The free energy of solvation can then be added to the free energy of activation for the reaction in the ideal gas phase (ΔG_{gas}^\ddagger) in order to account for the overall free energy of activation in the solvent (or other medium). The resulting expression for the rate constant is shown below, and reflects the strong dependence on the free energy of activation, ΔG^\ddagger , where $\Delta G^\ddagger = \Delta G_{sol}^\ddagger + \Delta G_{gas}^\ddagger$:

$$k_{obs} = \mathbf{k} \frac{k_B T}{h} \exp(-\Delta G^\ddagger / k_B T) \quad (1.14)$$

In the equation above, \mathbf{k} is the transmission coefficient, h is Planck's constant, and k_B is the Boltzmann constant. The transmission coefficient (\mathbf{k}) accounts for any recrossing of the activation barrier, and will have a value of less than one if recrossing is significant.

The contribution of Lim *et al.* [40] gives a nice review of the equilibrium solvation methods for calculating the overall free energy of activation. As a first approximation, the free energy of solvation can be calculated in simulation by treating the solvent as a continuum, or more rigorously, by treating the solvent molecules explicitly. The continuum models can either be treated classically as with generalized Born models [41,42], or the continuum can be treated

quantum mechanically, as with self-consistent reaction field (SCRF) methods. If the molecular details of the solvent are included, which may be important for hydrogen bonding systems or other systems that have specific interactions, Monte Carlo or molecular dynamics simulations can be used to calculate the free energies in such molecular fluids.

Other solvation methods are also available within classical MC and MD simulations, which accumulate the probability of observing the extent of a predefined reaction coordinate. For instance, in the dissociation of HCl, the statistical elongation of the H-Cl bond distance in a simulation can be related to the free energy of dissociation in different environments.

However, unless the potential energy associated with changes in the reaction coordinate is small ($<5k_B T$), biasing methods such as umbrella sampling [43] must be used to accumulate accurate statistics.

Another approach on this same level of molecular detail is the free energy perturbation (FEP) method [44]. This method relates the change in free energy ΔG between two different systems A and B in terms of potential energy differences ($\langle dU_{A@B} \rangle$), as shown in Eq. (1.15), where the brackets denote ensemble averages.

$$\Delta G(A \rightarrow B) = -k_B T \ln \langle -\langle dU_{A \rightarrow B} \rangle / k_B T \rangle \quad (1.15)$$

To use the FEP method to calculate a rate constant, the reaction can again be modeled according to transition state theory. State A is assigned as the reactant state and state B is

assigned as the transition state for the reaction, and the free energy change for the formation of the transition state can be computed in a variety of non-ideal environments. If the two states (*A* and *B*) are not similar, then the convergence of the method will be slow. To avoid slow convergence, the transformation between the reactants and the transition state can be discretized into intermediate structures between the two states. The free energy difference of each incremental step can then be calculated in simulation and summed to give the total change in free energy from state *A* to state *B*.

Using molecular dynamics simulations, it is also possible to compute rate constants using time correlation functions [45]. A dividing surface or reaction coordinate can be defined in the simulation which separates reactant species from product species. Then, the net flux through this dividing surface can be measured in simulation during a given length of time, and this flux (calculated using time correlation functions) can then be related to a rate constant. If the activation barrier is high, simulations can incorporate constraint molecular dynamics in order to observe the barrier crossing. The Bennett-Chandler approach [46-48], uses this general framework for calculating rate constants. However, a suitable reaction coordinate must be pre-defined in the Bennett-Chandler approach in order to generate accurate statistics, and this approach gives poor results when the transmission coefficient (\mathbf{k}) is low. An alternative route for employing the general time correlation formalism is using the transition path ensemble, which was recently developed by Chandler and coworkers [49]. However, unlike the Bennett-Chandler approach, the reaction coordinate is not pre-defined, but is found during the course of the simulation by sampling different possible reaction

trajectories. The reaction path ensemble can explicitly account for external forces, such as solvation effects, in identifying the transition state structure for a reaction. Further review and application of these two methods are discussed by Frenkel and Smit [43]. Quantum mechanical analogues of the time correlation technique also exist [50,51].

There are several ways to refine the rate constants determined from the above equilibrium solvation methods. First of all, corrections can be included to account for dynamic collision effects or frictional effects that might alter the rate constant. These effects are not specifically included in the equilibrium solvation methods, but can be approximated separately and absorbed into the transmission coefficient, k , shown in Eq. (1.14). The analytical theory of Kramers [52,53] and the transmission coefficient of Grote and Hynes [54] are fairly well established for accommodating these effects. A discussion of these methods and others for approximating the transmission coefficient is presented by Ruiz-Montero *et al.* [55]. Also, since external interactions can affect the free energy of activation, there is a form of transition state theory that varies the definition of the activated configuration (*i.e.*, transition state species) in order to minimize the rate constant. This widely-accepted approach, called variational transition state theory (VTST) [56-59], tends to give more accurate values of the rate constant.

There are additional methods to improve the values of the rate constant, but in order to do so, it is necessary to increase the level of detail, and study reactions on a much smaller length scale. These methods are discussed in the next section.

C. Quantum Mechanical Simulations

While the methods described in the previous section are primarily classical methods, many of the molecular quantities and parameters used in these methods are taken directly from quantum mechanical simulations. The quantum mechanical simulations are performed on a much smaller length scale, which limits the size and time scale of the simulations to a few hundred atoms and to a few picoseconds, but detailed information about the transition state geometry, quantum mechanical tunneling, energy barriers, etc. can all be calculated. This is extremely important to the calculation of rate constants since this type of information is either difficult or impossible to measure with experiments.

Both *ab initio* methods and density functional theory (DFT) methods are capable of generating potential energy surfaces (PES), which are routinely used as input in classical MC and MD simulations for calculating rate constants. The calculation of a PES is usually attempted in order to identify a transition state species, which is defined to correspond to the maximum in the free energy during the course of a reaction. The observation of the transition state in the quantum mechanical simulations can normally be verified by observing a single imaginary frequency in one of the normal vibrational modes. Once a possible transition state has been observed, it can be confirmed to be the correct transition state by examining the normal mode corresponding to the imaginary frequency [60]. The motion in the normal mode should tend to deform the transition structure as expected, and this motion should connect reactants and products on the two sides of the potential barrier. Once the

transition state is identified, the necessary parameters such as the activation energy and the transition state geometry can be calculated.

In addition to developing PES's, several quantum mechanical methods, similar to the classical methods described above, are available for estimating rate constants in the presence of external interactions. For instance, Miller *et al.* [50,51] have developed a quantum mechanical analog for implementing the time correlation function approach for calculating rate constants. Additionally, there is the quantized version of variation TST, which is reviewed by Truhlar *et al.* [61] and applications of which are demonstrated in ref. [62,63]. This is similar to the classical version, which varies the definition of the dividing surface to minimize the rate constant. Also, there is a path integral formulation of quantum TST [64], which can be applied to reactions in solution and has been reviewed by Voth [65,66]. Applications of these methods as well as other quantum mechanical approaches to reaction rates can be found in the ref. [61]. In order to refine predictions of rate constants, there is a quantum mechanical analog of the classical Kramers and Grote-Hynes theories, which was first derived by Wolynes [67], and can account for quantum mechanical tunneling through the activation barrier or non-classical reflection above the barrier.

Probably one of the most recent and most popular quantum mechanical methods for calculating rate constants in the presence of surrounding molecules is called the Car-Parrinello method [68]. This is a molecular dynamics type approach for estimating kinetics, coupled with DFT to account for the motion of the electrons. The primary difference

between this method and other quantum mechanical methods is that a special technique is used to propagate the molecular orbitals. Instead of reoptimizing the orbitals at each step, the orbitals are assigned a fictitious mass and propagated along with the atomic nuclei. This maintains the orbitals on the ground-state (Born-Oppenheimer) surface in an efficient way and reduces the computational demands of the method. The main drawback of the Car-Parrinello method is that it is still limited to small systems (of the order of 100 atoms), similar to other quantum mechanical methods. Applications of this method to reactions in solution, at surfaces, and for biological processes have been recently reviewed by Trout [69].

1.5.2 Integration of RxMC Simulations with Transition State Theory

Since we are primarily concerned with the physical interactions, such as confinement within porous materials, on chemical reaction kinetics, we have primarily used semi-classical methods to study rate constants. Although we have adopted a semi-classical simulation approach to our project, much of the information about the transition state and the activation energy for the reaction must be gathered from separate studies at the quantum mechanical level.

In order to address our questions about the change of the rate constant in different physical environments, we have developed a simple technique, which combines the TST quasi-equilibrium hypothesis [37,39] with Reactive Monte Carlo [22] simulations. We are able to perform these simulations in heterogeneous environments, with simulation scales on the

order of 10^6 atoms, and achieve close agreement where experimental comparison is available. Our methodology is described in detail in Chapter 5, as well as applications of this method to the kinetics of hydrogen iodide decomposition in a variety of non-ideal environments.

1.6 Overview of Our Work

1.6.1 Equilibrium Studies

From the survey given in Section 1.4, it is clear that little work on confined reactions has been reported. In the following chapters, we will present our simulation results for several realistic systems. While the work of Borówko and Zagórski [33] and other contributions [70-77] give some insight into confined chemical reactions by studying simple, idealized reactions and associations, we have chosen to model more realistic reactions using detailed micropore models. We have chosen to model several systems, which we believe explore a range of chemical reaction phenomena. We begin by looking at the dimerization of nitric oxide in activated carbon fibers and in carbon nanotubes. Next, we model the ammonia synthesis reaction within several different microporous carbon models, as there has been recent interest in catalyzing this reaction within porous carbons. We then look at the esterification of acetic acid in both microporous carbons and in a supercritical CO₂ solvent.

1.6.2 Kinetic Studies

There have been many quantum mechanical studies examining the effects of solvents and surfaces on reaction kinetics. However, there have been few, if any, molecular level studies of the effects of porous confinement on chemical reaction rates. The last part of our work

focuses on this relatively unexplored effect, as we combine RxMC simulations within the framework of transition state theory. We demonstrate the validity of our new technique by studying the hydrogen iodide decomposition reaction within carbon slit pores and carbon nanotubes as an example.

References

- [1] C. K. Regan, S. L. Craig, and J. I. Brauman, *Science* **295** (2002), 2245.
- [2] Gardiner, Jr. W. C., *Rates and Mechanisms of Chemical Reactions*, W. A. Benjamin: New York, (1969).
- [3] S. Xu, P. E. Laibinis, and G. Liu, *Journal of the American Chemical Society* **120** (1998), 9356.
- [4] E. Brunet, *Chirality* **14** (2002), 135.
- [5] J. Kang and J. Rebek, *Nature* **382** (1996), 239.
- [6] Y. Tokunaga and J. Rebek, *Journal of the American Chemical Society* **120** (1998), 66.
- [7] S. Jayaraman, S. Uppili, A. Natarajan, A. Joy, K. C. W. Chong, M. R. Newton, A. Zenova, J. R. Scheer, and V. Ramamurthy, *Tetrahedron Letters* **41** (2000), 8231.
- [8] M. D. Halls and H. B. Schlegel, *Journal of Physical Chemistry B* **106** (2002), 1921.
- [9] D. F. Coker and R. O. Watts, *Chemical Physics Letters* **78** (1981), 333.
- [10] D. F. Coker and R. O. Watts, *Molecular Physics* **44** (1981), 1303.
- [11] D. A. Kofke and E. D. Glandt, *Molecular Physics* **64** (1988), 1105.
- [12] B. Widom, *Journal of Chemical Physics* **39** (1963), 2808.
- [13] M. S. Shaw, *Journal of Chemical Physics* **94** (1991), 7550.
- [14] N. A. Busch, M. S. Wertheim, Y. C. Chiew, and M. L. Yarmush, *Journal of Chemical Physics* **101** (1994), 3147.
- [15] N. A. Busch, M. S. Wertheim, and M. L. Yarmush, *Journal of Chemical Physics* **104** (1996), 3962.
- [16] W. G. T. Kranendonk and D. Frenkel, *Molecular Physics* **64** (1988), 403.
- [17] D. M. Tsangaris and J. J. de Pablo, *Journal of Chemical Physics* **101** (1994), 1477.
- [18] C.-Y. Shew and P. Mills, *Journal of Physical Chemistry* **97** (1993), 13824.
- [19] C.-Y. Shew and P. Mills, *Journal of Physical Chemistry* **99** (1995), 12988.
- [20] C.-Y. Shew and P. Mills, *Journal of Physical Chemistry* **99** (1995), 12980.

- [21] W. R. Smith and B. Triska, *Journal of Chemical Physics* **100** (1994), 3019.
- [22] J. K. Johnson, A. Z. Panagiotopoulos, and K. E. Gubbins, *Molecular Physics* **81** (1994), 717.
- [23] A. L. Smith and H. L. Johnston, *Journal of the American Chemical Society* **74** (1952), 4696.
- [24] Guedes, H. J. R., Thermodynamic properties of simple liquid systems, PhD Thesis, Universidade Nova de Lisboa, Portugal, (1988).
- [25] M. Lisal, I. Nezbeda, and W. R. Smith, *Journal of Chemical Physics* **110** (1999), 8597.
- [26] W. R. Smith and M. Lisal, *Physical Review E* (2002, in press).
- [27] M. Lisal, W. R. Smith, and I. Nezbeda, *Journal of Chemical Physics* **113** (2000), 4885.
- [28] M. Lisal, W. R. Smith, and I. Nezbeda, *Journal of Physical Chemistry B* **103** (1999), 10496.
- [29] M. Lisal, W. R. Smith, and I. Nezbeda, *Fluid Phase Equilibria* **181** (2001), 127.
- [30] Boulos, M. I., Fauchais, P., and Pfender, E., *Thermal Plasmas: Fundamentals and Applications*, Plenum: New York, (1994).
- [31] J. K. Brennan and B. M. Rice, *Physical Review E* (2002, in press).
- [32] L. E. S. de Souza and U. K. Deiters, *Physical Chemistry Chemical Physics* **1** (1999), 4069.
- [33] M. Borówko and R. Zagórski, *Journal of Chemical Physics* **114** (2001), 5397.
- [34] C. H. Turner, J. K. Brennan, J. K. Johnson, and K. E. Gubbins, *Journal of Chemical Physics* **116** (2002), 2138.
- [35] M. G. Evans, *Transactions of the Faraday Society* **34** (1938), 49.
- [36] Moore, J. W. and Pearson, R. G., *Kinetics and Mechanism*, Wiley-Interscience: New York, (1981).
- [37] M. G. Evans and M. Polanyi, *Transactions of the Faraday Society* **31** (1935), 875.
- [38] C. A. Eckert and M. Boudart, *Chemical Engineering Science* **18** (1963), 144.
- [39] H. Eyring, *Journal of Chemical Physics* **3** (1935), 107.

- [40] Lim, D., Jenson, C., Perasky, M. P., and Jorgensen, W. L. Transition State Modeling for Catalysis, edited by Truhlar, D. G. and Morokuma, K., Oxford (1999), 74-85.
- [41] C. J. Cramer and D. G. Truhlar, *Reviews in Computational Chemistry* **6** (1995), 1.
- [42] M. Orozco, C. Alhambra, X. Barril, J. M. López, M. A. Busquets, and F. J. Luque, *Journal of Molecular Modeling* **2** (1996), 1.
- [43] Frenkel, D. and Smit, B., *Understanding Molecular Simulation*, Academic Press: San Diego, (2002).
- [44] R. W. Zwanzig, *Journal of Chemical Physics* **22** (1954), 1420.
- [45] T. Yamamoto, *Journal of Chemical Physics* **33** (1960), 281.
- [46] D. Chandler, *Journal of Chemical Physics* **68** (1978), 2959.
- [47] Chandler, D., *An Introduction to Modern Statistical Mechanics*, Oxford University Press: New York, (1987).
- [48] Bennett, C. H., *Diffusion in Solids: Recent Developments*, Academic Press, New York, 1975.
- [49] P. G. Bolhuis, C. Dellago, and D. Chandler, *Faraday Discussions* **110** (1998), 421.
- [50] W. H. Miller, S. D. Schwartz, and J. W. Tromp, *Journal of Chemical Physics* **79** (1983), 4889.
- [51] J. W. Tromp and W. H. Miller, *Journal of Physical Chemistry* **90** (1986), 3482.
- [52] H. A. Kramers, *Physica* **7** (1940), 284.
- [53] S. Chandrasekhar, *Reviews of Modern Physics* **15** (1943), 1.
- [54] R. F. Grote and J. T. Hynes, *Journal of Chemical Physics* **73** (1980), 2715.
- [55] M. J. Ruiz-Montero, D. Frenkel, and J. J. Brey, *Molecular Physics* **90** (1997), 925.
- [56] E. Wigner, *Journal of Chemical Physics* **5** (1937), 720.
- [57] Horiuti, *Journal of the Bulletin of the Chemical Society of Japan* **13** (1938), 210.
- [58] J. C. Keck, *Advances in Chemical Physics* **13** (1967), 85.
- [59] D. G. Truhlar and B. C. Garrett, *Annual Reviews in Physical Chemistry* **35** (1984), 159.

- [60] Foresman, J. B. and Frisch, Æ., *Exploring Chemistry with Electronic Structure Methods*, Gaussian, Inc.: Pittsburgh, (1996).
- [61] D. G. Truhlar, B. C. Garrett, and S. J. Klippenstein, *Journal of Physical Chemistry* **100** (1996), 12771.
- [62] D. G. Truhlar, Y.-P. Liu, G. K. Schenter, and B. C. Garrett, *Journal of Physical Chemistry* **98** (1994), 8396.
- [63] B. C. Garrett and G. K. Schenter, *International Reviews in Physical Chemistry* **13** (1994), 263.
- [64] G. A. Voth, D. Chandler, and W. H. Miller, *Journal of Chemical Physics* **91** (1989), 7749.
- [65] G. A. Voth, *Journal of Physical Chemistry* **97** (1993), 8365.
- [66] Voth, G. A., *New Trends in Kramers' Reaction Rate Theory*, Kluwer: Dordrecht, (1995).
- [67] P. G. Wolynes, *Physical Review Letters* **47** (1981), 968.
- [68] R. Car and M. Parrinello, *Physical Review Letters* **55** (1985), 2471.
- [69] Trout, B. L., *Advances in Chemical Engineering* **28**, edited by Chakraborty, A., Academic Press: San Diego (2001), 353.
- [70] A. Jamnik, *Journal of Chemical Physics* **102** (1995), 5811.
- [71] A. Huerta, S. Sokolowski, and O. Pizio, *Molecular Physics* **97** (1999), 919.
- [72] Y. Duda, D. Henderson, B. Millan-Malo, and O. Pizio, *Journal of Physical Chemistry B* **101** (1997), 10687.
- [73] O. Pizio, D. Henderson, and S. Sokolowski, *Journal of Physical Chemistry* **99** (1995), 2408.
- [74] C. Segura, E. Vakarín, W. Chapman, and M. Holovko, *Journal of Chemical Physics* **108** (1998), 4837.
- [75] A. Trokhymchuk, O. Pizio, and S. Sokolowski, *Journal of Colloid and Interface Science* **178** (1996), 436.
- [76] A. Kovalenko, O. Pizio, and D. Henderson, *Journal of Physical Chemistry B* **101** (1997), 3571.

[77] B. M. Malo, L. Salazar, S. Sokolowski, and O. Pizio, *Journal of Physics: Condensed Matter* **12** (2000), 8785.

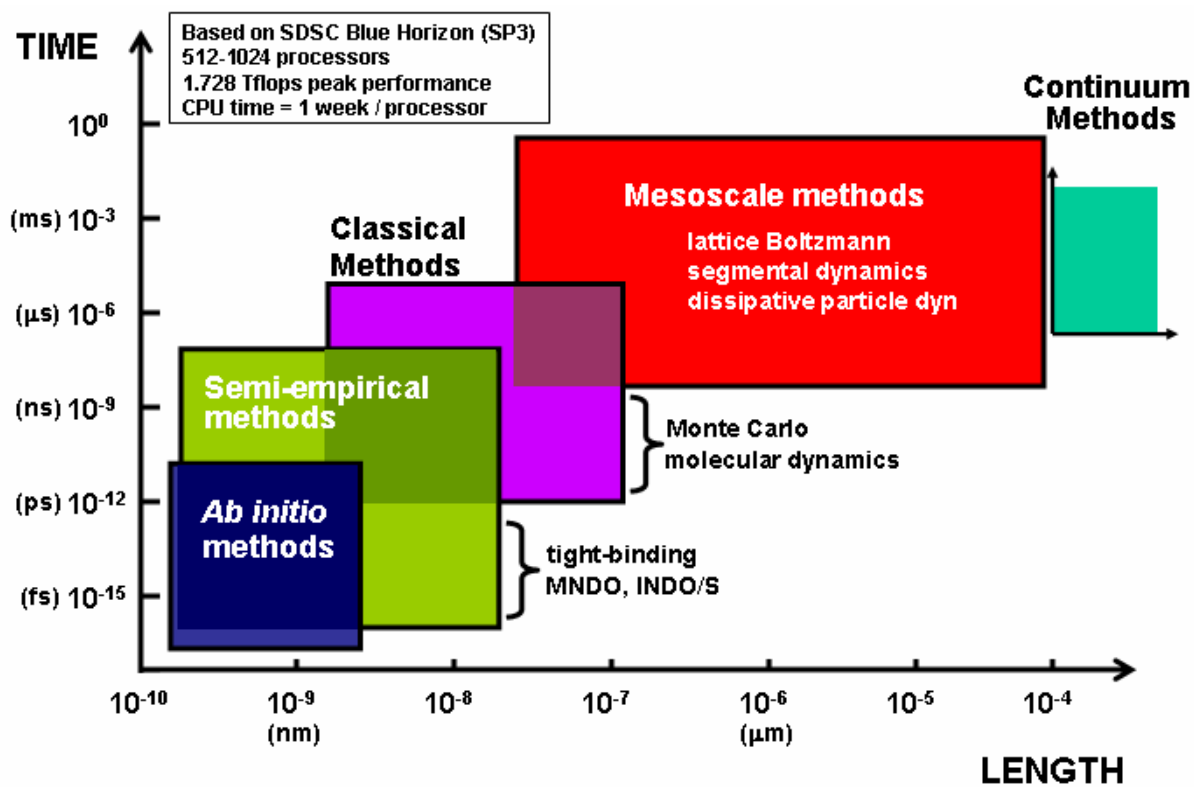


Figure 1.1 Molecular simulation time scales for various computational methods. This assumes calculations are allowed for a maximum of one week on the Blue Horizon (SP3) supercomputer, which operates at a maximum speed of 1.728 Tflops.

CHAPTER 2

Dimerization of Nitric Oxide

2.1 Introduction

We began our project by looking at the dimerization of nitric oxide, Eq. (2.1), within microporous carbons [1]:



The NO dimerization reaction is a convenient choice for several reasons. First, the molecules involved are simple and easy to model in simulations. NO has a negligible dipole moment and a small quadrupole moment [2]. Intermolecular force models for both NO and (NO)₂ have already been developed based on site-site Lennard-Jones potentials and have been shown to give an accurate account of the chemical equilibrium in the bulk gas and liquid phases [3]. Second, NO dimerization is interesting because experimental measurements have been reported for this reaction in both the bulk phase [4-6] and in activated carbons having slit pores [7]. The NO molecule is paramagnetic while the (NO)₂ dimer is diamagnetic. Therefore the composition of the reaction mixture in the activated carbon can be obtained by measuring the magnetic susceptibility [7]. Furthermore, this reaction is important in atmospheric chemistry [8], pollution abatement [8], and in medicine, where it controls certain

functions in living organisms [9]. It is important to note that activated carbons are commonly used for removal of nitrogen oxides from auto exhaust and industrial effluent gas streams.

Although there is only limited experimental data for reactions in confinement, there have been several attempts by Kaneko and co-workers at Chiba University to measure chemical reaction equilibria in pores [7,10], which includes studies of the NO dimerization reaction. However, there are typically many challenges associated with these types of experiments. First of all, determining the composition of the confined phase is usually very difficult and is only possible using indirect methods. It is usually impossible to distinguish between true equilibrium in the pore and long-lived metastable states. Also, it has not proved possible to determine the free energies of confined phases. In spite of these challenges, Kaneko *et al.* [7] have been able to observe large increases in yield for the nitric oxide dimerization reaction within activated carbons.

The increased conversion in the pore phase can be understood in terms of Le Chatlier's principle, since there is a reduction in the number of moles as the conversion shifts towards the (NO)₂ dimer. According to Le Chatlier's principle, the increased density within the pore phase should naturally shift the conversion towards the formation of (NO)₂, as well as any other reaction that involves a reduction in mole number. Surprisingly however, this same group found large increases in yield for the following two reactions when carried out in activated carbons:



We would not expect the increased density in the pores to produce these results, so a more subtle explanation must exist.

In order to clarify the experimental picture, we have modeled the nitric oxide dimerization reaction, Eq. (2.1), within two different microporous models, intended to represent activated carbon fibers and carbon nanotubes. The model for the activated carbons (the slit-pore model) was assigned pore widths similar to the carbons used by Kaneko et al. [7], in the range of 0.8 to 0.9 nm.

Using molecular simulations, we should be able to clarify the experimental understanding of this system by answering several basic questions:

- a) Do simulations and experiments predict the same conversion in microporous carbons?
- b) How sensitive is the conversion of the reaction to the width of the pore?
- c) What is the distribution and orientation of the molecules within the pore?
- d) What is the primary driving force for the equilibrium in the pore phase?

The rest of this Chapter is arranged as follows. In Section 2.2 we will describe the simulation techniques that we have used to predict the reaction conversion. Next, we will

present in Section 2.3 the models that we have used for the reacting molecules and the carbon pore. Then in Section 2.4 we will discuss our results and compare with the experimental and theoretical results of other groups. Finally, in Section 2.5 we will present our conclusions and extensions of this work.

2.2 Simulation Methods

2.2.1 Reactive Monte Carlo

As mentioned in Chapter 1, we have used the Reactive Monte Carlo (RxMC) method [3] to determine the equilibrium state of reactive mixtures in both the bulk phase and also in micropore spaces. Attractive features of this method are that it can be applied to reactions in which the number of mole changes and to reactions in multiple phases, and it is not necessary to calculate chemical potentials or chemical potential differences. The RxMC approach is designed to minimize the Gibbs energy at constant pressure, thus determining the true equilibrium condition, irrespective of any rate limitations. The general acceptance criteria for the forward and reverse reaction steps used in this method can be found by combining the grand canonical partition function for a multi-component fluid with the restrictions of chemical equilibrium, $\sum \mathbf{n}_i \mathbf{m}_i = 0$, and conservation of mass. The resulting expression for the acceptance criteria can be easily evaluated in simulation for either a forward or reverse reaction step:

$$P_{acc} = \min \left[1, \exp(-\beta dU) \prod_{i=1}^c q_i^{n_i} \prod_{i=1}^c \frac{N_i!}{(N_i + \mathbf{n}_i)!} \right] \quad (2.4)$$

In the above equation, \mathbf{b} is the reciprocal of the Boltzmann constant times the temperature, q_i is the partition function for molecular species i , N_i is the number of moles of species i , \mathbf{n}_i is the stoichiometric coefficient for component i (negative for reactants and positive for products), and dU is the change in configurational energy during the attempted reaction step. The products in Eq. (2.4) are over the total number of species C participating in the reaction. For a rigorous derivation and confirmation that detailed balance is obeyed during the RxMC moves, see the recent review by Johnson [11]. The constant pressure version of the RxMC method, as applied to nitric oxide dimerization, involves the following trial moves [3], with each move being accepted with the designated probability criterion (P_{acc}):

(a) A change in the position or orientation of a molecule, chosen at random

$$P_{acc} = \min [1, \exp(-\mathbf{b}dU)] \quad (2.5)$$

(b) $2\text{NO} \rightarrow (\text{NO})_2$: A forward reaction step, in which one randomly selected NO molecule is deleted and another randomly selected NO molecule is changed to $(\text{NO})_2$, with the acceptance probability of:

$$P_{acc} = \min \left[1, \exp(-\mathbf{b}dU_F) \times \frac{q_{(\text{NO})_2}}{q_{\text{NO}}^2} \times \frac{(N_{\text{NO}})(N_{\text{NO}} - 1)}{(N_{(\text{NO})_2} + 1)} \right] \quad (2.6)$$

(c) $(\text{NO})_2 \rightarrow 2\text{NO}$: A reverse reaction step, in which one randomly selected $(\text{NO})_2$ molecule is changed to NO and another NO molecule is randomly inserted into the system, with the acceptance probability of:

$$P_{acc} = \min \left[1, \exp \left(- \mathbf{b} dU_R \right) \times \frac{q_{NO}^2}{q_{(NO)_2}} \times \frac{N_{(NO)_2}}{(N_{NO} + 1)(N_{NO} + 2)} \right] \quad (2.7)$$

(d) $V_{B,o} \rightarrow V_{B,n}$: A random change of volume, in order to maintain the bulk pressure constant:

$$P_{acc} = \min \left[1, \exp \left\{ - \mathbf{b} \left[dU_V + P dV_B - N \mathbf{b}^{-1} \ln \left(V_{B,n} / V_{B,o} \right) \right] \right\} \right] \quad (2.8)$$

In the above equations, the symbols dU_F , dU_R , and dU_V represent the changes in the configurational energy of the system for forward reaction, reverse reaction, and volume change steps, respectively. In the volume change steps, $V_{B,o}$ is the original volume, $V_{B,n}$ is the new system volume, and dV_B is the difference between these two volumes, $V_{B,n} - V_{B,o}$. In order to maintain microscopic reversibility, the forward and reverse reaction steps (steps b and c above) must be attempted with equal probability, and in an identical fashion. To illustrate this last point more clearly, consider the more general equilibrium reaction: $A+B \leftrightarrow C+D$. If A is replaced by C and B is replaced by D in a forward reaction step, then the reverse move must preserve detailed balance by replacing C with A and D with B.

While performing the single-phase bulk simulations, we used the isothermal-isobaric ensemble, which specifies the total number of atoms, the pressure, and the temperature of the system. For the nitric oxide bulk phase simulations, we typically used 1,200 NO particles, equilibrated for about 10×10^6 moves, and took averages for about 30×10^6 moves. The simulation lengths at the lower temperatures were approximately five times longer, due to slower convergence. The potential cutoff was set at 1.6 nm ($5.0 s_{NO}$), with no long-range corrections applied.

2.2.2 Constant Pressure Gibbs Ensemble Monte Carlo

In order to simulate a two-phase system, consisting of a pore phase and a bulk phase, we implemented a constant pressure Gibbs ensemble Monte Carlo technique [12,13]. This technique divides our system into two separate phases (or simulation boxes): (1) the bulk gas phase and (2) the microporous carbon phase. Through the appropriate application of the RxMC simulation moves and the constant pressure Gibbs ensemble, we maintain chemical equilibrium within each phase and phase equilibrium between the bulk and the pore phase:

$$\sum n_i \mathbf{m}_{i,bulk} = \sum n_i \mathbf{m}_{i,pore} = 0 \quad (2.9)$$

$$\mathbf{m}_{i,bulk} = \mathbf{m}_{i,pore} \quad (2.10)$$

This simulation design facilitates a more natural comparison with experimental results, since the specified simulation parameters are temperature, pressure, and initial composition, and the measured quantity is the equilibrium conversion (along with other thermodynamic properties). This technique permits the use of a constant pressure bulk phase, eliminating the need to specify chemical potentials or fugacities. The equilibria between the two phases is maintained through attempted particle exchange, which only requires the (# of reacting species - 1) to be exchanged, since the chemical equilibrium of the last species will always be maintained through the RxMC steps in each of the discrete phases. The particle exchanging convention is chosen to increase the sampling efficiency, as only the smaller molecules are used for insertions and deletions (in our case the NO monomer). The validity of this method

was tested by swapping all molecular species (monomer and dimer) between the two phases, and we obtained identical reaction conversions. Additionally, the chemical potential of each species was measured in simulation using Widom's test particle insertion method [14], in order to insure that Eq. (2.9) and (2.10) are satisfied.

According to the constant pressure Gibbs ensemble method [12,13], the following moves are added to establish equilibrium between the bulk phase reaction and the pore phase reaction:

(a) particle transfer from the bulk phase to the pore phase ($N_{B,i} - 1, N_{P,i} + 1$):

$$P_{acc} = \min \left[1, \exp \left(- \mathbf{b}dU_{N_{B,i}-1} - \mathbf{b}dU_{N_{P,i}+1} \right) \times \frac{N_{B,i} V_P}{(N_{P,i} + 1) V_B} \right] \quad (2.11)$$

(b) particle transfer from the pore phase to the bulk phase ($N_{B,i} + 1, N_{P,i} - 1$):

$$P_{acc} = \min \left[1, \exp \left(- \mathbf{b}dU_{N_{P,i}-1} - \mathbf{b}dU_{N_{B,i}+1} \right) \times \frac{N_{P,i} V_B}{(N_{B,i} + 1) V_P} \right] \quad (2.12)$$

In equations (2.11) and (2.12), $N_{P,i}$ and $N_{B,i}$ represent the number of molecules of type i in the pore and bulk phase, respectively. V_B is the volume of the bulk phase and V_P is the volume of the pore phase. The exponential term in equations (2.11) and (2.12) accounts for the total change in potential energy associated with the particle transfer.

2.3 Simulation Models

2.3.1 Molecular Models

The intermolecular potential models used for the NO dimerization reaction were those previously applied by Johnson *et al.* [3]. Following Kohler *et al.* [15], the NO and (NO)₂ interactions were modeled using the site-site Lennard-Jones (LJ) potential:

$$u_{ij} = \sum_a \sum_b 4e_{ia,jb} \left[\left(\frac{\mathbf{s}_{ia,jb}}{r_{ia,jb}} \right)^{12} - \left(\frac{\mathbf{s}_{ia,jb}}{r_{ia,jb}} \right)^6 \right] \quad (2.13)$$

In equation (2.13), the sum is calculated over the sites (**a**) on molecule *i* with each site (**b**) on molecule *j*, $r_{ia,jb}$ is the separation distance between sites on different molecules, and the interaction parameters **s** and **e** are specific to each molecular species, as shown in Table 2.1. Since the dipole moment ($\mathbf{m}=0.16 \times 10^{-18}$ esu) of NO is very small, and the quadrupole moment ($Q \sim -1.0 \times 10^{-26}$ esu) is also rather small [2], electrostatic forces were neglected. The (NO)₂ dimer was modeled using a two-site LJ potential. The individual site parameters of the dimer were identical to those of the monomer, and the bond length was set equal to the experimental value of 0.2237 nm [16]. In Table 2.1, the positions of the two LJ sites of the dimer are given in reference to the center of mass, so that each site is displaced from the center of mass by a distance of "*bl*".

Fluid-wall interactions were calculated between the LJ sites on the fluid and the LJ carbon atoms forming the walls of the slit-shaped pores or the carbon nanotubes, depending on the

chosen pore model. Unlike pair interactions between the fluid molecules and the carbon pores were approximated using the standard Lorentz-Berthelot mixing rules: $\epsilon_{ia,jb} = (\epsilon_{ia}\epsilon_{jb})^{1/2}$ and $s_{ia,jb} = (s_{ia}+s_{jb})/2.0$.

Table 2.1 Summary of the Lennard-Jones parameters.

molecule	site #	b/nm	s/nm	$\epsilon/k_b/\text{K}$	reference
NO	1	0.0	0.31715	125.0	[15]
(NO) ₂	1	0.11185	0.31715	125.0	[3]
	2	0.11185	0.31715	125.0	
C (pore)	1	0.0	0.340	28.0	[17]

We calculated the molecular partition functions for NO and (NO)₂ from a variety of sources; these are used in the acceptance criteria for the forward and reverse reaction steps.

Molecular constants for the NO monomer were taken from standard sources [18,19].

Rotational and vibrational constants for the dimer were taken from Kukolich [16] and Smith *et al.* [20], respectively. Unfortunately, the experimental and theoretical values of the dimerization energy, D° , vary over a wide range: from 7.64 to 13.8 kJ/mol [21-25].

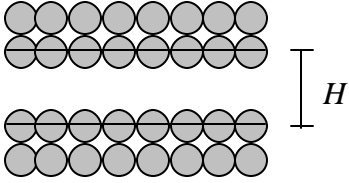
Therefore, we fitted our simulation data at the lowest temperature of 110 K to experimental data for the dimer mole fraction in the bulk saturated liquid and obtained a value of $D^\circ=10.9$ kJ/mol, which is close to the midpoint of the range of experimental estimates.

2.3.2 Pore Models

Carbon slit-shaped pores were used as an approximate model for the activated carbon fibers used by Kaneko *et al.* [7]. The 10-4-3 Steele potential [17], was used to model the interaction of the reacting adsorbate molecules with the carbon walls, with the usual potential

parameters for carbon (Table 2.1). This model assumes that the carbon pore is constructed of two parallel walls that are infinite in the x-y plane. The structure of these walls is assumed to be that of sheets of graphite, and the surface corrugation is neglected by averaging the carbon potential over the two graphitic pore surfaces. As a result, the interaction potential between an adsorbate molecule and the pore wall is only a function of the z-coordinate, the distance of each site from each pore wall.

$$U_{ia,c}(z) = 4pe_{ia,c}s_{ia,c}^2\Delta r_c \left[\frac{1}{5} \left(\frac{s_{ia,c}}{H/2 \pm z} \right)^{10} - \frac{1}{2} \left(\frac{s_{ia,c}}{H/2 \pm z} \right)^4 - \frac{s_{ia,c}^4}{6\Delta(H/2 \pm z + 0.61\Delta)^3} \right] \quad (2.14)$$



In equation (2.5), H is the width of the pore, defined as the distance between carbon centers on the two opposing walls of the pore, Δ is the experimentally measured interlayer spacing of graphite (0.335 nm), r_c is the experimentally measured density of graphite (2.27 g/cm³), and e and s are the LJ parameters shown in Table 2.1.

The models for the carbon nanotubes were slightly more detailed. We modeled the carbon nanotubes by using explicit carbon atoms, with site-site LJ interactions (no electrostatic interactions) between the carbon atoms and the adsorbate molecules. The nanotubes were chosen to be single-walled carbon nanotubes, arranged in a hexagonal array, as is the

configuration typically observed in experiments. Nanotubes can be uniquely defined in terms of their helicity, and according to the standard convention [26], the nanotubes in our model are designated as (10,10) nanotubes. This is essentially an armchair type of structure, with ten carbon rings forming the circumference of the cylinder. The corresponding diameter of these nanotubes is 1.36 nm, as measured from the carbon centers. Figure 2.1 shows the (10,10) nanotubes in a bundled configuration, as used in our simulations. The distance between neighboring nanotubes within a bundle is 0.34 nm (as measured from the carbon centers), which is the LJ diameter of carbon. Periodic boundary conditions are applied in all three coordinate directions, and adsorption and reaction are allowed within the nanotubes and in the interstitial spaces between the tubes.

As a refinement to the ideal nanotube model, depicted in Figure 2.1, we have added defects to the nanotube structure. This modification should create more realistic representations of the actual nanotube samples used in experiments. Experimental synthesis of single-walled carbon nanotubes typically results in the production closed-end structures, which decrease adsorption capacity and diffusion [27-31]. In order to open the ends of these tubes, chemical cutting can be applied, followed by thermal decomposition of functional groups. This chemical cutting and thermal treatment process creates a more porous material by removing approximately 5% of the carbon structure. Some of the removed carbon originates from the tips of the nanotubes, but a large fraction of the carbon comes from the nanotube walls. The defects are reflected in our models by randomly removing similar amounts of carbon from the nanotube arrays. We have randomly removed 2.5%, 5.0%, 7.5%, and 10% of the carbon

from the structure in order to quantify the influence of the defects on the yield of confined chemical reactions. The only restriction imposed during this process is that every carbon atom within a single nanotube must maintain connectivity with the neighboring atoms, so that an unphysical structure is not produced. In other words, we have intentionally eliminated the possibility of "floating" carbon atoms within our nanotube model. A simulation snapshot of one of these defective bundles, in the absence of the nitric oxide reaction, is shown in Figure 2.2. It is additionally noted that defects can be intentionally introduced into the nanotube structure by ion irradiation [32].

2.4 Results and Discussion

2.4.1 Reaction in the Bulk Phase

In order to validate the molecular models, we first carried out RxMC simulations for the NO reaction in the bulk phase using an isothermal-isobaric (NPT) ensemble. We began by making comparisons in the bulk saturated liquid phase for the nitric oxide reaction. Reliable experimental data is available for this reaction for temperatures in the range of 110-120 K [4], and extrapolated estimates for the reaction yield is available from 120-170K [6]. The fraction of dimers was much higher in the liquid phase than in the gas phase in both experiment and in our simulations. In Figure 2.3, our simulated results in the liquid phase show excellent agreement in the temperature range over which the experimental and extrapolated experimental results are available. For the vapor phase at a pressure of 1.01 bar and 121.4 K we obtained a mole percent of monomers of 98%, which is in agreement with

Guggenheim's estimate [5] based on analysis of second virial coefficient data. In both gas and liquid phases, our simulations are consistent with the reference data.

The heat of reaction, ΔH_r , was measured using a van't Hoff plot, and we obtained a value of 12.8 kJ/mol. This is well within the range of experimental measurements of 11.0 to 15.5 kJ/mol [4,5]. The heat of reaction was obtained from the slope of the natural logarithm of the equilibrium constant, K_c , versus the inverse temperature of the reaction, where K_c is written in terms of the concentrations. This assumes an ideal gas phase. The equilibrium constant can also be calculated directly from the partition functions of each of the reacting molecules, as shown in Eq. (2.15), and is a function of temperature only.

$$K_c = \frac{(q_{(NO)_2}/V)^{n_{(NO)_2}}}{(q_{NO}/V)^{n_{NO}}} = \frac{[(NO)_2]}{[NO]^2} \quad (2.15)$$

2.4.2 NO Dimerization in slit-shaped carbon pores

After confirming the accuracy of our simulated conversion in the bulk gas and liquid phases, we then wanted to measure the effects of confinement by allowing the reaction to adsorb into the slit-shaped carbon pores. We investigated the influence of confinement on conversion by combining the two-phase simulation technique with RxMC moves (as described in Section 2.2.2). This permitted the use of a constant pressure bulk phase and made it possible to simultaneously predict both chemical and phase equilibrium in the pore.

The confinement in the slit-pores had a large effect on the yield of dimers for the nitric oxide reaction. Results for the yield of dimers for a range of pore sizes and temperatures are shown in Figure 2.4, for a constant bulk pressure of 0.16 bar (which corresponds to a gas phase). Results for the reaction in the bulk gas phase at these same conditions are shown for comparison. The initial mixtures at the start of the simulations contained 100% NO monomers. However, different starting compositions were tested and found not to influence the final conversion, as should be expected. The simulations show a great enhancement of the dimer formation in the pores, with increases of a factor of about 40 at the lower temperatures. This enhancement effect becomes greater as the pore size is reduced. For larger pore sizes, above $4.00s_{NO}$, the influence of further increases in pore width is small. The reason for this is readily seen from plots of the solid-fluid interaction potentials, shown in Figure 2.5. For the larger pores, the adsorbate molecules near the center of the pore experience only a weak interaction with the walls. Consequently, the fluid density in the center of the pore is small in these larger pores (Figure 2.6) and contributes little to the average dimer yield in the pore. The density profiles in the smaller pores are more dependent on pore size deviations due to potential overlap near the center of the pore. The density is high even near the pore center (Figure 2.7), and thus the yield is more strongly affected by variation in pore width. It is expected that the pore phase conversion would approach the bulk phase conversion as the width of the pore increases.

The yield of $(NO)_2$ dimers in the pore is strongly affected by the temperature, and this temperature effect is much larger than that seen in the bulk phase. This increased

temperature sensitivity arises because of the strong temperature dependence of the average density in the pore. As the temperature is increased, the molecules tend to migrate from the pore phase to the bulk phase, reducing the average density in the pore and shifting the equilibrium further towards the NO monomers.

The effect of varying the bulk gas pressure on the number of molecules adsorbed is shown in Figure 2.8 for a temperature of 122.5 K and a slit width of $5.5s_{\text{NO}}$ (1.74 nm). A relatively low temperature was chosen in order to observe the effect of capillary condensation in the pore. Capillary condensation leads to the filling of the pore with a phase of liquid-like density, and is a first order transition. It results in the formation of additional dense layers of molecules in the center of the pore. Although the number of dimers in the pore almost doubles upon capillary condensation, the overall mole fraction in the pore is only slightly enhanced since the monomers fill the pore in a similar proportion. Therefore, although there is a significant amount of hysteresis in the adsorbate density, there is only a small amount of hysteresis in the pore phase conversion. The small cusp in Figure 2.8 at around 0.52 bar is due to finite-scaling effects, as this point corresponds to a change of the simulation box size.

Since first publishing our simulated conversion for the NO dimerization reaction in the slit-shaped carbon pores [1], our results have been verified by Tripathi and Chapman [33] at Rice University using perturbation density-functional theory (TPT1)[34]. They have used similar intermolecular potentials and models for the NO monomer, the $(\text{NO})_2$ dimer, and the slit-shaped carbon pore. The DFT predictions, illustrated in Figure 2.9, show excellent

agreement with our simulation results (Figure 2.4) but tend to predict slightly higher conversion than the RxMC simulations at the higher temperatures. As noted by Tripathi and Chapman [34], these small discrepancies between simulation and theory could possibly originate from two different sources. First, the long-range fluid-fluid interactions are slightly different, as the DFT calculations use a hard-sphere reference and the attractive tail treated in the mean field approximation. This specifically neglects fluctuations in the density and energy, and molecular correlations are neglected, in contrast to the simulations. Secondly, the theory is based on Wertheim's first order perturbation theory (TPT1) [35-38], which assumes the dimers are formed from tangent spheres. Wertheim's theory has been shown [39] to deviate from exact results when applied to systems with bond lengths less than $0.8s$. The bond length of the $(\text{NO})_2$ dimer model is $0.705s_{\text{NO}}$, which may cause slight errors.

The increased yield shown by our nitric oxide simulations [1] and theory [34] is qualitatively similar to that found in experiments [7], which were carried out at ambient temperature and above. However, the experiments show even larger increases in dimerization than we find in our simulations. Thus, at 298 K and a bulk pressure of 0.8 bar (the pressure studied experimentally) we find a dimer mole fraction of 0.22 for a pore width H of 0.85 nm. Keeping the pressure and pore width constant and raising the temperature to 373 K, reduces the simulated mole fraction of dimers to 0.033. Similar mole fractions are found using DFT at these two temperatures: 0.17 at 298 K and 0.023 at 373 K [34]. The experiments surprisingly indicate a constant yield of approximately 0.98 mole fraction dimers at these elevated temperatures. The reason for this discrepancy is unresolved. However, the

qualitative correspondence between simulation and theory, suggests a reconsideration of the experimental results.

This system is now being investigated by Prof. J. Yates at the University of Pittsburgh. Studying the same reaction, the dimerization of nitric oxide, Yates is using spectroscopic techniques to look at the formation of the $(\text{NO})_2$ dimer in (10,10) carbon nanotubes. In anticipation of this comparison, we have performed additional simulations of this system in (10,10) carbon nanotubes, which are modeled with site-site interaction parameters. We expect that comparison with the Yates' experiments will shed light onto the discrepancy found for (slit-shaped) activated carbons.

2.4.3 NO Dimerization in Carbon Nanotubes

Our simulations show that the equilibrium shift in the NO conversion is even more dramatic in the carbon nanotubes. Since we have already verified the conversion in the bulk phase reaction, we will use these same models of NO and $(\text{NO})_2$ for simulating the conversion in the carbon nanotubes. These are again two-phase simulations that insure both chemical and phase equilibrium between the reaction in the bulk phase and the reaction in the nanotubes.

We began by simulating the conversion in a perfect (10,10) carbon nanotube bundle (Figure 2.1). Each nanotube in the bundle has a diameter of 1.36 nm, as measured from the carbon centers. Both adsorption and reaction were allowed within the nanotubes and in the interstitial spaces between adjacent carbon nanotubes. The simulations were performed at a

constant temperature of 130 K while the pressure was varied from 0.001 bar to 0.100 bar and the resulting conversion was measured. The mole fraction of the (NO)₂ dimer is shown in Figure 2.10 at various pressures for two different nanotube-nanotube separation distances, 0.34 nm and 0.32 nm.

Table 2.2 Simulation results of the nitric oxide dimerization reaction in the bulk gas phase at a temperature of 130 K.

Pressure/bar	$y_{(\text{NO})_2}$	density/(mol/L)
0.001	0.000011	0.000092
0.005	0.000052	0.000463
0.010	0.000105	0.000924
0.025	0.000262	0.002314
0.050	0.000523	0.004628
0.100	0.001041	0.009232

In the pressure range that we have studied (0.001 to 0.100 bar), there is a significant increase in the reaction conversion as compared to the conversion in the bulk gas phase, which is shown in Table 2.2 as $y_{(\text{NO})_2}$. This can be attributed mainly to the increased density found within the nanotubes, as compared to the equilibrium bulk phase. Snapshots from our simulations clearly demonstrate this point, as significant changes in the conversion correspond to increases in the fluid adsorption. Figure 2.11 contains four snapshots, each corresponding to a different pressure, and hence a different conversion. There is a large increase in conversion from a pressure of 0.001 bar to 0.005 bar, and this is reflected in the filling of the nanotubes. As the pressure is further increased, the adsorption increases gradually, along with the conversion, and a second layer begins to form in the center of the pore. When the conversion in the (10,10) nanotubes is compared with that in a slit-shaped pore of similar dimensions ($H=1.36$ nm), we find the mole fraction of (NO)₂ to be

consistently higher in the nanotubes. For example, at a bulk pressure of 0.16 bar and a temperature of 130 K, the mole fraction of $(\text{NO})_2$ in the bundle of (10,10) nanotubes is 0.875, while the mole fraction in the slit-pore is 0.705.

Figure 2.10 also shows that the conversion in the more tightly packed model is about 5% higher than the model with the 0.34 nm nanotube-nanotube separation, and this differential increases to about 8% at the highest pressure studied. Snapshots from our simulations clearly explain the shift in conversion between the two different nanotube models. Figure 2.12 reveals that at a 0.34 nm separation distance NO and $(\text{NO})_2$ can adsorb within the interstitial spaces of the nanotubes. Due to the restricted size of these cavities, NO (the smaller species) is preferentially formed over $(\text{NO})_2$, in contrast to the reaction within the nanotubes. The formation of NO in the interstitial spaces dilutes the overall conversion of the system. However, the more tightly packed structure (0.32 nm spacing) completely eliminates adsorption or reaction between the nanotubes, and hence reduces the formation for the nitric oxide monomer. This preserves the elevated conversion of the overall nanotube structure, since NO formation is geometrically forbidden within the interstitial gaps.

Structural defects in the nanotube can yield surprising results in the equilibrium conversion, as shown in Figure 2.13. The most significant effects are seen at intermediate pressures from about 0.005 bar to 0.010 bar. For example, only 5% defects in the nanotube structure causes the mole fraction of $(\text{NO})_2$ to fall from 0.611 to 0.309 at a pressure of 0.005 bar. The driving force for the shifts in conversion can be attributed to the adsorbate density. As the defects

increase, the nanotubes become less adsorptive, and the conversion tends to diminish. Figure 2.14 illustrates this more clearly, as the adsorbate density is plotted versus the pressure for the same array of defective nanotubes. The adsorbate density plotted in Figure 2.14 is almost an exact reproduction of the mole fraction plotted in Figure 2.13, which suggests again that the conversion within the nanotubes is strongly linked to the adsorbate density.

2.5 Conclusions

For the nitric oxide dimerization reaction, there are large increases in dimerization, within carbon slit-pores and carbon nanotubes, especially at lower temperatures and higher pressures. In these systems the carbon pores show no significant preference for the two reactant NO molecules over one product (NO)₂ molecule, since the LJ parameters are identical for the two molecules, and hence adsorption selectivity is not an important factor. For this reaction the large increase in dimerization is mainly due to the increased density within the pores. This conclusion is confirmed by calculations of the mole fraction of dimers in a bulk phase reacting mixture at a density equal to the average density found in the pore. The yield of dimers in such a system is very similar to that found in the carbon pore, indicating that the principal effect of confinement is the increased density of the reaction mixture.

For NO dimerization, the yield in the slit-pores decreases rapidly as temperature is increased, particularly for the narrower pores. This temperature effect is much larger than that for the bulk phase, and arises because the average density in the pore decreases rapidly with rise in

temperature. In both phases, the exothermic nature of the reaction contributes to the temperature sensitivity of the equilibrium conversion.

The NO dimerization in the (10,10) carbon nanotubes yields similar increases in conversion. The fundamental difference between the two systems is that the slit-pores confine the system in only one of the dimensions (z), while the nanotubes confine the reaction in two dimensions. We found that by manipulating the nanotube-nanotube separation distance we can inhibit NO monomer formation in the interstitial spaces, and thus increase the overall $(\text{NO})_2$ yield for the system. Alternatively, we found that the conversion decreases when defect sites (*i.e.*, structural vacancies) are included in the nanotube model, due to the decreased adsorption strength of the pores. The effects tend to fade away at pressures of 0.100 bar and greater.

While our simulations [1] and the theoretical work of Tripathi and Chapman [34] are in almost exact agreement for the NO dimerization reaction in carbon slit-pores, the experimental investigation gives quantitatively different results [7]. The reason for this discrepancy is still unclear. While both simulation and experiment show a large increase in dimerization due to confinement, the effect is much larger in the reported experiments. The composition in the pore is determined experimentally from magnetic susceptibility measurements. Since NO is paramagnetic and $(\text{NO})_2$ is diamagnetic, by assuming that changes in magnetic susceptibility arise solely from the dimerization reaction it is possible to deduce the composition of the equilibrium mixture. It is possible that other phenomena

contribute to the magnetic susceptibility. One such possibility is complexation between the NO monomer and defects on the pore surface. Alternatively, other molecular species could be formed within the pore which might be incorrectly interpreted as (NO)₂ dimers.

We note that the intermolecular potential models used in our simulations are simple, and that additional interactions, particularly between the fluid molecules and the wall, could be significant. For example, electrostatic and induction interactions with the carbon wall have been neglected. However, from test simulations we find that the binding energy of the dimer would have to increase by a factor of six in order to approach the elevated conversions measured in the experiments. Our *ab initio* calculations of the (NO)₂ dimer near a carbon surface have shown that an increase in the binding energy of this magnitude is unlikely. Our calculations have shown that the binding energy of the dimer is actually 2.3 kcal/mol *lower* near a carbon surface than in the gas phase. These calculations were performed with *Gaussian 98* [40] using the density function theory (DFT) method in conjunction with the B3LYP functional, while the carbon surface was approximated as a benzene ring.

We believe in this work we have fully investigated the equilibrium conversion of the nitric oxide dimerization reaction and have shown adequate justification for reconsideration of the experimental results. John Yates at the University of Pittsburgh is currently using spectroscopic techniques to study NO dimerization in (10,10) carbon nanotubes, which should provide a rigorous test of the earlier measurements [7].

References

- [1] C. H. Turner, J. K. Johnson, and K. E. Gubbins, *Journal of Chemical Physics* **114** (2001), 1851.
- [2] Gray, C. G. and Gubbins, K. E., *Theory of Molecular Fluids*, App. D, Clarendon: Oxford, (1984).
- [3] J. K. Johnson, A. Z. Panagiotopoulos, and K. E. Gubbins, *Molecular Physics* **81** (1994), 717.
- [4] A. L. Smith and H. L. Johnston, *Journal of the American Chemical Society* **74** (1952), 4696.
- [5] E. A. Guggenheim, *Molecular Physics* **10** (1966), 401.
- [6] Guedes, H. J. R., *Thermodynamic properties of simple liquid systems*. PhD Thesis, Universidade Nova de Lisboa, Portugal, (1988).
- [7] K. Kaneko, N. Fukuzaki, K. Kakei, T. Suzuki, and S. Ozeki, *Langmuir* **5** (1989), 960.
- [8] Seinfeld, J. H. and Pandis, S. N. , *Atmospheric Chemistry and Physics*, Wiley: New York, (1998).
- [9] J. R. Lancaster, *American Scientist* **80** (1992), 248.
- [10] Y. Nishi, T. Suzuki, and K. Kaneko, *Journal of Physical Chemistry* **101** (1997), 1938.
- [11] Johnson, J. K., *Advances in Chemical Physics*, edited by Ferguson, D. M., Siepmann, I., and Truhlar, D. G., Wiley: New York **105** (1999), 461.
- [12] S. C. McGrother and K. E. Gubbins, *Molecular Physics* **97** (1999), 955.
- [13] A. Z. Panagiotopoulos, *Molecular Physics* **62** (1987), 701.
- [14] B. Widom, *Journal of Chemical Physics* **39** (1963), 2808.
- [15] F. Kohler, M. Bohn, J. Fischer, and R. Zimmerman, *Monatshefte Chemie* **118** (1987), 169.
- [16] S. G. Kukolich, *Journal of the American Chemical Society* **104** (1982), 4715.
- [17] Steele, W. A., *Interaction of Gases with Solid Surfaces*, Pergamon: Oxford, (1974).
- [18] McQuarrie, D. A., *Statistical Mechanics*, HarperCollins: New York, (1976).

- [19] Reed, T. M. and Gubbins, K. E., Applied Statistical Mechanics, McGraw-Hill: New York, (1973).
- [20] A. L. Smith, W. E. Keller, and H. L. Johnston, Journal of Chemical Physics **19** (1951), 189.
- [21] E. A. Wade, J. I. Cline, K. T. Lorenz, C. Hayden, and D. W. Chandler, Journal of Chemical Physics **116** (2002), 4755.
- [22] A. Dkhissi, P. Soulard, A. Perrin, and N. Lacome, Journal of Molecular Spectroscopy **183** (1997), 12.
- [23] A. R. W. McKeller and J. K. G. Watson, Molecular Physics **86** (1995), 273.
- [24] R. Gonzalez-Luque, M. Merchan, and B. O. Roos, Theoretica Chimie Acta **88** (1994), 425.
- [25] B. J. Howard and A. R. W. McKeller, Molecular Physics **78** (1993), 55.
- [26] P. M. Ajayan and T. W. Ebbesen, Reports on Progress in Physics **60** (1997), 1025.
- [27] A. Kuznetsova, D. B. Mawhinney, V. Naumenko, J. T. Yates Jr., J. Liu, and R. E. Smalley, Chemical Physics Letters **321** (2000), 292.
- [28] M. Monthieux, B. W. Smith, B. Burtheaux, A. Claye, J. E. Fischer, and D. E. Luzzi, Carbon **39** (2001), 1251.
- [29] M. A. Hamon, H. Hu, P. Bhowmik, S. Niyogi, B. Zhao, M. E. Itkis, and R. C. Haddon, Chemical Physics Letters **347** (2001), 8.
- [30] D. B. Mawhinney, V. Naumenko, A. Kuznetsova, J. T. Yates, J. Liu, and R. E. Smalley, Chemical Physics Letters **324** (2000), 213.
- [31] A. Kuznetsova, J. T. Yates, V. V. Simonyan, J. K. Johnson, C. B. Huffman, and R. E. Smalley, Journal of Chemical Physics **115** (2001), 6691.
- [32] A. V. Krashennnikov, K. Nordlund, M. Sirviö, E. Salonen, and J. Keinonen, Physical Review B **63** (2001), 245405-1.
- [33] Tripathi, S., Zhang, J., and Chapman, W. G. Chemical reactions in confined spaces: a density functional approach. AICHE Annual Meeting, (2001).
- [34] S. Tripathi and W. G. Chapman, Journal of Chemical Physics (in review, 2002).
- [35] M. S. Wertheim, Journal of Statistical Physics **35** (1984), 19.
- [36] M. S. Wertheim, Journal of Statistical Physics **35** (1984), 35.

- [37] M. S. Wertheim, *Journal of Statistical Physics* **42** (1986), 459.
- [38] M. S. Wertheim, *Journal of Statistical Physics* **42** (1986), 477.
- [39] Y. Q. Zhou and G. Stell, *Journal of Chemical Physics* **96** (1992), 1504.
- [40] Frisch, M. J., Trucks, G. W., Schlegel, H. B., Scuseria, G. E., Robb, M. A., Cheeseman, J. R., Zakrzewski, V. G., Montgomery, J. A., Stratmann, R. E., Burant, J. C., Dapprich, S., Millam, J. M., Daniels, A. D., Kudin, K. N., Strain, M. C., Farkas, O., Tomasi, J., Barone, V., Cossi, M., Cammi, R., Mennucci, B., Pomelli, C., Adamo, C., Clifford, S., Ochterski, J., Petersson, G. A., Ayala, P. Y., Cui, Q., Morokuma, K., Malick, D. K., Rabuck, A. D., Raghavachari, K., Foresman, J. B., Cioslowski, J., Ortiz, J. V., Stefanov, B. B., Liu, G., Liashenko, A., Piskorz, P., Komaromi, I., Gomperts, R., Martin, R. L., Fox, D. J., Keith, T., Al-Laham, M. A., Peng, C. Y., Nanayakkara, A., Gonzalez, C., Challacombe, M., Gill, P. M. W., Johnson, B. G., Chen, W., Wong, M. W., Andres, J. L., Head-Gordon, M., Replogle, E. S., and Pople, J. A. , *Gaussian 98 (Revision A.1)*, Gaussian, Inc., Pittsburgh, PA, (1998).

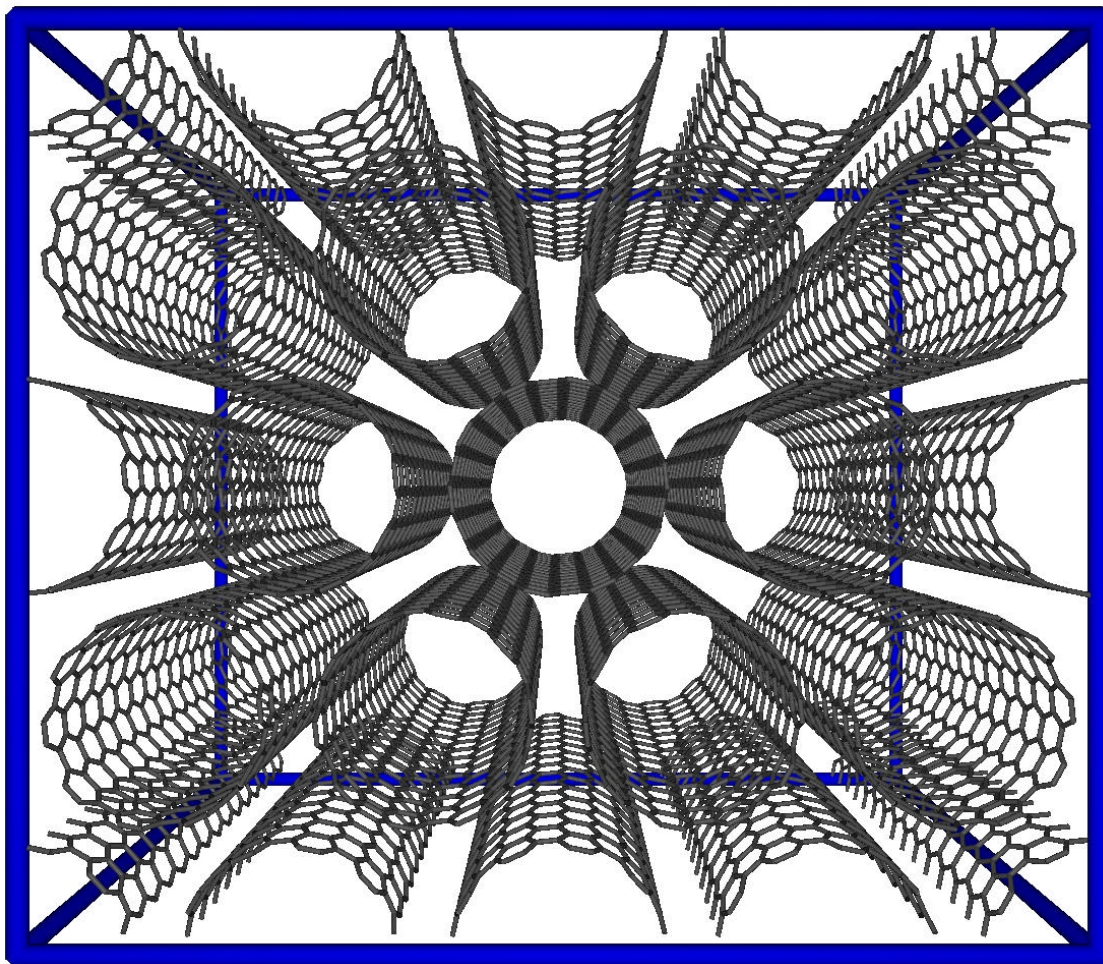


Figure 2.1 Simulation snapshot of the (10,10) carbon nanotube bundle, without defects. The nanotube diameters are 1.36 nm and the spacing between adjacent nanotubes is 0.34 nm.

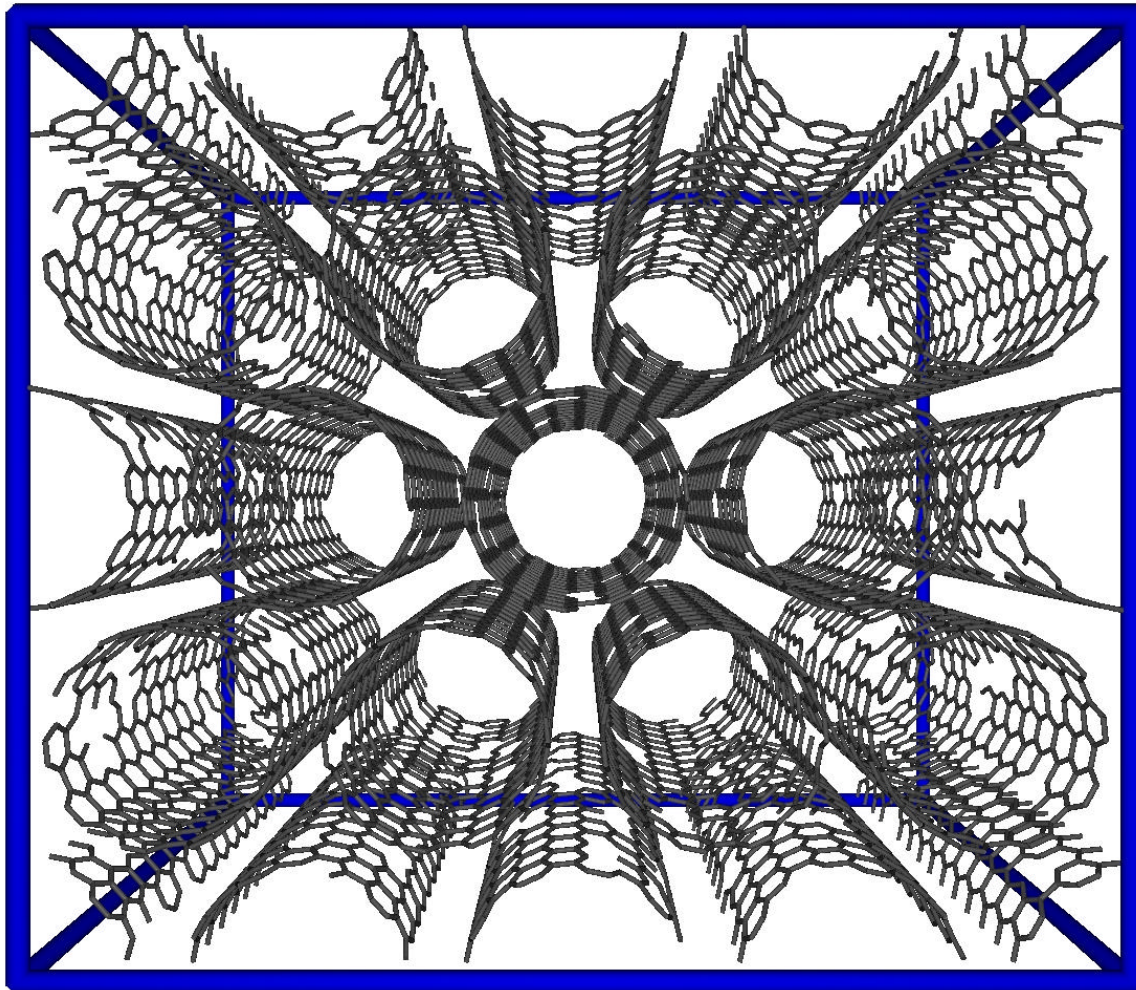


Figure 2.2 Simulation snapshot of the (10,10) carbon nanotube bundle, with 5% of the carbon atoms removed from the model. The nanotube diameters are 1.36 nm and the spacing between adjacent nanotubes is 0.34 nm.

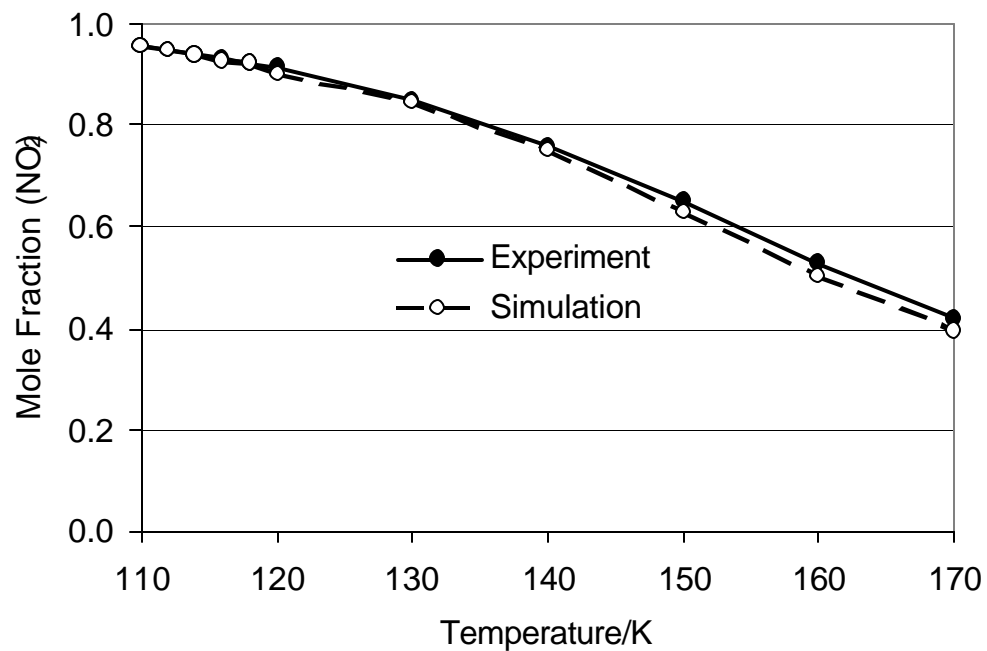


Figure 2.3 Conversion of the NO dimerization reaction in the bulk saturated liquid. Simulation results are shown with hollow circles and dashed line. Experimental results [4] from 110 to 120 K and extrapolated estimates [6] from 120 to 170 K are represented by the filled circles and solid line.

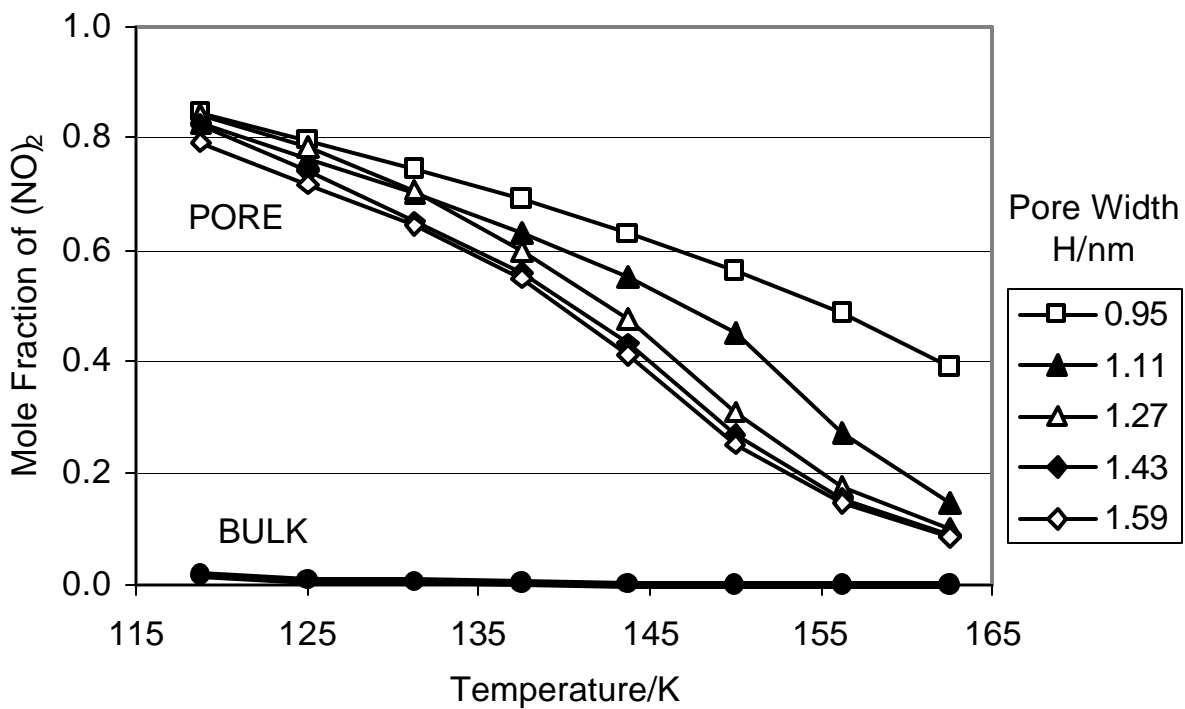


Figure 2.4 Conversion of the NO dimerization reaction within slit-shaped carbon pores, predicted from simulation. The bulk phase pressure is 0.16 bar, and the corresponding conversion in the bulk phase is shown for comparison.

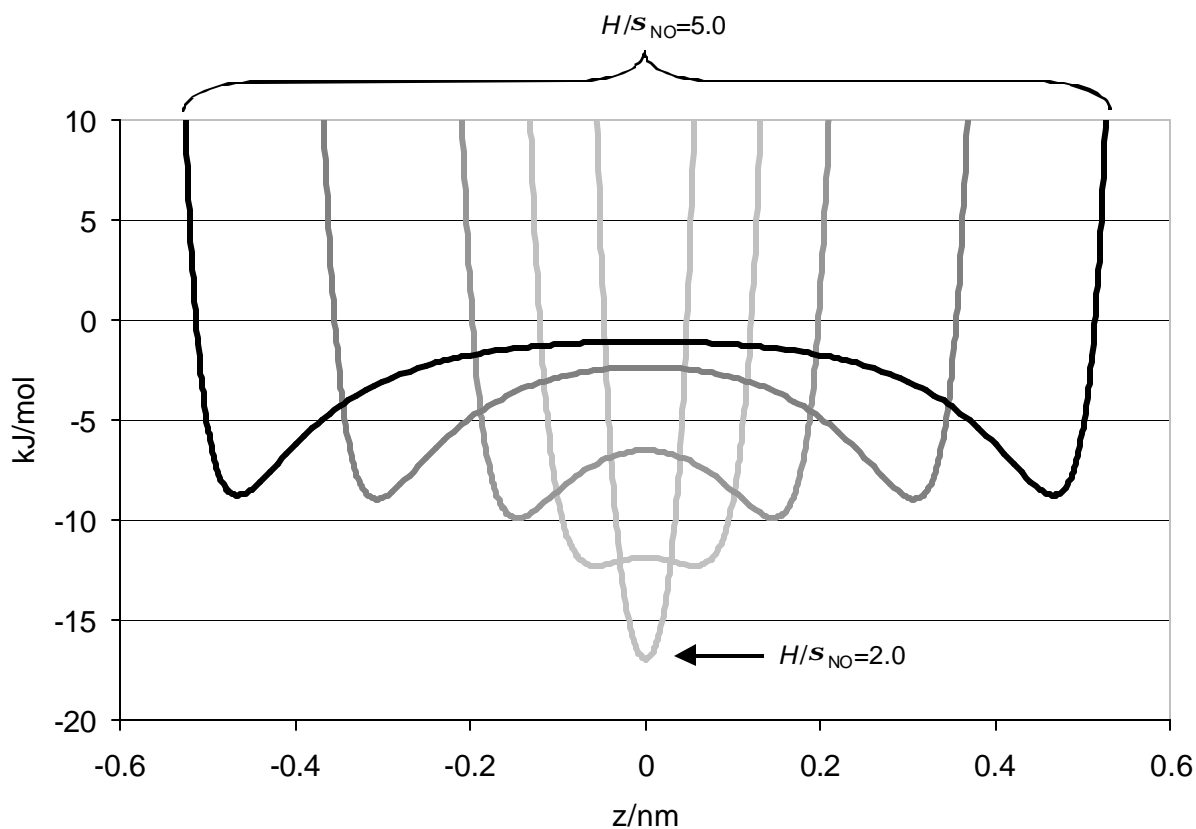


Figure 2.5 Potential energy profile of NO within slit-pores modeled with the 10-4-3 Steele potential. The pore widths in the figure are $H/s_{\text{NO}} = 2.0, 2.5, 3.0, 4.0,$ and 5.0 , beginning with the innermost curve and moving outwards. The LJ diameter of NO, s_{NO} , is 0.31715 nm.

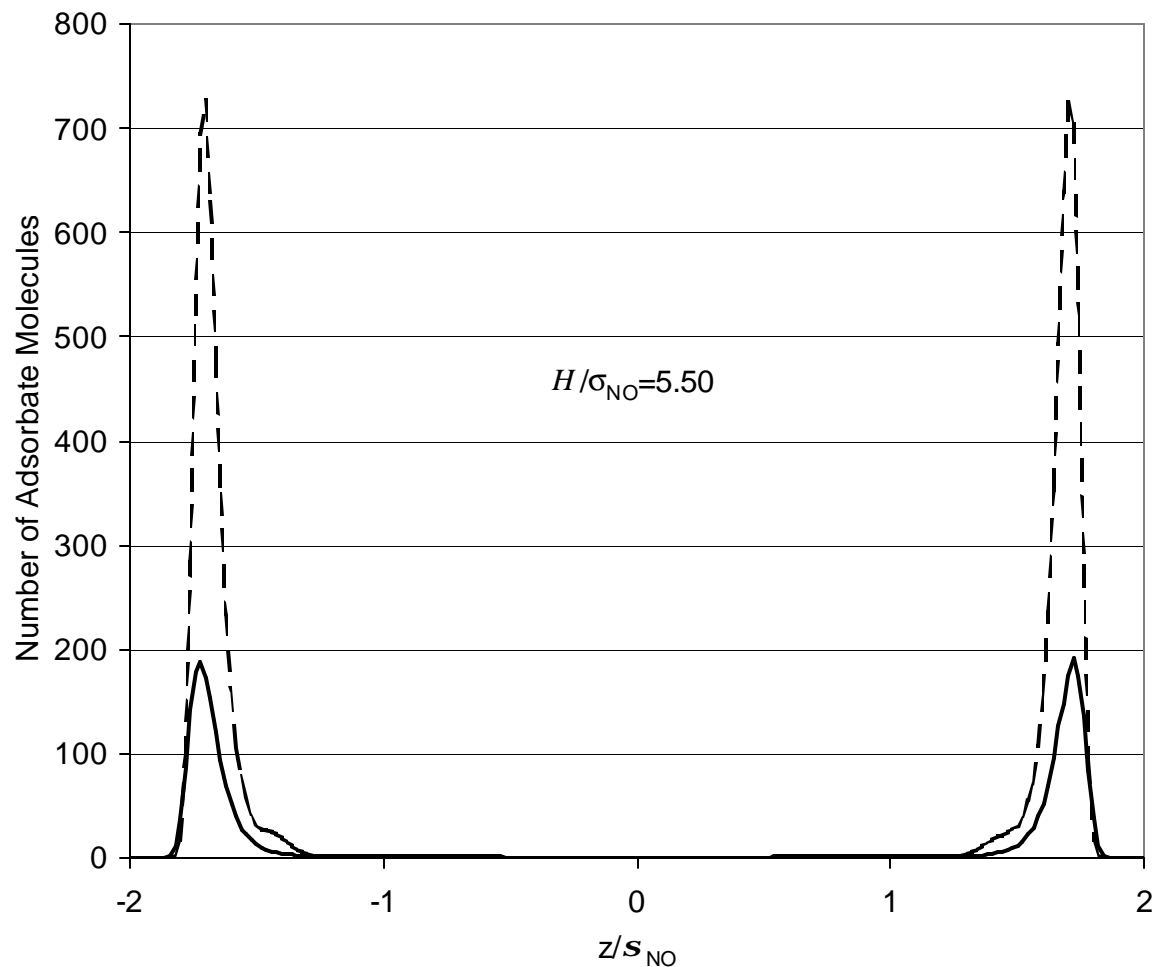


Figure 2.6 Density profiles for the NO monomers (solid line) and (NO)₂ dimers (dashed line) in the slit-pore at 125 K and 0.16 bar bulk pressure. A value of $z/s_{\text{NO}} = 0.0$ corresponds to the center of the pore.

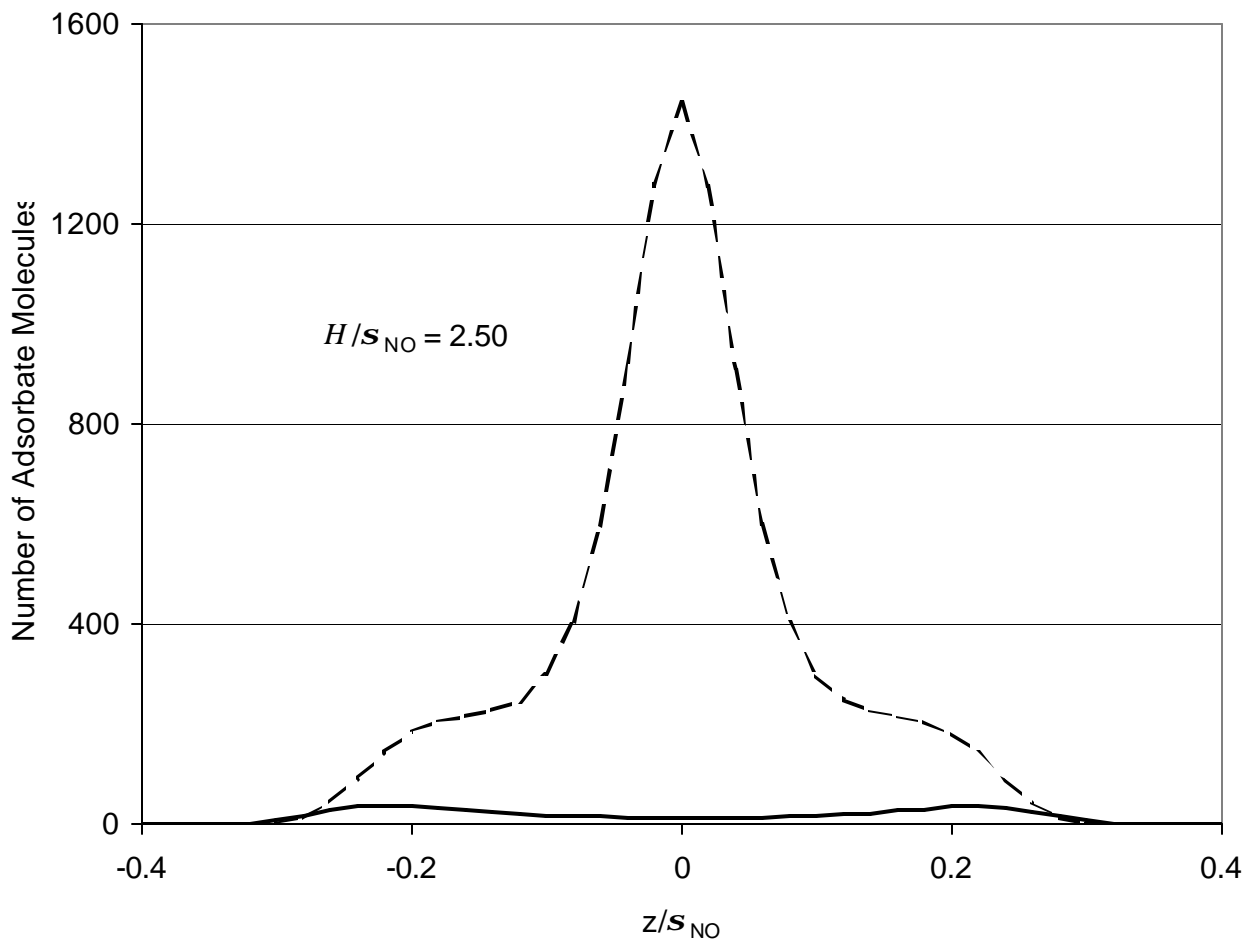


Figure 2.7 Density profiles for the NO monomers (solid line) and $(NO)_2$ dimers (dashed line) in the slit-pore at 125 K and 0.16 bar bulk pressure. A value of $z/s_{NO} = 0.0$ corresponds to the center of the pore.

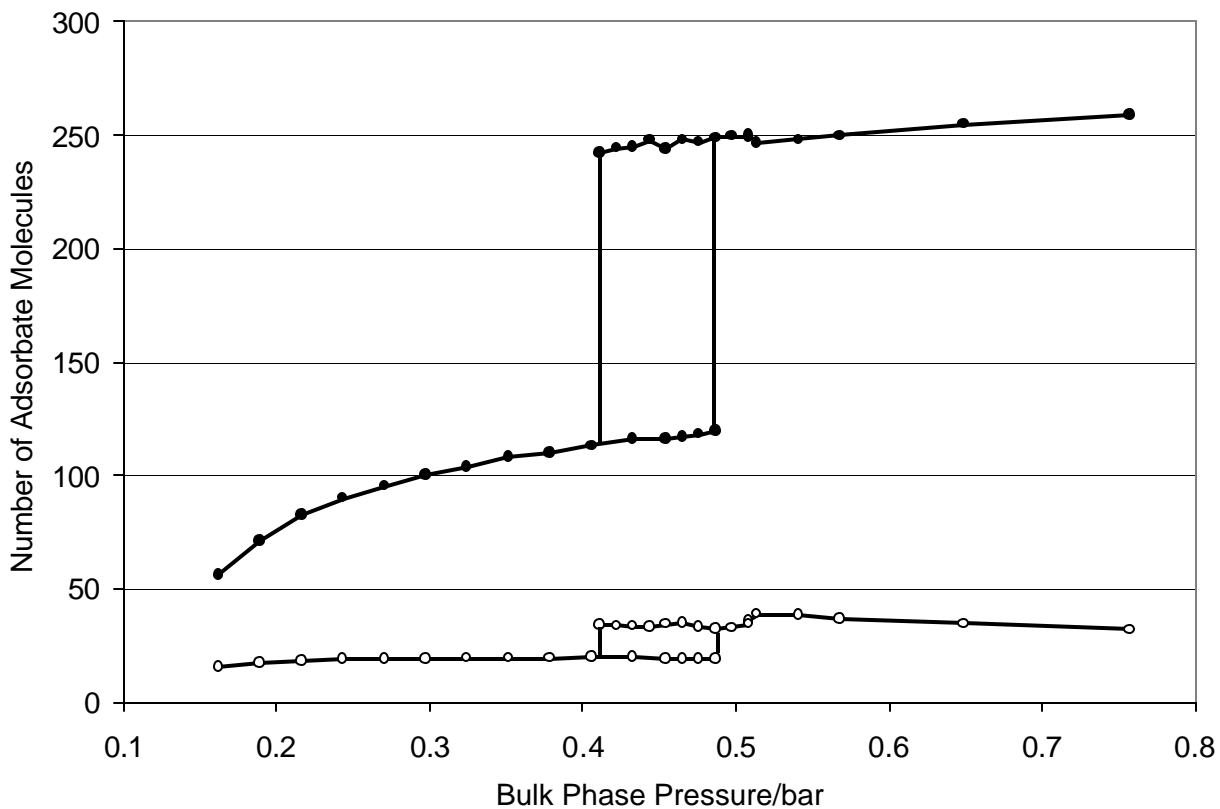


Figure 2.8 Effect of bulk gas pressure on the adsorption and reaction equilibrium at 122.5 K for a pore width of $H/s_{NO}=5.5$ (1.744 nm). Open circles and closed circles correspond to monomers and dimers, respectively, and vertical jumps represent capillary condensation (the lines are drawn as a guide to the eye).

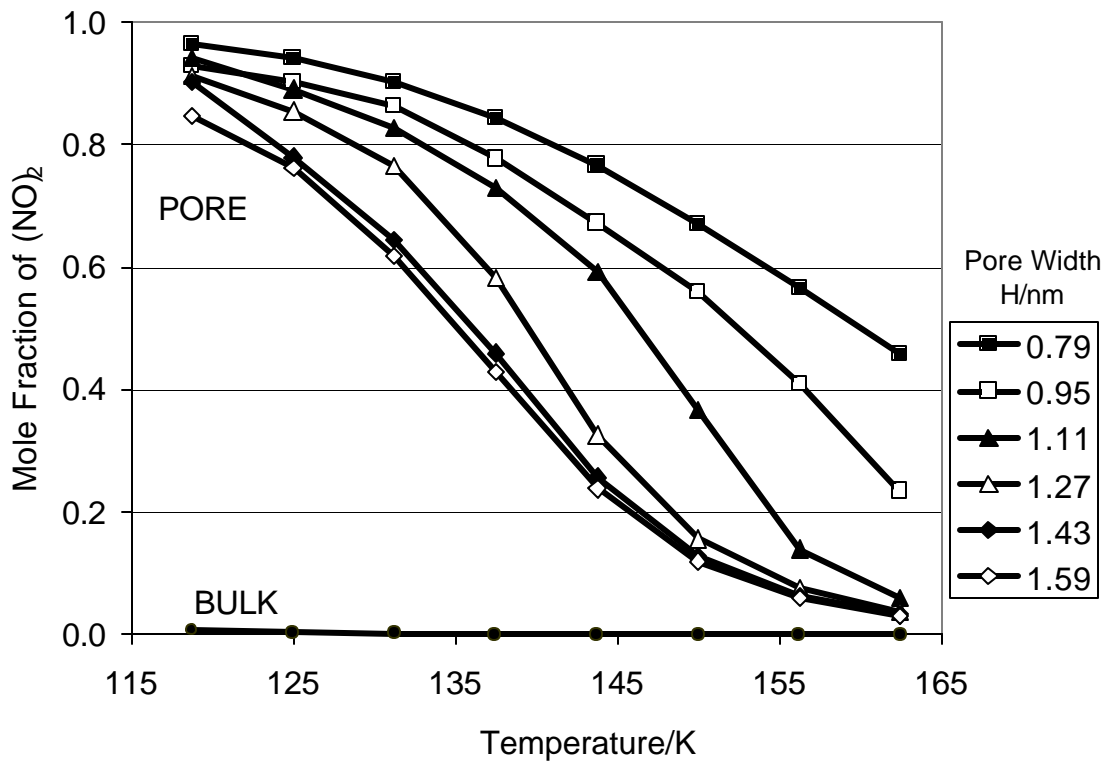


Figure 2.9 Conversion of the NO dimerization reaction within slit-shaped carbon pores, predicted from DFT [33,34]. The bulk phase pressure is 0.16 bar, and the corresponding conversion in the bulk phase is shown for comparison.

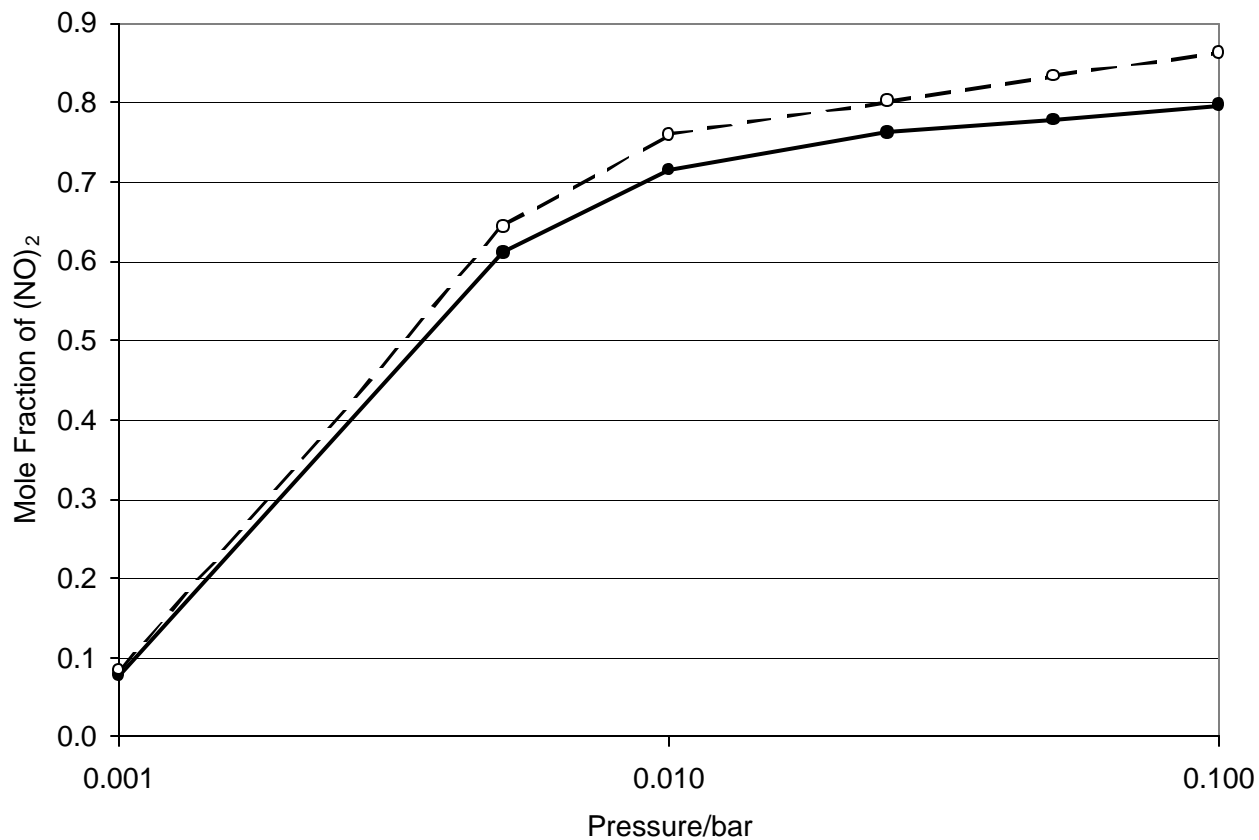


Figure 2.10 Simulated conversion of the NO dimerization reaction in the perfect (10,10) carbon nanotube bundle during RxMC simulations. The system temperature is 130 K. The solid line represents a bundle with 0.34 nm spacing between adjacent nanotubes, and the dashed line represents a tighter spacing of 0.32 nm between the tubes.

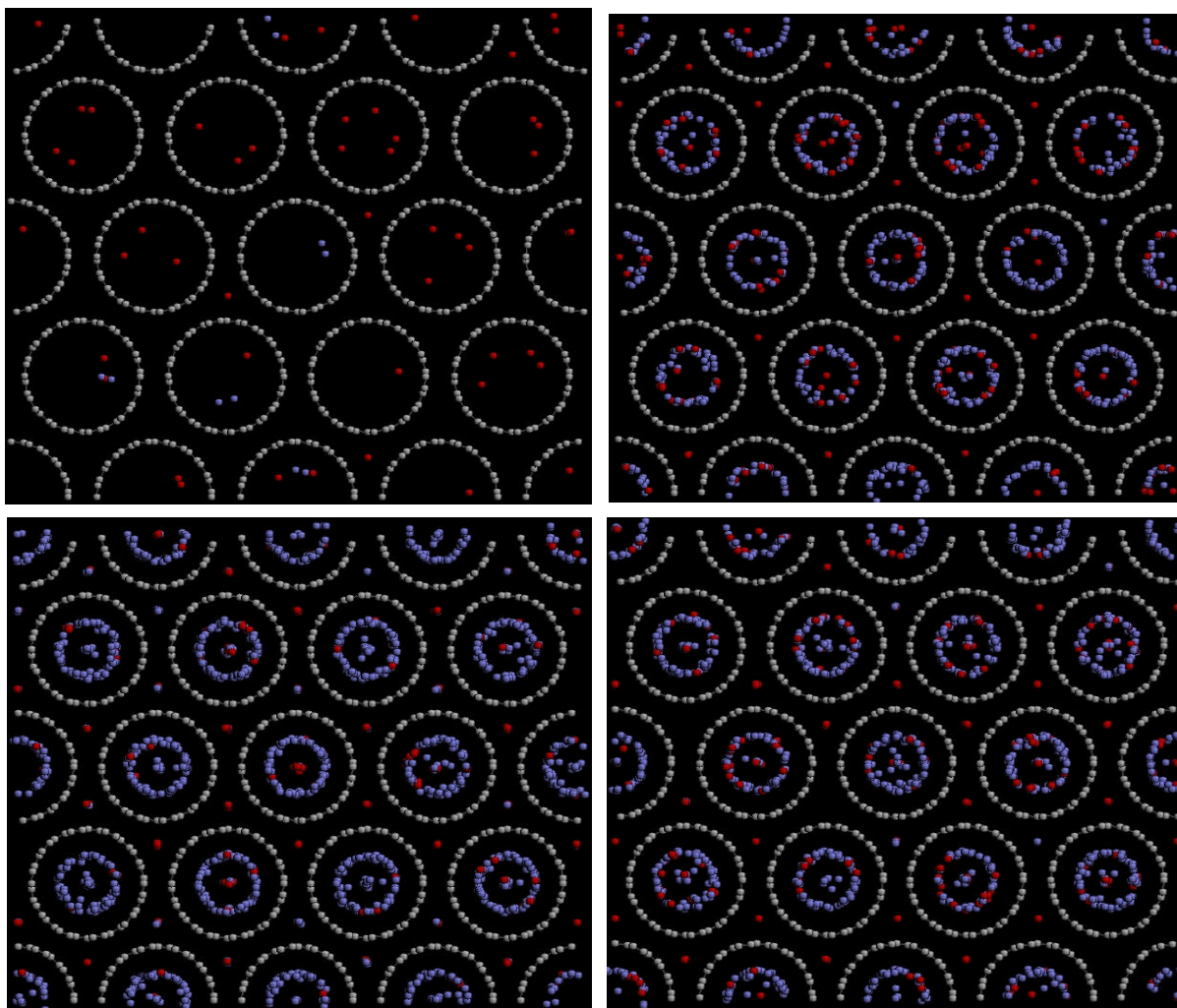


Figure 2.11 Simulation snapshots during adsorption and reaction of the nitric oxide system at a temperature of 130 K. The (10,10) nanotubes within the bundle are separated by a distance of 0.34 nm. Starting in the upper left hand corner and moving clockwise, the pressure corresponds to 0.001, 0.005, 0.010, and 0.050 bar. The NO monomers are shown in red and the $(\text{NO})_2$ dimers are shown in blue.

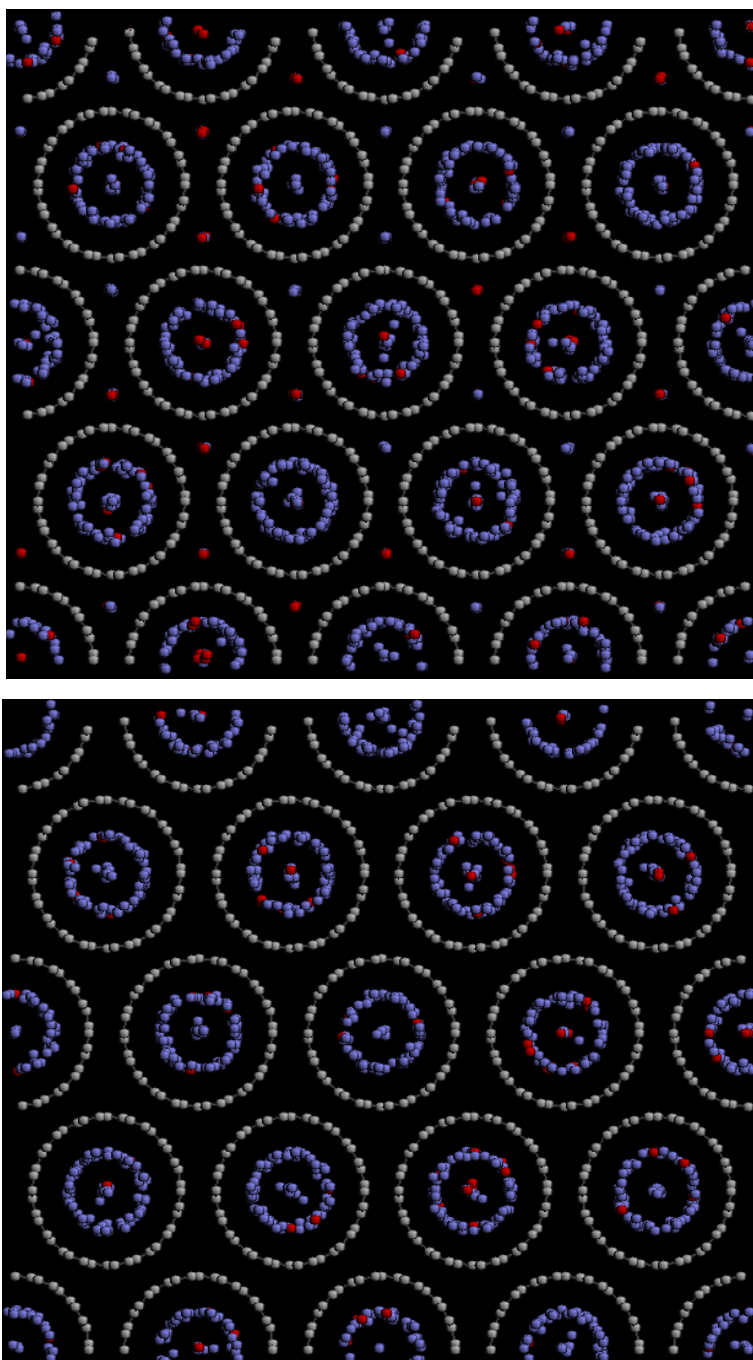


Figure 2.12 Simulation snapshot of the nitric oxide dimerization reaction in (10,10) carbon nanotubes with two different nanotube-nanotube separation distances: 0.34 nm (top) and 0.32 nm (bottom). The temperature is 130 K and the bulk phase pressure is 0.100 bar.

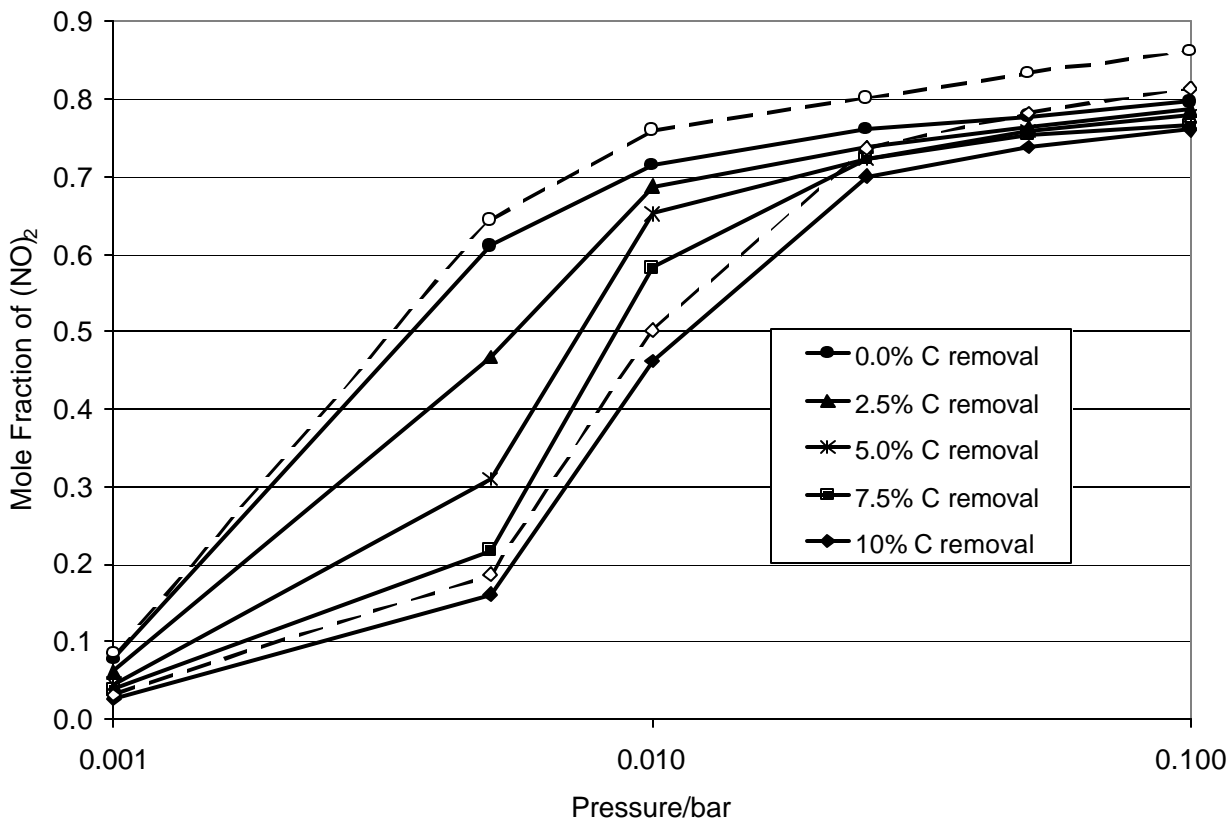


Figure 2.13 Simulated conversion of the NO dimerization reaction in the (10,10) carbon nanotube bundle during RxMC simulations. The system temperature is 130 K. The legend shows the amount of carbon removed from each bundle, in order to represent structural defects. The solid lines represent bundles with 0.34 nm spacing between adjacent nanotubes, and the dashed lines represent 0.32 nm spacing.

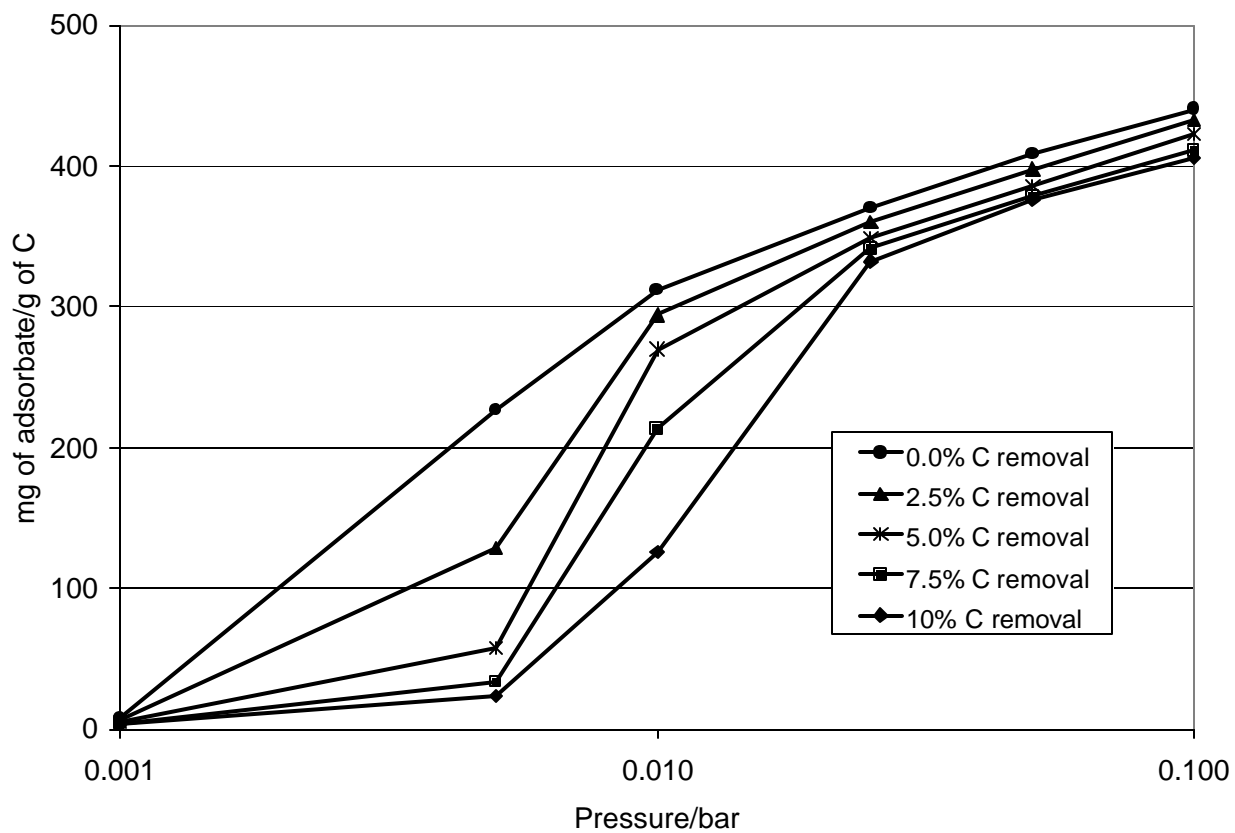


Figure 2.14 Adsorbate density in the (10,10) carbon nanotube bundle during RxMC simulations of the NO dimerization reaction with 0.34 nm spacing between adjacent nanotubes. The system temperature is 130 K.

CHAPTER 3

Ammonia Synthesis

3.1 Introduction

In this Chapter simulation results are presented for the yield of the ammonia synthesis reaction, $N_2+3H_2\leftrightarrow 2NH_3$, in several different microporous carbon models. Our work is motivated by the recent industrial interest of catalyzing the ammonia synthesis reaction with an alternative ruthenium catalyst on a carbon support instead of the traditional iron catalyst [1-4]. Based on the enhanced performance of the carbon-supported catalyst, a 600 ton/day plant began producing ammonia in 1992 using this new technology. Since the commercialization of this process, research has been devoted to optimizing the catalyst support material [5], selecting catalytic promoters [6], and understanding the structure sensitivity of this reaction [2].

The current simulations have been designed to supplement the growing interest of Ru/C catalysts by providing simulation studies of ammonia synthesis in several different microporous carbon support structures. We have focused primarily on the geometrical and chemical heterogeneity of microporous carbons and how these characteristics influence the equilibrium yield of ammonia. In this study, Reactive Monte Carlo (RxMC) [7] simulations are used to calculate the yield of ammonia in four different types of carbon models: a smooth slit-shaped carbon pore, a smooth slit-shaped carbon pore decorated with carboxyl (-COOH)

groups, a realistic coconut shell carbon model, and an atomistic carbon nanotube model.

Using these four microporous carbon models, we are able to determine the most significant pore characteristics for the yield of ammonia.

The fundamental nature of this work is motivated by the fact that porous materials are used extensively as catalysts and catalyst supports in industrial chemical reactions. However, there has been relatively little fundamental theoretical or simulation work performed to evaluate the effects of physical confinement on chemical reaction equilibria [8-10]. There are several effects that should be considered to be important. First, the pore phase is typically at a higher density than the coexisting bulk phase, due to the strong adsorption potential of the porous material. Furthermore, reactions will be influenced by selective adsorption of the reactant and product molecules, depending on the nature of the material and the specific reaction. Finally, the geometrical structure of the pores can favor certain products, when the pores are of molecular dimensions [1,11]. In this Chapter, we explore all of these phenomena as related to the ammonia synthesis reaction.

3.2 Simulation Methods

3.2.1 Reactive Monte Carlo

In this study, we use the Reactive Monte Carlo (RxMC) simulation technique [7,12-14] (reviewed in Chapter 1) in order to predict the reaction yield within each of the carbon models. Attractive features of this method are that equilibrium yield can be predicted for reactions that involve a change in the number of moles, multiple simultaneous reaction

equilibria, or multi-phase reacting systems. The only information necessary for predicting reaction equilibria using this technique are the molecular partition functions (q_i) for each of the reacting species, in addition to accurate potentials for describing the intermolecular interactions. The constant pressure version of RxMC, applied to the ammonia synthesis reaction in the bulk phase, involves the following trial moves, with the forward and reverse reaction steps being accepted with the designated probability. The forward and reverse reaction steps are directly derived from Eq. (2.4) in Chapter 2.

- (A) **Move/Rotation:** a change in the position or orientation of a molecule chosen at random;

$$P_{acc} = \min [1, \exp(-\mathbf{bd}U)] \quad (3.1)$$

- (B) **Forward Reaction Step:** reactant molecules are chosen at random and changed to product molecules ($\text{N}_2 + 3\text{H}_2 \rightarrow 2\text{NH}_3$);

$$P_{acc} = \min \left[1, \exp(-\mathbf{bd}U_F) \times \frac{q_{\text{NH}_3}^2}{q_{\text{N}_2} q_{\text{H}_2}^3} \times \frac{(N_{\text{N}_2})(N_{\text{H}_2})(N_{\text{H}_2} - 1)(N_{\text{H}_2} - 2)}{(N_{\text{NH}_3} + 1)(N_{\text{NH}_3} + 2)} \right] \quad (3.2)$$

- (C) **Reverse Reaction Step:** product molecules are chosen at random and changed to reactant molecules ($2\text{NH}_3 \rightarrow \text{N}_2 + 3\text{H}_2$);

$$P_{acc} = \min \left[1, \exp(-\mathbf{bd}U_R) \times \frac{q_{\text{N}_2} q_{\text{H}_2}^3}{q_{\text{NH}_3}^2} \times \frac{(N_{\text{NH}_3})(N_{\text{NH}_3} - 1)}{(N_{\text{N}_2} + 1)(N_{\text{H}_2} + 1)(N_{\text{H}_2} + 2)(N_{\text{H}_2} + 3)} \right] \quad (3.3)$$

- (D) **Volume Change:** a random change in the bulk gas phase volume in order to maintain the bulk pressure constant.

$$P_{acc} = \min [1, \exp \{- \mathbf{b} [dU_V + P dV_B - N \mathbf{b}^{-1} \ln (V_{B,n} / V_{B,o})]\}] \quad (3.4)$$

In the above equations, \mathbf{b} is the reciprocal of the Boltzmann constant times the temperature, N_i is the number of molecules of component i present in the system, and q_i is the intramolecular partition function for molecular species i . In the volume change steps, $V_{B,o}$ is the original volume, $V_{B,n}$ is the new system volume, and dV_B is the difference between these two volumes, $V_{B,n} - V_{B,o}$. The symbols dU_F , dU_R , and dV_B represent the changes in the configurational energy of the system for forward reaction, reverse reaction, and volume change steps, respectively. For instance, dU_F signifies the change in the configurational energy required to remove one N_2 and three H_2 molecules and insert two NH_3 molecules into the system. In order to maintain microscopic reversibility within the reacting system, the forward and reverse reaction steps, (B) and (C) above, must be attempted with equal probability. During the forward and reverse reaction steps, the newly created molecules are placed in the cavities left by the deleted molecules, which tends to aid in convergence at the higher densities. When the reaction step involves an increase in mole number, such as in step (C), the excess molecules are inserted randomly into the fluid. In simulations, these reacting systems were typically equilibrated for 1×10^6 moves and averages taken for 3×10^6 moves, with moves (A), (B), (C), and (D) selected 39.9%, 30%, 30%, and 0.1% of the time, respectively.

3.2.2 Constant Pressure Gibbs Ensemble Monte Carlo

The overall objective in this study was to measure the shift in conversion of a reaction confined within a carbon micropore as compared to an unconfined phase, or *bulk* phase, that is in equilibrium with the confined phase. In order to perform these two-phase simulations, between a pore phase and a bulk phase, we implemented a simulation technique called constant pressure Gibbs Ensemble Monte Carlo [15,16]. This technique permits the use of a constant pressure bulk phase, without specifying chemical potentials or fugacities. This two-phase simulation technique is easily combined with the RxMC framework shown previously, by incorporating particle swaps between the bulk phase and the pore phase. The acceptance probabilities for these exchange moves are shown in Eqs. (3.5) and (3.6):

(A) **Bulk to Pore** : particle transfer from the bulk phase to the pore phase:

$$P_{acc} = \min \left[1, \exp \left(- \mathbf{b}dU_{N_{B,i}-1} - \mathbf{b}dU_{N_{P,i}+1} \right) \times \frac{N_{B,i}V_P}{(N_{P,i}+1)V_B} \right] \quad (3.5)$$

(B) **Pore to Bulk** : particle transfer from the pore phase to the bulk phase:

$$P_{acc} = \min \left[1, \exp \left(- \mathbf{b}dU_{N_{P,i}-1} - \mathbf{b}dU_{N_{B,i}+1} \right) \times \frac{N_{P,i}V_B}{(N_{B,i}+1)V_P} \right] \quad (3.6)$$

In Eqs. (3.5) and (3.6), $N_{P,i}$ and $N_{B,i}$ represent the number of molecules of type i in the pore and bulk phase, respectively. V_B is the volume of the bulk phase and V_P is the volume of the pore phase. The exponential term in Eqs. (3.5) and (3.6) accounts for the total change in potential energy associated with the particle transfer. All but one of the molecular species

participating in the reaction needs to be swapped between the two phases, as the equilibrium of the last species will be completely satisfied by the RxMC reaction steps within each of the discrete phases. In order to increase sampling efficiency, only the smaller species should be exchanged between the bulk and the pore. Consequently, in our simulations, only nitrogen and hydrogen were exchanged. It is important that a molecular species be transferred from the bulk phase to the pore phase with a probability equal to its transfer from the pore phase to the bulk phase, for this technique to be valid. The chemical potential of each species, \mathbf{m} , was calculated in several different simulations in order to confirm that the chemical equilibrium between the reacting species, $\sum \mathbf{n}_i \mathbf{m}_{i,bulk} = \sum \mathbf{n}_i \mathbf{m}_{i,pore} = 0$, and the equilibrium between the two phases, $\mathbf{m}_{i,bulk} = \mathbf{m}_{i,pore}$, was maintained, where \mathbf{n}_i is the stoichiometric coefficient of component i (negative for reactants and positive for products).

3.2.3 Reverse Monte Carlo

One of the microporous carbon models used in this work is a structural model of a coconut shell activated carbon developed by Jorge Pikunic [10,17]. The name of the activated carbon reflects the fact that coconut shells are used as the starting material in its production process. Pikunic's simulation model was built from the experimental diffraction data of the coconut shell carbon, using a simulation protocol based on Reverse Monte Carlo [18]. The goal is to produce an atomic configuration that is consistent with a set of experimental structure data. The method consists of changing the positions of groups of atoms in a simulation box through a stochastic procedure. Using the Metropolis algorithm, these moves are accepted or rejected based on the agreement between some simulated structural property and a

corresponding experimental target. During the progress of the simulation, the differences between the simulated and the target functions are minimized. Since the experimental $g(r)$ was used as the target function for the current model, the appropriate quantity to be minimized is:

$$\mathbf{c}^2 = \sum_{i=1}^{n_{exp}} [g_{sim}(r_i) - g_{exp}(r_i)]^2 \quad (3.7)$$

where n_{exp} is the number of experimental points, $g_{sim}(r_i)$ is the simulated $g(r)$ and $g_{exp}(r_i)$ is the experimental $g(r)$ evaluated at r_i . After each move, the quantity \mathbf{c}^2 is calculated and the move is accepted with probability P_{acc} , shown in Eq. (3.8). In Eq. (3.8), P_c is a weighting parameter. Note that when P_c is set to infinity, the moves are only accepted if $\mathbf{c}_{new}^2 < \mathbf{c}_{old}^2$.

$$P_{acc} = \min \left[1, \exp \left\{ -P_c \left(\mathbf{c}_{new}^2 - \mathbf{c}_{old}^2 \right) \right\} \right] \quad (3.8)$$

In conjunction with the minimization procedure, the following constraints were imposed to eliminate unphysical features in the model: (1) any atom can only have two or three neighbors, (2) all the interatomic distances are 1.42 Å, (3) all bond angles are 120°. When these three constraints are applied together, it is possible to generate basic carbon units. These units are rigid aromatic sheets of sp^2 bonded carbon which resemble the structure of graphene sheets.

Once convergence is achieved, the final configuration of the atoms is saved and then used later as one of the four microporous carbon models in the ammonia synthesis simulations.

For additional information about the details of the model construction, see references [10,17].

3.3 Simulation Models

3.3.1 Molecular Models

In all simulations, the configurational energy between any two molecules, i and j , is represented by the site-site Lennard-Jones (LJ) plus Coulomb potential:

$$u_{i,j} = \sum_a \sum_b 4\mathbf{e}_{ia,jb} \left[\left(\frac{\mathbf{s}_{ia,jb}}{r_{ia,jb}} \right)^{12} - \left(\frac{\mathbf{s}_{ia,jb}}{r_{ia,jb}} \right)^6 \right] + \frac{q_{ia}q_{jb}}{r_{ia,jb}} \quad (3.9)$$

In Eq. (3.9), the sum is calculated over the sites (\mathbf{a}) on molecule i with each site (\mathbf{b}) on molecule j , $r_{ia,jb}$ is the separation distance between sites on different molecules, and the interaction parameters \mathbf{s} , \mathbf{e} , and q are specific to each molecular species, as shown in Table 3.1. The interaction sites on each molecule are found at a distance of ' bl ' from the molecule center of mass. All of the molecules are linear with the exception of ammonia, which has a HNH bond angle of 110.9° [19]. The cross-term interaction parameters between unlike species in the potential were calculated using the Lorentz-Berthelot mixing rules: $\mathbf{e}_{ia,jb} = (\mathbf{e}_{ia}\mathbf{e}_{jb})^{1/2}$ and $\mathbf{s}_{ia,jb} = (\mathbf{s}_{ia} + \mathbf{s}_{jb})/2.0$. Before making predictions of the conversion in the carbon pores, the molecular models used in the ammonia synthesis simulations have been first verified by reproducing the experimental conversion in the bulk gas phase [19]. The results of the bulk phase comparison are presented in Section 3.4, along with adsorption isotherms in carbon slit-pores using the chosen nitrogen and hydrogen models.

Table 3.1 Summary of potential parameters used in the ammonia simulations.

molecule	site	bl/nm	q/e	s/nm	$e/k_b/K$	reference
NH ₃	1	0.0	0.0	0.332	36.4	[20]
	2	0.10124	+0.485	0.225	21.1	
	3	0.10124	+0.485	0.225	21.1	
	4	0.10124	+0.485	0.225	21.1	
	5	0.0156	-1.455	0.0	0.0	
N ₂	1	0.055	-0.40505	0.332	36.4	[21]
	2	0.055	-0.40505	0.332	36.4	
	3	0.0	+0.81010	0.0	0.0	
H ₂	1	0.0	0.0	0.2915	38.0	[22]
C (pore)	1	0.0	0.0	0.340	28.0	[23]

3.3.2 Microporous Carbon Models

RxMC simulations of the ammonia synthesis reaction have been performed in four distinct microporous carbon models. These carbon models, which are listed below, are chosen to reproduce the general structure and surface chemistry of realistic microporous carbons used in experiments. For simplicity and clarity, these models are labeled as smooth, activated, coconut, and nanotubes, as designated below.

- (A) **Smooth:** smooth, slit-shaped graphitic pores
- (B) **Activated:** smooth, slit-shaped graphitic pores, activated with surface carboxyl groups
- (C) **Coconut:** atomistic, graphitic pores, which include surface corrugation and connectivity, modeling carbon produced from coconut shells
- (D) **Nanotubes:** atomistic, single-walled carbon nanotubes, in a hexagonal array

The following sections give the structural and energetic details unique to each of the microporous carbon models used in these simulations.

A. Smooth Slit-Shaped Pore

We modeled the smooth slit-shaped carbon pore using the structureless 10-4-3 Steele potential [23], shown in Eq. (3.10). This model assumes that the carbon pore is constructed of two parallel walls that are infinite in the x-y plane. The structure of these walls is assumed to be that of graphene sheets, and the surface corrugation is neglected by averaging the carbon potential over the two graphitic pore surfaces. As a result, the interaction potential between an adsorbate molecule and the pore wall is only a function of the z-coordinate, the distance from each pore wall:

$$U_{ia,c}(z) = 4pe_{ia,c}s_{ia,c}^2\Delta r_c \left[\frac{1}{5} \left(\frac{s_{ia,c}}{H/2 \pm z} \right)^{10} - \frac{1}{2} \left(\frac{s_{ia,c}}{H/2 \pm z} \right)^4 - \frac{s_{ia,c}^4}{6\Delta(H/2 \pm z + 0.61\Delta)^3} \right] \quad (3.10)$$

In equation (3.10), H is the width of the pore, defined as the distance between carbon centers on the two opposing walls of the pore, Δ is the experimentally measured interlayer spacing of graphite (0.335 nm), r_c is the experimentally measured density of graphite (2.27 g/cm³), and e and s are the LJ parameters listed in Table 3.1.

B. Activated Carbon Pore

The second microporous carbon model used in these simulations, the activated carbon pore, is similar to the smooth slit-pore model just described. The only difference is that carboxyl surface groups are added to the smooth carbon surface in order to mimic the chemical activation that is often applied in experiments. The experimental activation process typically

increases the surface area and adsorption capacity of the carbon, while the carbon surface is chemically altered by the addition of hydroxyl, carboxyl, quinone, peroxide, and aldehyde groups [24]. For simplicity, the activated sites on the carbon pore surface were all modeled as carboxyl (-COOH) groups with varying site densities, according to Shevade *et al.* [25]. The carboxyl group is planar, with the geometry shown in Figure 3.1. The interaction potential between these activated sites and the adsorbate molecules are modeled with the potential of Eq. (3.9), with the parameters of -COOH shown in Table 3.2, and the interaction between the adsorbate molecules and the carbon surface is modeled with Eq. (3.10).

Table 3.2 Summary of the potential parameters for -COOH sites [25].

Molecule	Site	q/e	s/nm	e/k _B /K
-COOH	1 (C*)	0.08	0.340	28.0
	2 (C)	0.55	0.375	52.8
	3 (=O)	-0.50	0.296	105.7
	4 (O)	-0.58	0.300	85.6
	5 (H)	0.45	0.0	0.0

* Anchor carbon on the graphite basal plane.

C. Coconut Shell Carbon

The RMC simulation method, described in Section 3.2, was used to generate the coconut shell carbon model. The simulation cell length was 11 nm, and the target density was 1.90 g/ml, based on the actual carbon density estimated by helium pycnometry [26]. A structural representation of this model is shown in Figure 3.2. The simulated and the target $g(r)$ are shown in Figure 3.3.

The experimental and the simulated $g(r)$ are in overall good agreement. Deviations are seen in the first four peaks (r less than $\sim 6 \text{ \AA}$). In this range of r , the structure of the model is driven by the constraints imposed in the simulation. The three constraints applied by Pikunic in this approach do not allow the appearance of any defects, such as rings of 5 or 7 carbon atoms, which would cause curvature in the plates. These irregularities of the graphene layers can be introduced by allowing the bond angles and bond distances to change about an equilibrium value [17]. However, the current RxMC simulations focus on the effect of the energetic heterogeneity caused by connectivity, variation in size and shape of the graphene sheets, and number of graphene sheets that are stacked to form the pore walls. It can be seen in Figure 3.2 that there is a nematic order (little orientational disorder) in the structure. Figure 3.2 represents only a small slice ($\sim 1.5\%$) out of the actual carbon model used in our simulations, which is composed of approximately 130,000 carbon atoms.

All the carbon atoms in the coconut shell model are assumed to have sp^2 hybridization and each carbon atom is bonded to 2 or 3 other atoms. Based on the experimental composition [26], it is assumed that the amount of oxygen and other heteroatoms is negligible and thus, the material is composed entirely of carbon and hydrogen. The interaction between each carbon site and an adsorbate molecule is modeled with the site-site LJ potential (without electrostatic interactions). This is in contrast to the smooth slit-pore model, in which the surface corrugation is neglected and the interactions with neighboring graphite layers are averaged together. The LJ parameters used for the carbon sites are the same as those used for the smooth models listed in Table 3.1.

D. Carbon Nanotube Model

We modeled the carbon nanotubes by using explicit carbon atoms, with site-site LJ interactions (without electrostatic interactions) between the carbon atoms and the adsorbate molecules. The nanotubes are modeled as single-walled carbon nanotubes, arranged in a hexagonal array, as is often found in experiments. Nanotubes can be uniquely defined in terms of their helicity, and according to the standard convention [27], the nanotubes in our model are designated as (8,8), (9,9), and (10,10) nanotubes. This is essentially an armchair type of structure, with 8, 9, and 10 carbon rings forming the circumference of the cylinder, respectively. Figure 3.4 shows the bundled nanotube configuration used in these simulations. Periodic boundary conditions are applied in all three coordinate directions, and adsorption and reaction are allowed within the nanotubes and in the interstitial spaces between adjacent nanotubes.

3.4 Results and Discussion

The effect of confinement on the ammonia reaction in the two-phase system is more complex than for the nitric oxide reaction presented in Chapter 2, and provides an interesting comparison. In contrast to the nitric oxide reaction, the molecules in this system experience selective adsorption in the pore phase, due to the differing adsorption characteristics of the N_2 , H_2 , and NH_3 . Also, there are now three components in the mixture, which further complicates the reaction and phase equilibrium.

3.4.1 Conversion in the Bulk Gas Phase

In order to validate our molecular models and algorithms, we first carried out RxMC simulations for the ammonia synthesis reaction in the bulk gas phase using an isothermal-isobaric (NPT) ensemble. Due to the abundance of experimental data, we were able to make comparisons of simulation and experiment over a broad range of temperatures and pressures. The reference data that we used for the ammonia reaction comes from an analytical expression for the equilibrium composition developed by Gillespie and Beattie [28], which accurately reproduces experimental measurements of ammonia conversion within the experimental uncertainty over a large temperature and pressure range. We compared our simulated mole fraction of ammonia to this analytical expression over a temperature range of 573 K to 873 K and over a pressure range of 100 to 1000 bar, with the results shown in Figure 3.5. All of the bulk phase ammonia simulations were performed with an initial N:H ratio of 1:3, as in the experiments. We modified the bond energy of the NH bond, given in reference [29] by less than 0.2% (to a final value of 385.8 kJ/mol) in order to achieve a close match with the reference data at the lowest temperature. Considering the wide range of temperature and pressure conditions, the agreement is very good. The heat of reaction of the ammonia synthesis reaction was also calculated using a van't Hoff plot and the result was 45.2 kJ/mol of NH_3 . This agrees with the value calculated from the heats of formation of the individual molecules of 45.9 kJ/mol [30] and the experimental value of 44.39 kJ/mol [28].

As a further test of our molecular models, we simulated the ammonia reaction in the presence of two inert components, methane and argon, and compared these results with experimental

data. The same molecular models for the N₂, H₂, and NH₃ like-pair interactions were used. The ratio of N:H was held constant at 1:3, and methane and argon were added in amounts of 7.5 mol% and 2.5 mol% respectively and were modeled as LJ spheres [22]. Again, we compared our simulation results with data from the work of Gillespie and Beattie [28]. The results are shown in Figure 3.6. The agreement is again good, considering the wide temperature and pressure range.

3.4.2 Pure Component Adsorption Isotherms

Before studying this reaction in the carbon pore, we first tested the adsorption characteristics of the pure components. We carried out constant pressure Gibbs ensemble Monte Carlo simulations to determine the adsorption isotherms of pure N₂ and pure H₂ in our slit-pore model, and confirmed that our models could accurately reproduce experimental adsorption isotherms in activated carbon fibers [31,32]. The comparisons are shown in Figures 3.7 and 3.8, which show close agreement with the experimental results. It is noted that the adsorption of H₂ is slightly over-predicted in our simulations. After performing these checks, we then carried out RxMC simulations for the reaction in the carbon pores in equilibrium with the bulk phase, again using an overall N:H ratio of 1:3.

3.4.3 Smooth Slit-Shaped Pore

Having verified our simulation results in the bulk gas phase and with the pure component adsorption isotherms, we began by performing the two-phase RxMC simulations of ammonia synthesis between a bulk phase and the smooth slit-pore, modeled with the 10-4-3 Steele

potential [23]. These simulations were performed over a distribution of pore widths ranging from about 0.8 nm to 1.5 nm, which are pore widths characteristic of microporous carbons. The reacting conditions of 100 bar and 573-773 K were chosen in order to compare with the typical industrial operating conditions for the production of ammonia [19].

The results for these RxMC simulations in the smooth slit-pores are shown in Figure 3.9. It is readily apparent that the reaction yield in the pore is enhanced when compared to the bulk phase yield. Furthermore, the conversion within the pore increases as the pore width decreases. This enhancement is in part due to the increased density within the pore phase, as the smaller pores are more adsorptive than the larger pores. The total adsorbate density within several different pore widths is shown in Table 3.3, and reflects the fact that the conversion increase within the pores can be well-correlated to the total adsorbate density. In Table 3.3, the adsorbate density is calculated from the accessible pore volume, with the accessible pore width H' defined as: $H'=H-s_{\text{carbon}}$.

Table 3.3 Simulated density within the bulk phase and in several different pore sizes, corresponding to a bulk phase pressure of 100 bar.

Temperature/K	573	623	673	723	773
	Density (g/cm ³)				
0.83 nm pore	0.1009	0.0720	0.0538	0.0415	0.0338
1.16 nm pore	0.0642	0.0461	0.0353	0.0281	0.0236
1.49 nm pore	0.0518	0.0380	0.0299	0.0244	0.0207
Bulk	0.0268	0.0218	0.0183	0.0158	0.0141

While narrower pores generally tend to increase the conversion, the conversion within the slit-pore is limited by geometric factors when the pore width becomes too small. Below a

pore width of about 0.65 nm, the conversion quickly declines, as the formation of the ammonia molecule is limited by the proximity of the pore walls (Figure 3.10).

The trends in the ammonia conversion are qualitatively similar to those observed for the nitric oxide dimerization reaction presented in Chapter 2. However, the increase in yield within the pores is smaller in the case of the NH_3 synthesis reaction. This is a result of the higher (supercritical) temperatures, and also of the selective adsorption of N_2 over H_2 in the pores. The change in the ammonia concentration with temperature in the pores is less pronounced than for the NO dimerization (Figure 2.4), which is due to a more gradual decrease in adsorbate density with temperature for the NH_3 synthesis reaction.

In the case of the NO dimerization, there is only one reactant and selective adsorption of reactants does not arise. For the ammonia synthesis reaction, equilibrium is further complicated due to selective adsorption of the reactant molecules in the pore. Nitrogen is preferentially adsorbed over hydrogen, and this effect is more pronounced at low pressures, where fluid-wall interactions dominate the adsorption. Thus, the ratio of N:H within the pore phase was not constant, and selective adsorption of N_2 at the lower pressures caused the N:H ratio to deviate from the ideal value of 1:3. Table 3.4 shows the selectivity of N_2 over H_2 in a $2.5\sigma_{\text{N}_2}$ (0.83 nm) carbon pore during constant pressure Gibbs ensemble simulations at 573K. Only N_2 and H_2 are present in the measurement of selectivity, and the selectivity of nitrogen, S_{N_2} , is defined in Eq. (3.11), where x_{N_2} and y_{N_2} are the mole fractions of N_2 in the pore and bulk phase, respectively.

$$S_{N_2} = \frac{x_{N_2}/x_{H_2}}{y_{N_2}/y_{H_2}} \quad (3.11)$$

Table 3.4 Selectivity of N₂ to H₂ in a 0.83 nm wide carbon pore at a temperature of 573 K.

Pressure/bar	Selectivity, S_{N_2}
10	3.33
20	3.30
40	3.26
60	3.22
80	3.19
100	3.12
200	2.89
300	2.75

In order to compensate for the selective adsorption and maximize the yield in the pore phase, the bulk phase composition was varied in order to maintain the optimum 1:3 N:H ratio in the pore. This was accomplished by increasing the overall H₂ concentration in the simulation.

The results for these simulations in a pore width of 2.5 σ_{N_2} (0.83 nm) and at a temperature of 573 K are shown in Figure 3.11. The experimental bulk phase conversion with a 1:3 overall ratio of N:H is shown for comparison.

For high pressures the 1:3 ratio of N:H yielded the highest conversion of ammonia.

However, at lower pressures, N₂ was selectively adsorbed and resulted in a slightly lower yield of NH₃ than can be obtained by an increased concentration of H₂. The mole fractions of NH₃ in the lower pressure range are shown in Table 3.5 for N:H ratios ranging from 1:3 to 1:4. The standard deviation in the last digit of the reported NH₃ mole fraction is shown in

parenthesis. Although the maximum NH_3 conversion shifts when the overall N:H ratio changes from 3:12 to 3:9, the highest conversion was always obtained when the N:H ratio within the pore was in the stoichiometric ratio of 1:3.

Table 3.5 Ammonia mole fraction corresponding to Figure 3.11. The pore width is 0.83 nm and the temperature is 573 K. The highest conversion at each pressure is shown in bold type.

Pressure/bar	Overall N:H ratio			
	3:9	3:10	3:11	3:12
	Mole Fraction of NH_3			
20	0.452(11)	0.467(7)	0.470(11)	0.478(9)
40	0.598(8)	0.611(9)	0.612(11)	0.621(10)
60	0.678(7)	0.690(7)	0.693(8)	0.695(9)
80	0.727(6)	0.742(9)	0.741(7)	0.746(10)
100	0.768(5)	0.774(5)	0.777(5)	0.774(6)
150	0.824(5)	0.833(5)	0.831(6)	0.820(5)
200	0.859(4)	0.864(5)	0.859(5)	0.844(6)
250	0.882(4)	0.884(4)	0.871(4)	0.853(4)
300	0.896(4)	0.899(5)	0.881(4)	0.854(5)

The simulations show that the effect of selective adsorption on the ammonia synthesis reaction within a carbon pore is significant at lower pressures. Although the effect is small at higher pressures, this could be an important factor in other reacting systems.

3.4.4 Coconut Shell Carbon Model

The overall structure of the coconut shell carbon model is similar to the slit pore model. However, the coconut shell carbon preserves the surface corrugation and the pore structure seen in realistic microporous carbons. We adapt a common procedure to compare the conversion in the smooth slit-pore model to the more detailed coconut shell carbon model. The basic steps in the procedure are as follows:

- (A) Calculate the pore size distribution (PSD) of the coconut shell carbon, according to the procedure of Gelb and Gubbins [33]. The pore size distribution is represented as $P(H)$ (see Eq. (3.12) below) and the PSD is shown in Figure 3.12.
- (B) Perform Reactive Monte Carlo simulations in the slit-pore model at a specified temperature (573 K) and bulk phase pressure (100 bar), with pore widths (H) covering the range of the PSD of the realistic carbon model (H_{MIN} to H_{MAX}). Document the adsorbate density, $\mathbf{r}(H)$, and the conversion, $X_{SLIT}(H)$, measured in each slit-pore width. See Figure 3.10 for the conversion versus pore width (H).
- (C) Perform a Reactive Monte Carlo simulation in the realistic coconut shell carbon model at the same temperature (573 K) and bulk phase pressure (100 bar). Document the equilibrium conversion, $X_{COCONUT}$.
- (D) Equation (3.12) below is then used to predict the equilibrium conversion, $X_{SMOOTH(AVG)}$, from the slit-pore model approximation, by averaging the results over the PSD of the coconut shell carbon, weighting the average according to the total adsorbate density within each pore width. This can be directly compared with the simulated conversion in the coconut shell carbon, $X_{COCONUT}$, to probe the effects of the more realistic pore structure.

$$X_{SMOOTH(AVG)} = \frac{\int_{H_{MIN}}^{H_{MAX}} P(H) \cdot \mathbf{r}(H) \cdot X_{SLIT}(H) dH}{\int_{H_{MIN}}^{H_{MAX}} P(H) \cdot \mathbf{r}(H) dH} \quad (3.12)$$

This comparison procedure was performed for the ammonia synthesis reaction at a bulk phase pressure of 100 bar and a temperature of 573 K. Using the procedure just outlined, the average conversion in the smooth pores is $X_{SMOOTH(AVG)} = 0.771$, while the simulated conversion in the coconut shell carbon model is $X_{COCONUT} = 0.785$. The equilibrium conversion of the slit pore model lies within one standard deviation of the more realistic coconut shell carbon model. We would assume any discrepancy between the two calculations to arise from differences in the two pore structures.

The close agreement in conversion between the slit-pore model and the more realistic model can be attributed to the fact that there is almost no orientational disorder in the more realistic model. This causes most of the porous region to be slit-shaped. It is interesting to note that pore connectivity, corrugation and heterogeneity in the size and shape of the graphene layers and the number of graphene layers that are stacked to form the pore walls have very little influence on the equilibrium yield. Consequently, the smooth slit-pore approximation is justified as a reasonable model for adsorption in graphitic carbons and for carbons with little orientational disorder, such as graphitizable carbons heated at high treatment temperatures. In the future, it would be interesting to test the slit-pore model against other realistic models that include structural defects and curvature in the graphene sheets [17].

3.4.5 Chemically Activated Carbon Slit-Pores

In the previous two models, the carbon pore surfaces were chemically inert, with the pore surfaces composed entirely of carbon and hydrogen. However, microporous carbons often have oxygenated groups on the carbon surfaces; these can increase the selectivity and adsorption capacity of the carbon. We have modeled these chemically activated carbon pores by attaching carboxyl groups to the carbon surface at various densities, ranging from 0 sites/nm² (an unactivated pore) to 1.6 sites/nm², which are typical site densities measured in experiments. The activation sites are placed randomly on the surface, with the physical restriction that adjacent sites cannot overlap. At the highest site density studied, 1.6 sites/nm², the available volume for adsorption is reduced by roughly 8%, due to the protrusion of the carboxyl groups into the pore space. A typical configuration of these sites is shown in Figure 3.13.

We have performed simulations within these activated pores at temperatures ranging from 573-773 K and at a bulk phase pressure of 100 bar. Figure 3.14 shows the conversion to ammonia in the activated pores at these conditions and with different site densities. As seen in Figure 3.14, there is a large increase (20-80%) in conversion resulting from the surface activation. The effect of surface activation on the conversion is more pronounced at the lower temperatures, and the conversion then decreases with increasing temperature, as is seen in the unactivated pores. Over the entire temperature range, the yield of ammonia increases with an increasing amount of chemical activation. This increase in yield can be attributed to the electrostatic interaction between the ammonia molecules and the carboxyl groups.

Ammonia is strongly adsorbed to the carbon surface due to these interactions and this shifts the equilibrium towards the product ammonia molecules, as the free energy of the reacting system is minimized. We have performed simulations in narrower activated slit-pores, and similar results are obtained. Figure 3.15 shows the conversion of ammonia in a 1.0 nm activated pore, with site densities similar to the 1.6 nm pore shown in Figure 3.14 and at the same pressure of 100 bar.

The strong affinity of ammonia for the carboxyl sites is clearly illustrated in Figure 3.16, which is a simulation snapshot taken during a RxMC simulation in the activated carbon pore. For visual clarity, the top half of the pore is removed, and only ammonia molecules and carboxyl surface groups are shown. It is readily apparent in Figure 3.16 that the ammonia molecules tend to migrate towards the areas of high carboxyl site density, which is due to the favorable electrostatic interactions. Although not shown, the nitrogen and hydrogen molecules, which are also present in the pore, show very little preference for adsorption near the carboxyl groups.

While the results in the two pore sizes are similar, there are several differences that are evident. The conversion in the unactivated 1.00 nm pore is higher than in the 1.60 nm unactivated pore at 573 K, which is consistent with the trends seen in Figure 3.9. It is interesting to note that over the entire temperature range, the 1.00 nm pore maintains a distinct yield enhancement over the 1.60 nm pore, given the same amount of surface

activation. This seems to indicate that surface activation and pore width are two parameters that can be independently tuned to maximize the yield of this reaction.

3.4.6 Single-Walled Carbon Nanotubes

The last carbon model studied is the carbon nanotube model. The pore diameter of the tubes is varied, and the conversion is measured. Since these nanotubes are not isolated but rather are arranged in a hexagonal bundle, a second variable is also present in the model, the nanotube-nanotube separation distance. We have measured the conversion of ammonia synthesis at several different nanotube separation distances, ranging from 0.34 nm to 0.613 nm, where this separation distance is defined as the closest distance between any two carbon centers on neighboring tubes. For the ammonia synthesis reaction, the conversion in the nanotube arrays is found to be relatively insensitive to the nanotube separation distance, for the range of separations covered. This insensitivity to nanotube separation is due to the fact that the interstitial space between the nanotubes is generally too small for ammonia molecules to form. Therefore, we have chosen to focus on the effect of the individual nanotube diameters on the yield of ammonia, leaving the separation distance fixed. In all of the carbon nanotube simulations, we have fixed the nanotube-nanotube separation distance at a value of 0.34 nm, which corresponds to the LJ diameter of a carbon atom. With a separation distance of 0.34 nm, the majority of the adsorbate molecules are located within the inside of the nanotubes, due to the negligible space available for interstitial adsorption.

Using RxMC, the conversion of ammonia has been simulated in three different bundles with discrete nanotube diameters of 1.087 nm, 1.223 nm, and 1.359 nm, which correspond to (8,8), (9,9), and (10,10) nanotubes, respectively. The nanotube separation distance was 0.34 nm. The mole fraction of ammonia within each of these nanotube arrays is shown in Figure 3.17 at a bulk phase pressure of 100 bar and temperatures ranging from 573-773 K.

In Figure 3.17, the conversion of ammonia within slit-shaped pores is shown along with the conversion in the carbon nanotube arrays, in order to elucidate the effect of the different pore structures. While the pore diameters and the slit-pore widths in Figure 3.17 are comparable in dimension, the conversion within the nanotubes is noticeably higher than in the slit-pores. Although the smallest nanotube diameter shown is 1.087 nm, corresponding to an (8,8) nanotube, a (7,7) nanotube was also tested which had a diameter of 0.955 nm. However, there was very little increase in the conversion of ammonia as compared to the (8,8) nanotube. Although, the cylindrical geometry of the carbon nanotubes seems to favor the formation of ammonia, there is the same decrease in conversion with increasing temperature that is seen in the slit-pores, regardless of the nanotube diameter. We have also performed the comparison between slit-pores and the carbon nanotubes at higher pressures (200-500 bar, results not shown), and the enhancement is similar to the results shown in Figure 3.17.

3.5 Conclusions

The simulation results presented here demonstrate that the structural and chemical details of catalysts and catalyst supports can cause significant changes in the yield of chemical

reactions. This effect is seen with the ammonia synthesis system studied in this work [10], as well as with the nitric oxide dimerization reaction presented in Chapter 2 [8].

The current ammonia synthesis simulations within the four different microporous carbon models lead us to several conclusions. First, regardless of the pore geometry (slits or cylinders), the conversion of ammonia is enhanced within narrower pores. This conclusion is limited by geometric constraints when the accessible pore space becomes too small to allow the formation of ammonia molecules (widths below ~ 0.65 nm). Second, the comparison between the slit-pore and the more realistic coconut shell carbon suggest that the pore surface corrugation and pore connectivity are relatively unimportant in determining the yield of ammonia for such graphitic carbon. This result should be taken in conjunction with the relatively high simulation temperatures, as lower reaction temperatures could possibly magnify the effects of the geometric pore details. Lastly, the chemical nature of the pore surface was found to have a dramatic effect on the equilibrium yield of ammonia, regardless of the pore width in the slit-pore model.

Although all carbon pore types and sizes in this study have demonstrated an increased yield for the ammonia synthesis reaction, the yield was typically less than optimum due to selective adsorption of nitrogen over hydrogen within these microporous carbons. The maximum yield of ammonia synthesis is always obtained from a stoichiometric 3:1 mixture of $H_2:N_2$, whether the reaction is occurring in the bulk phase or in the pore phase. We have found that the stoichiometric imbalance within the pore, due to selective adsorption, can

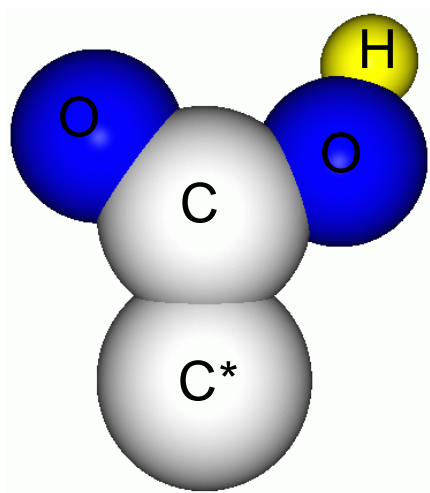
cause up to a 5% decrease in the conversion of ammonia. The conversion within the pore can be maximized by adjusting the overall system composition, *i.e.*, by increasing the relative concentration of H₂ to N₂ above 3:1.

The impact of these results should not be limited to the ammonia synthesis reaction or to carbon pores. Rather, these simulations should motivate work aimed to tailor the geometric and energetic details of microporous catalysts and support materials in an effort to create optimum nanoreactor environments for chemical synthesis.

References

- [1] L. Forni, D. Molinari, I. Rossetti, and N. Pernicone, *Applied Catalysis A: General* 185 (1999), 269.
- [2] C. J. H. Jacobsen, S. Dahl, P. Hansen, E. Törnqvist, L. Jensen, H. Topsøe, D. V. M. Prip, and I. Chorkendorff, *Journal of Molecular Catalysis A: Chemical* 163 (2000), 19.
- [3] Z. Kowalczyk, S. Jodzis, and J. Sentek, *Applied Catalysis A: General* 138 (1996), 83.
- [4] Z. Kowalczyk, S. Jodzis, W. Raróg, J. Zielinski, J. Pielaszek, and A. Presz, *Applied Catalysis A: General* 184 (1999), 95.
- [5] H.-B. Chen, J.-D. Lin, Y. Cai, X.-Y. Wang, J. Yi, J. Wang, G. Wei, Y.-Z. Lin, and D.-W. Liao, *Applied Surface Science* 180 (2001), 328.
- [6] C. Liang, Z. Wei, Q. Xin, and C. Li, *Applied Catalysis A: General* 208 (2001), 193.
- [7] J. K. Johnson, A. Z. Panagiotopoulos, and K. E. Gubbins, *Molecular Physics* 81 (1994), 717.
- [8] C. H. Turner, J. K. Johnson, and K. E. Gubbins, *Journal of Chemical Physics* 114 (2001), 1851.
- [9] M. Borówko and R. Zagórski, *Journal of Chemical Physics* 114 (2001), 5397.
- [10] C. H. Turner, J. Pikunic, and K. E. Gubbins, *Molecular Physics* 99 (2001), 1991.
- [11] W. Gu, M. Warrier, V. Ramamurthy, and R. G. Weiss, *Journal of the American Chemical Society* 121 (1999), 9467.
- [12] Johnson, J. K., *Advances in Chemical Physics*, edited by Ferguson, D. M., Siepmann, I., and Truhlar, D. G., Wiley: New York 105 (1999), 461.
- [13] W. R. Smith and B. Triska, *Journal of Chemical Physics* 100 (1994), 3019.
- [14] M. Lisal, W. R. Smith, and I. Nezbeda, *Journal of Chemical Physics* 113 (2000), 4885.
- [15] A. Z. Panagiotopoulos, *Molecular Physics* 62 (1987), 701.
- [16] S. C. McGrother and K. E. Gubbins, *Molecular Physics* 97 (1999), 955.
- [17] J. Pikunic, R. J. M. Pellenq, K. T. Thomson, J.-N. Rouzaud, P. Levitz, and K. E. Gubbins, *Studies in Surface Science and Catalysis* 132 (2001), 647.
- [18] R. L. McGreevy and L. Pusztai, *Molecular Simulation* 1 (1988), 359.

- [19] Appl, M., Ammonia, Wiley: New York, (1999).
- [20] A. Cheng and W. A. Steele, Journal of Chemical Physics 92 (1990), 3858.
- [21] A. V. Vernov and W. A. Steele, Langmuir 2 (1986), 219.
- [22] Hirschfelder, J. O., Curtiss, C. F., and Bird, R. B., Molecular Theory of Gases and Liquids, Wiley: New York, (1954).
- [23] Steele, W. A., Interaction of Gases with Solid Surfaces, Pergamon: Oxford, (1974).
- [24] E. A. Müller, F. R. Hung, and K. E. Gubbins, Langmuir 16 (2000), 5418.
- [25] A. V. Shevade, S. Jiang, and K. E. Gubbins, Journal of Chemical Physics 113 (2000), 6933.
- [26] Kaneko, K., personal communication, (2000).
- [27] P. M. Ajayan and T. W. Ebbesen, Reports on Progress in Physics 60 (1997), 1025.
- [28] L. J. Gillespie and J. A. Beattie, Physical Review 36 (1930), 743.
- [29] McQuarrie, D. A., Statistical Mechanics, HarperCollins: New York, (1976).
- [30] Perry, R. H. and Green, D. W., Perry's Chemical Engineers' Handbook, McGraw-Hill: New York, (1984).
- [31] K. Kaneko, R. F. Cracknell, and D. Nicholson, Langmuir 10 (1994), 4606.
- [32] F. Darkrim, J. Vermesse, P. Malbrunot, and D. Levesque, Journal of Chemical Physics 110 (1999), 4020.
- [33] L. D. Gelb and K. E. Gubbins, Langmuir 15 (1999), 305.



<u>bond length/nm</u>	<u>angle</u>
C*-C: 0.1520	C*-C=O: 126°
C=O: 0.1214	C*-C-O: 111°
C-O: 0.1364	C-O-H: 107°
O-H: 0.0970	

Figure 3.1 Structure of the -COOH activation site used in simulation.

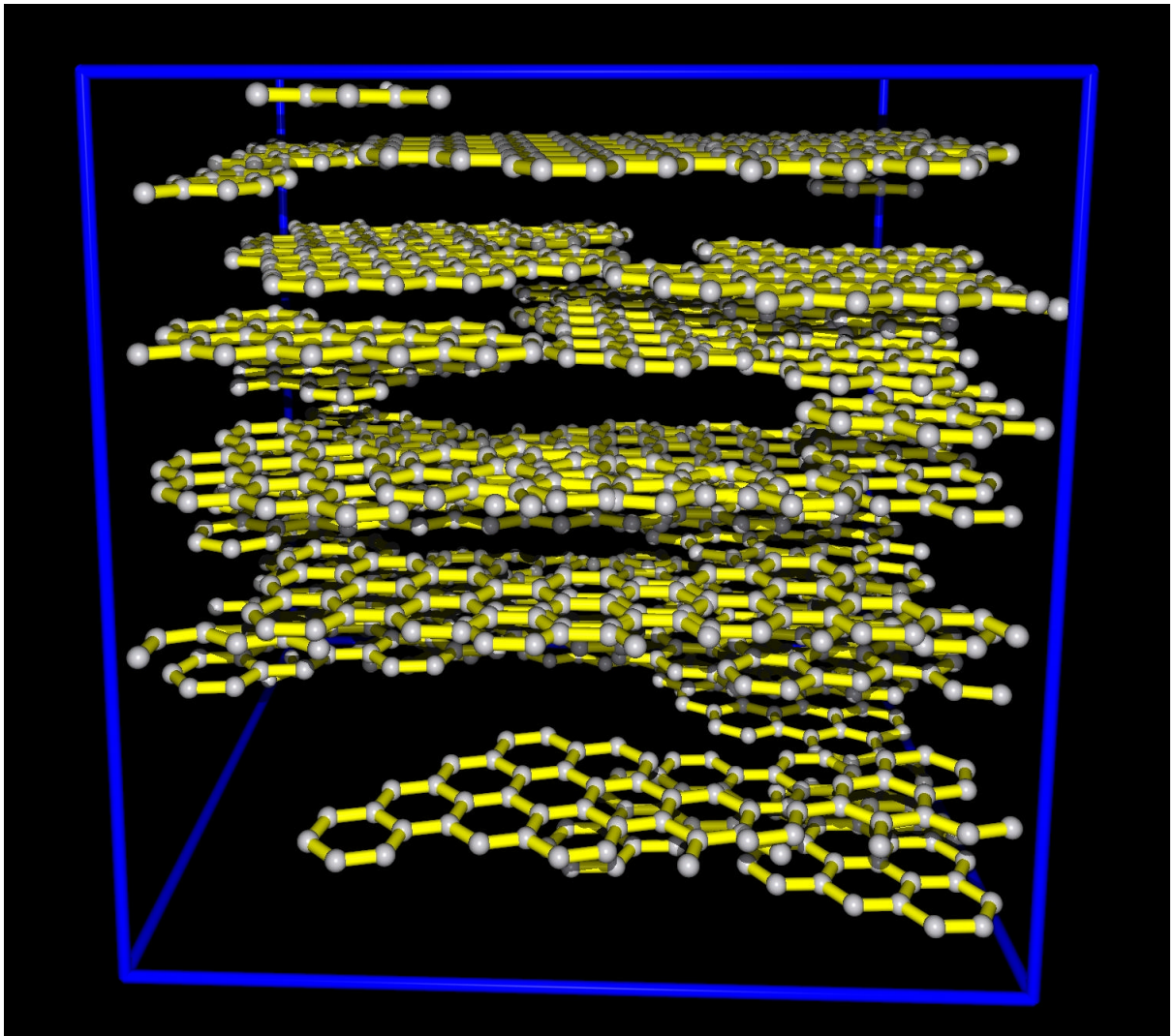


Figure 3.2 Coconut shell carbon model reconstructed from experimental structure factor data.

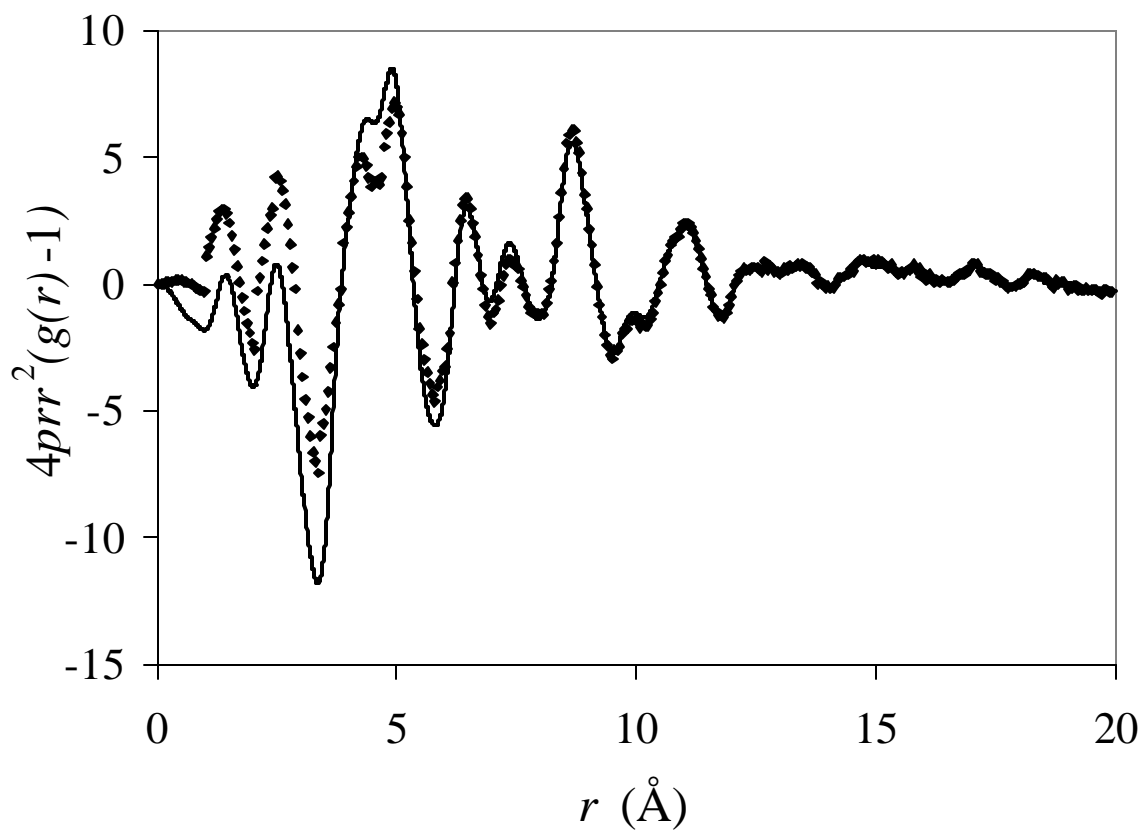


Figure 3.3 Radial distribution function of activated carbon from coconut shell. Experimental (line) and RMC model (diamonds).

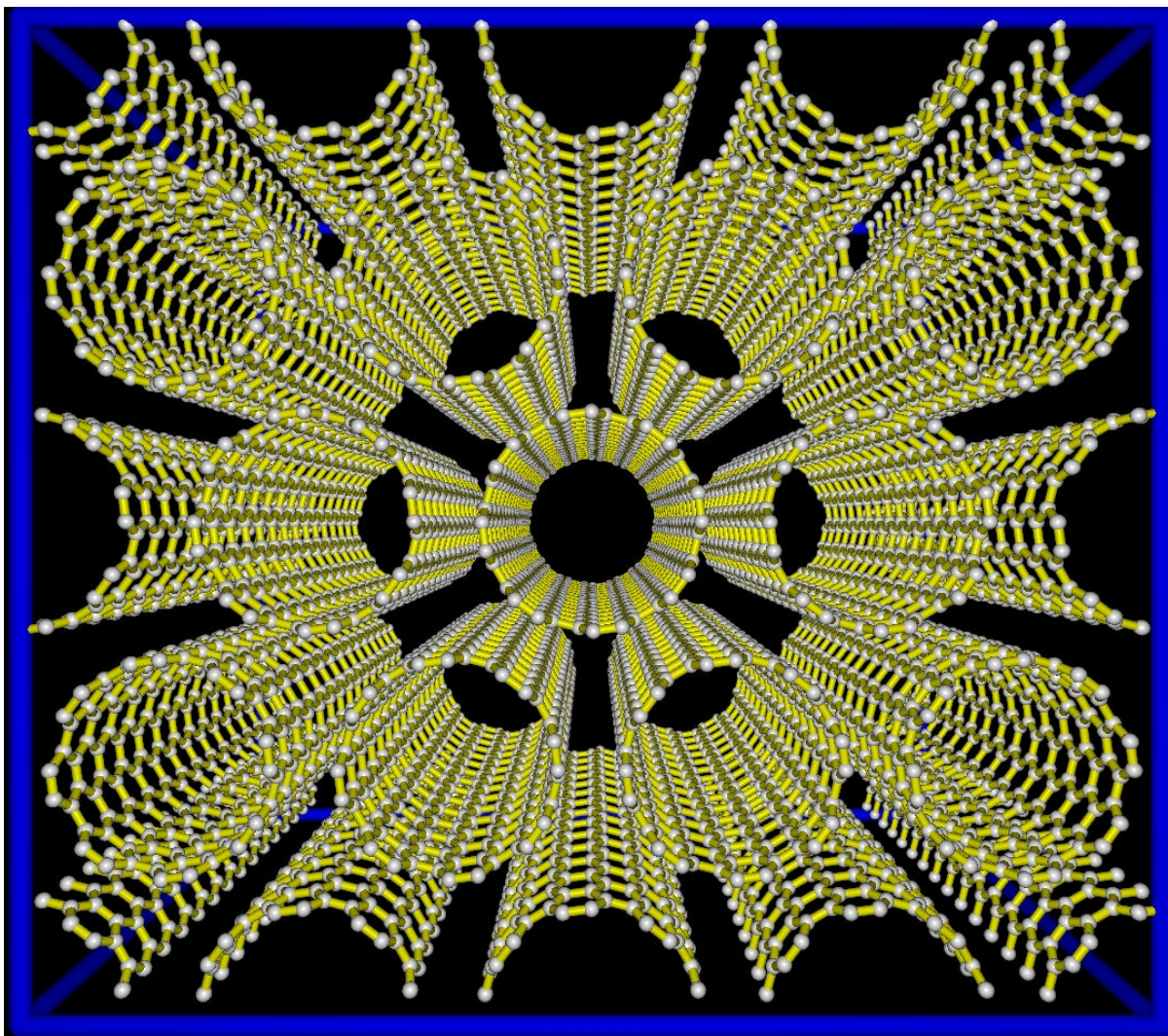


Figure 3.4 Hexagonal packing of the carbon nanotubes used in simulations. These are (10,10) nanotubes, corresponding to a diameter of 1.36 nm.

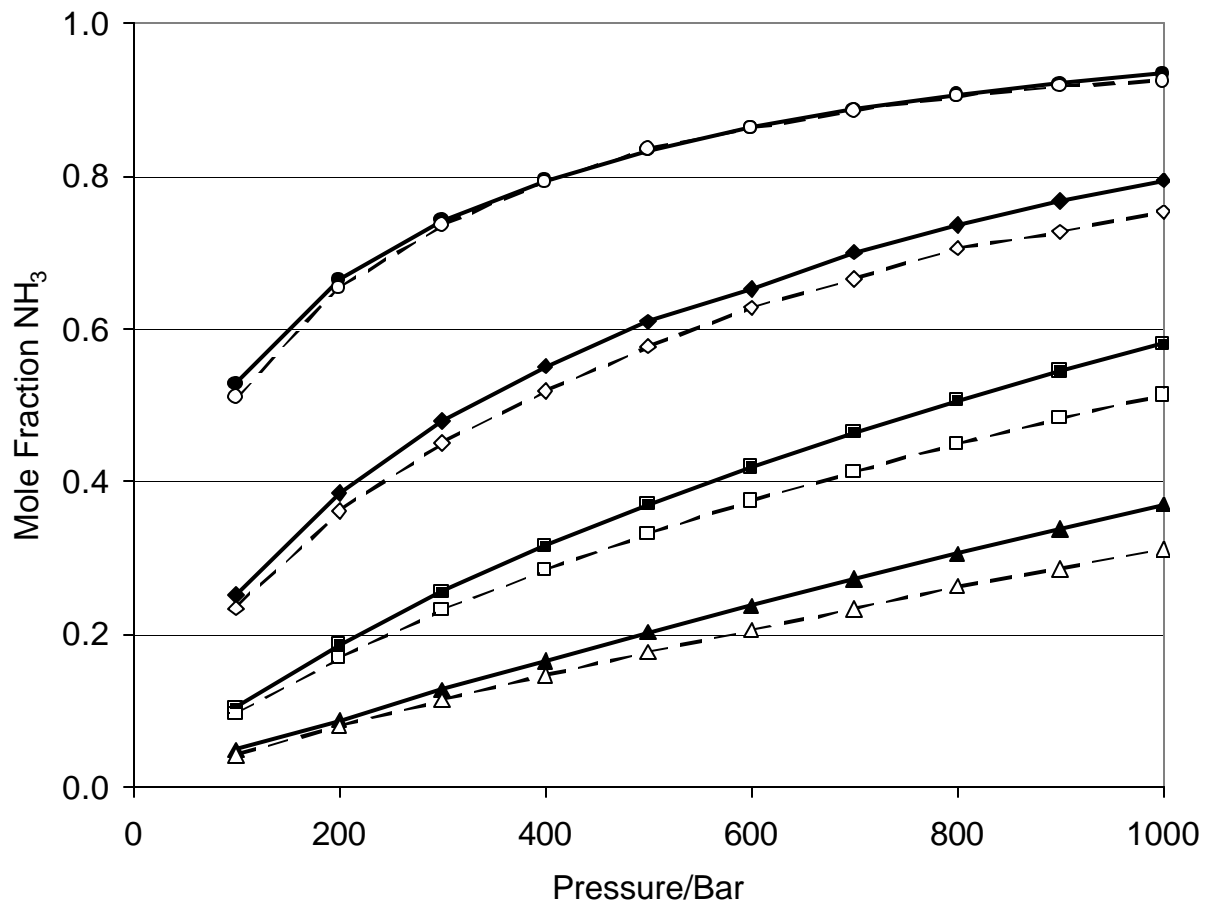


Figure 3.5 Mole fraction of NH₃ for the bulk phase reaction, with the ratio of N₂ to H₂ set at 1:3. The solid points and solid lines represent fits to experimental data [28], while the open points and dashed lines correspond to simulations from this work. Key: circles: 573 K, diamonds: 673 K, squares: 773 K, triangles: 873 K.

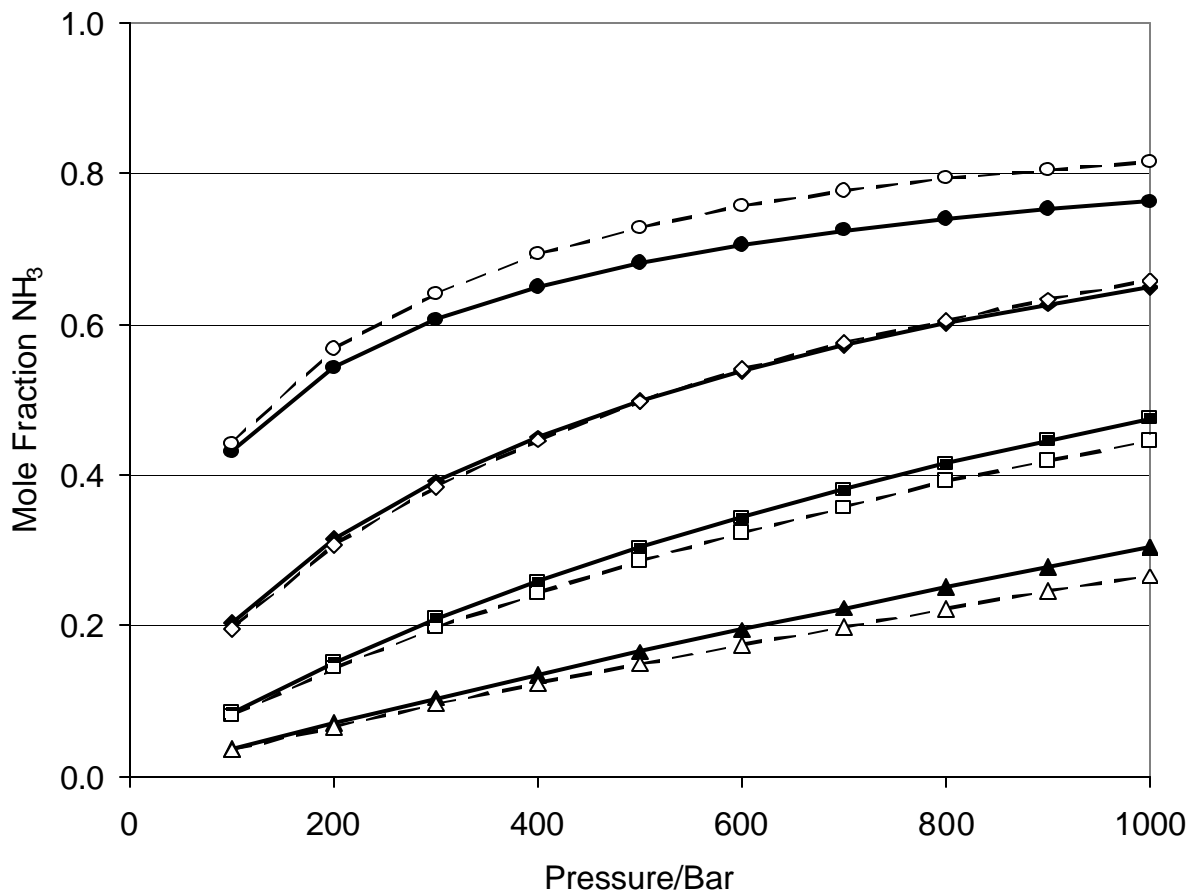


Figure 3.6 Mole fraction of NH_3 for the bulk phase reaction starting from a 1:3 ratio of N_2 to H_2 , in the presence of inert gases (2.5 mole % Ar; 7.5 mole % CH_4). The solid points and solid lines represent fits to experimental data [28], while the open points and dashed lines correspond to simulations from this work. Key: circles: 573 K, diamonds: 673 K, squares: 773 K, triangles: 873 K.

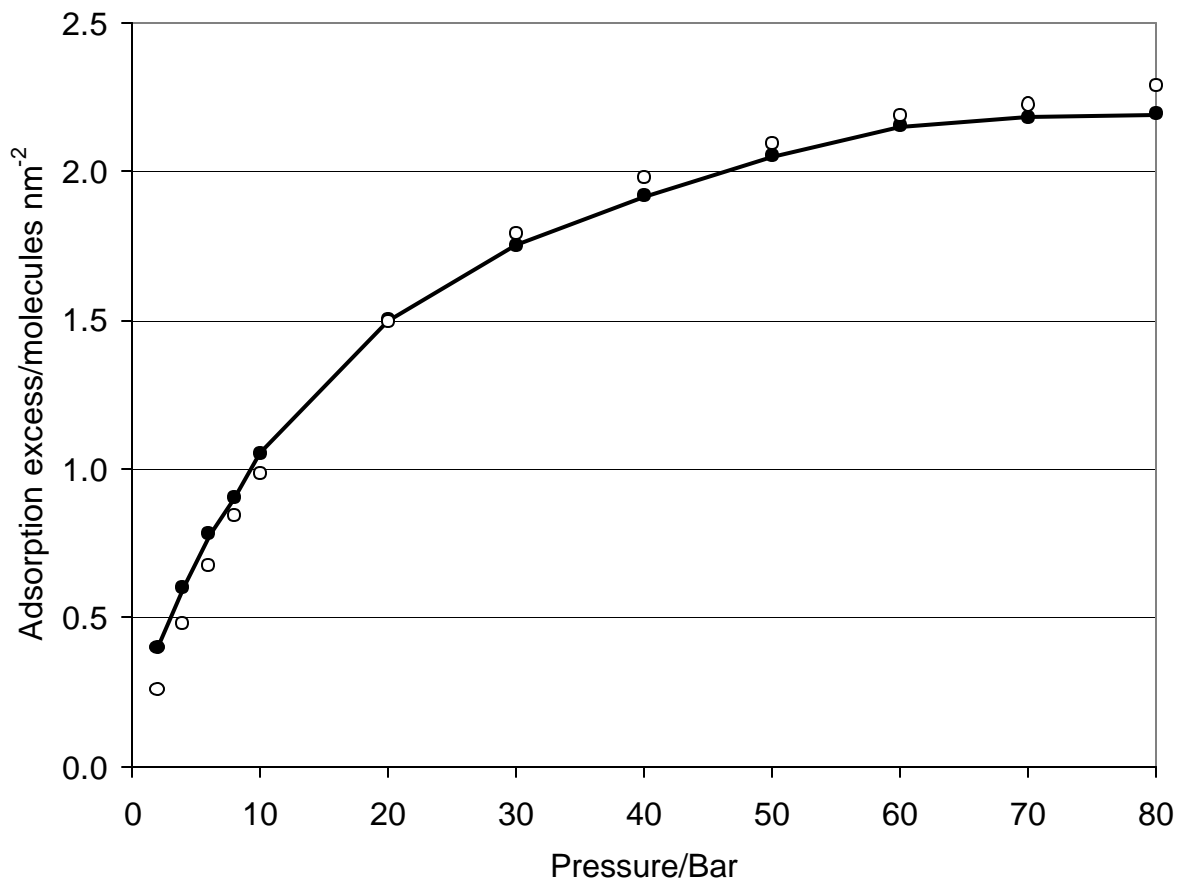


Figure 3.7 N₂ adsorption isotherm in a pore of width $H/s_{N_2}=2.98$ (0.99 nm) at a temperature of 303 K. The solid line and solid points correspond to the experimental adsorption measurements of N₂ in activated carbon fibers [31]. The open circles correspond to the constant pressure Gibbs ensemble MC simulations from this work.

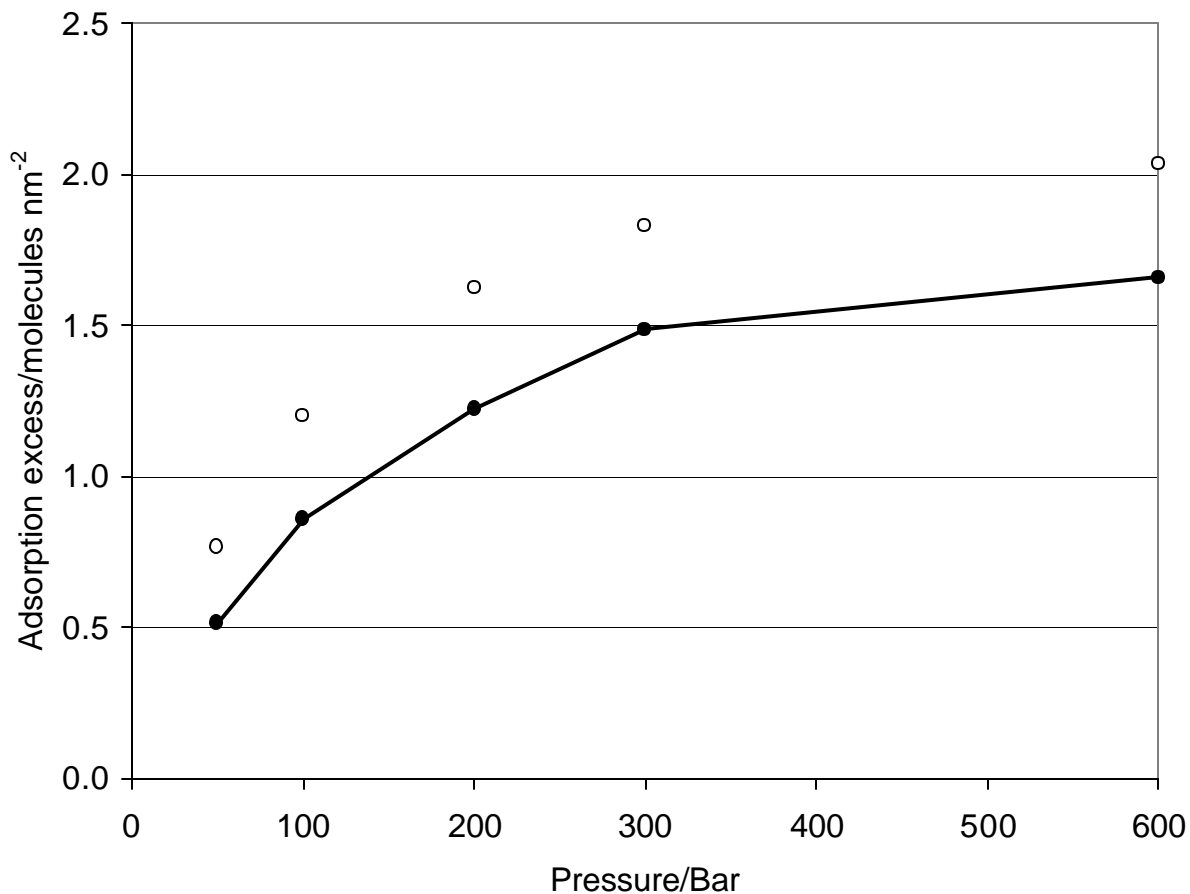


Figure 3.8 H₂ adsorption isotherm in a pore of width $H/s_{H_2} = 2.53$ (0.737 nm) at a temperature of 293 K. The solid line and filled circles correspond to the experimental adsorption measurements of H₂ in AX21 activated carbon fiber [32]. The open circles correspond to the constant pressure Gibbs ensemble MC simulations from this work.

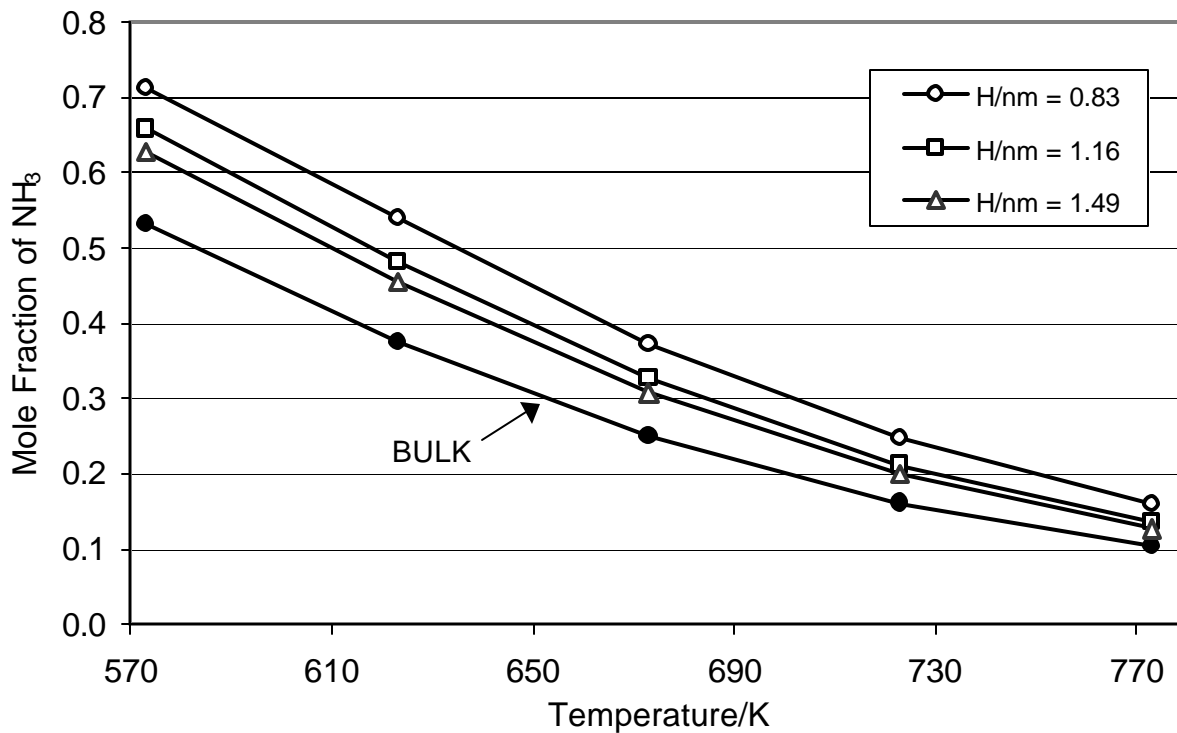


Figure 3.9 Simulations of ammonia synthesis in carbon slit-shaped pores of various widths, corresponding to a bulk phase pressure of 100 bar. The corresponding mole fraction of NH_3 in the bulk phase is shown for comparison.

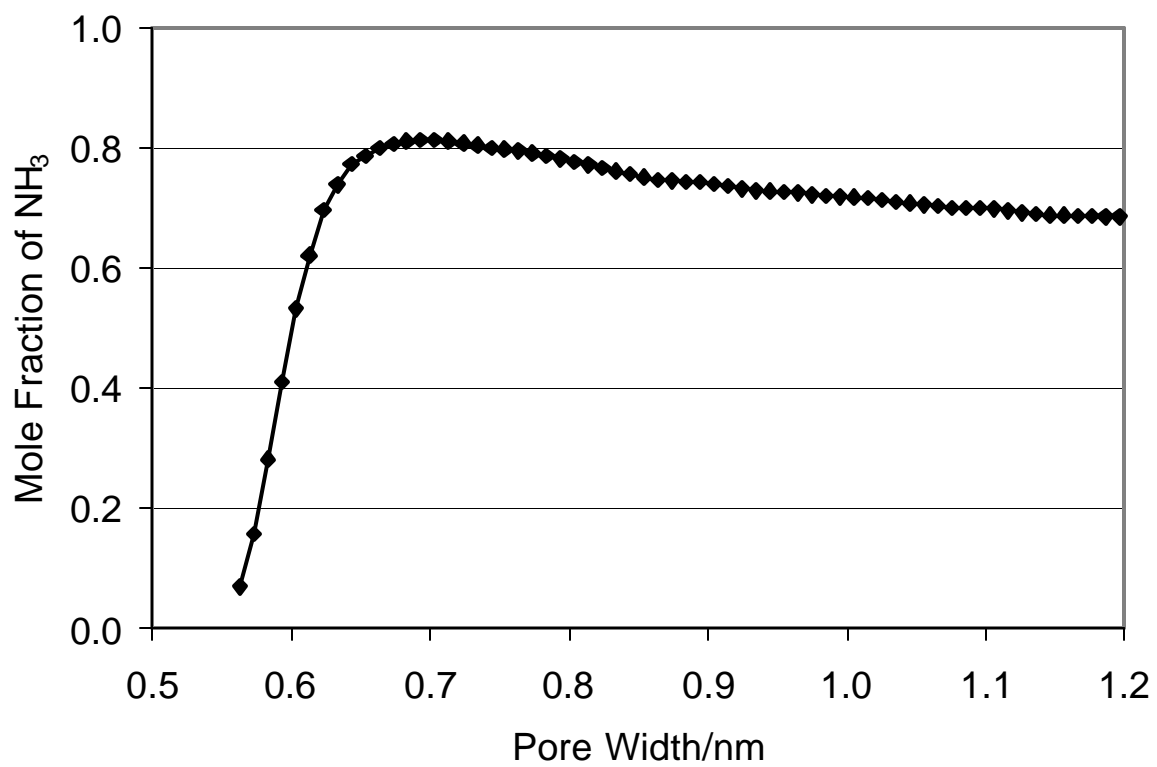


Figure 3.10 Conversion of the ammonia synthesis reaction at a temperature of 573 K and a pressure of 100 bar, in a smooth slit-shaped pore modeled with the 10-4-3 Steele potential [23].

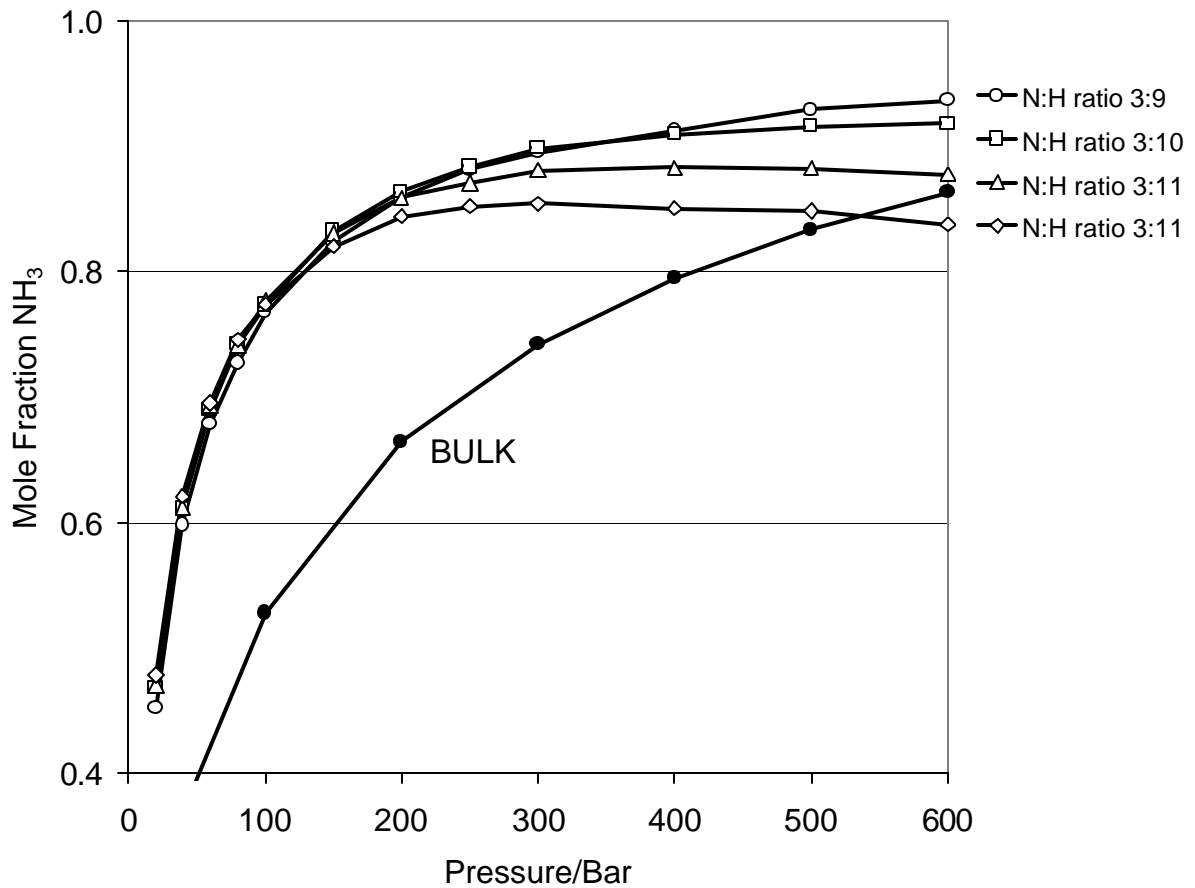


Figure 3.11 Ammonia synthesis at a temperature of 573 K in a pore width of $2.5s_{N_2}$ (0.83 nm). The graph shows the effect of different overall N:H ratios (bulk + pore) on the conversion within the pore phase. The experimental mole fraction of NH₃ from a bulk phase mixture with an overall 1:3 N:H ratio is shown for comparison.

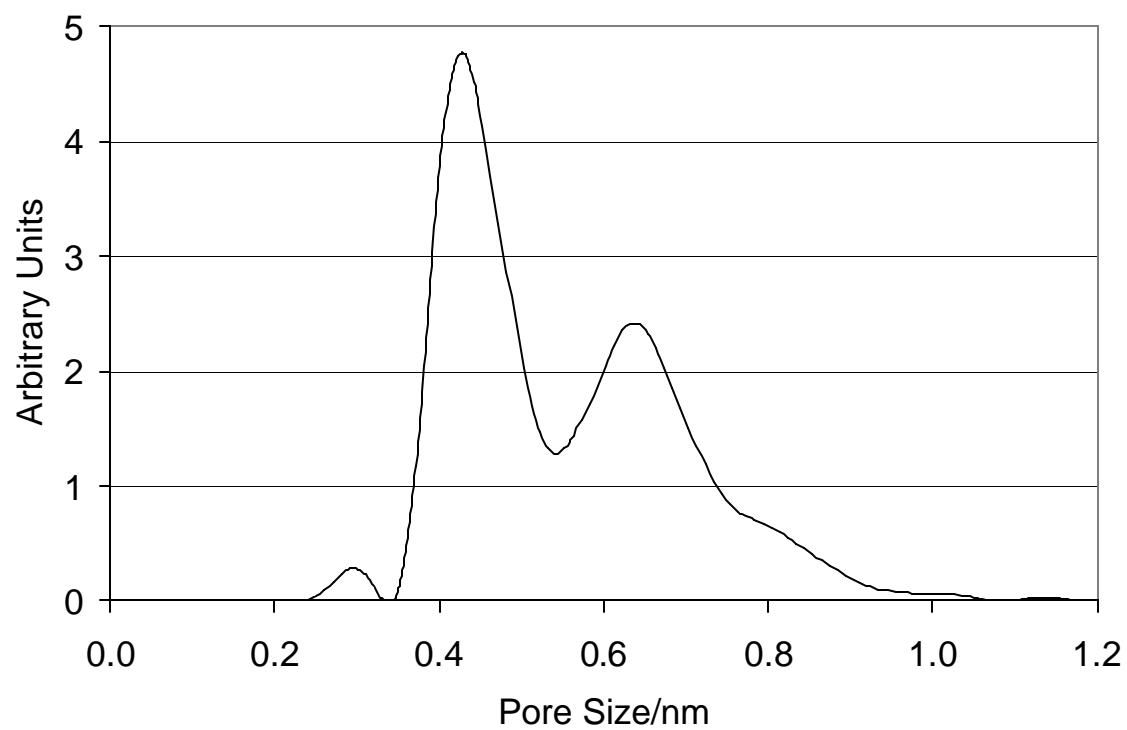


Figure 3.12 Pore size distribution (PSD) of the coconut shell microporous carbon model.

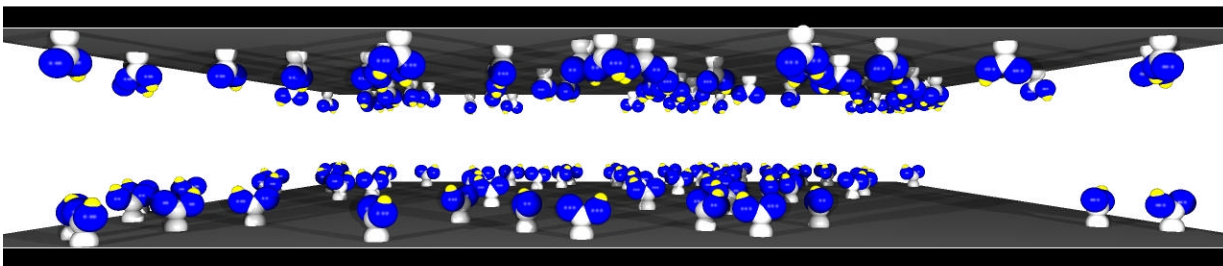


Figure 3.13 A slit-shaped pore, chemically activated by -COOH groups. The site density is 0.544 sites/nm^2 and the pore width is 1.60 nm .

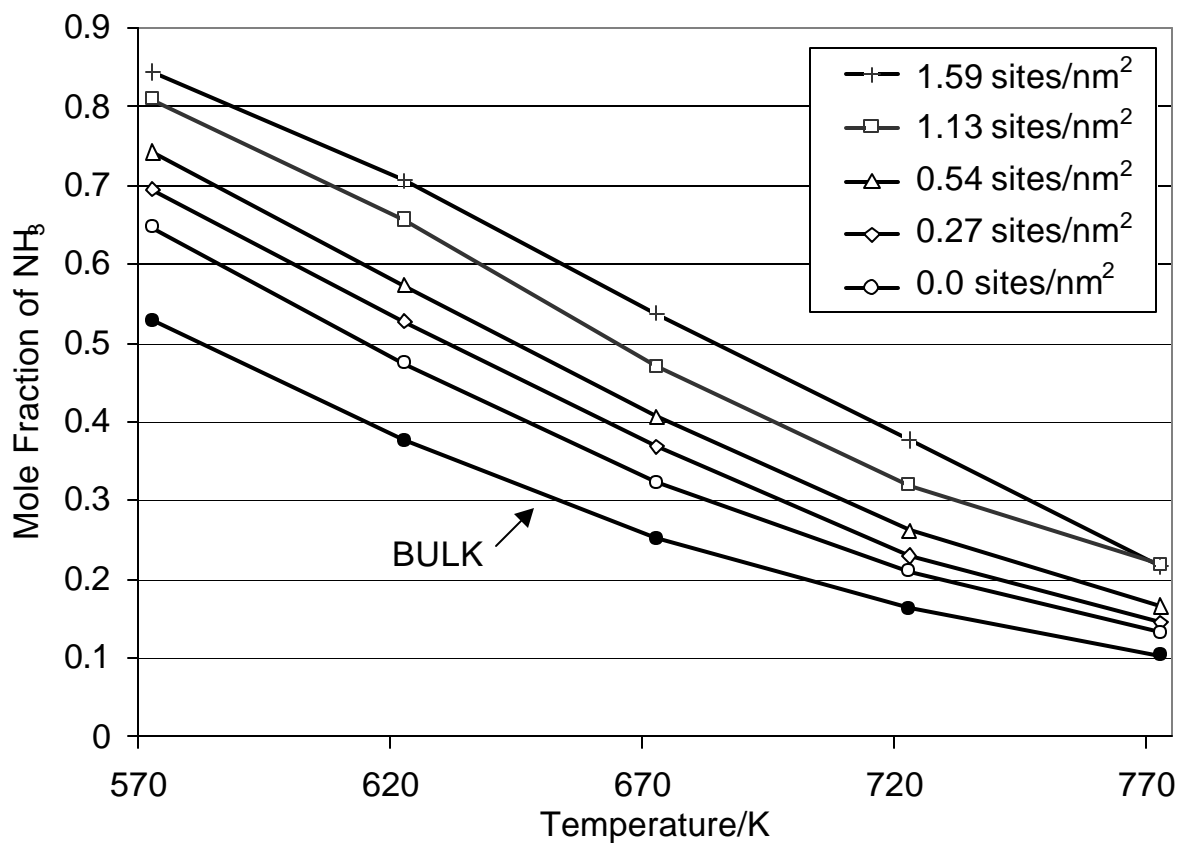


Figure 3.14 Conversion to ammonia in chemically activated slit-pores, with varying -COOH site densities. The bulk phase pressure is 100 bar, and the pore width is 1.60 nm. The conversion in the equilibrium bulk phase is shown for comparison.

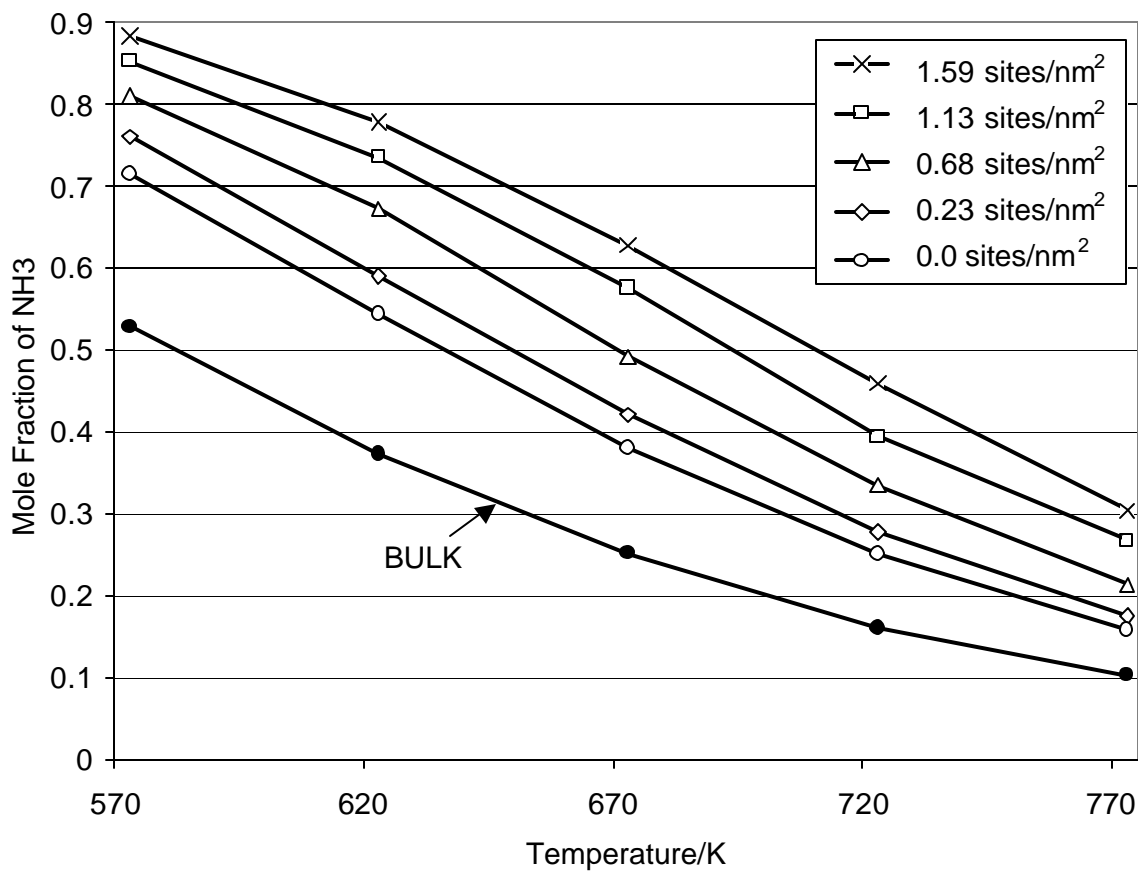


Figure 3.15 Conversion to ammonia in chemically activated slit-pores, with varying -COOH site densities. The bulk phase pressure is 100 bar, and the pore width is 1.00 nm. The conversion in the equilibrium bulk phase is shown for comparison.

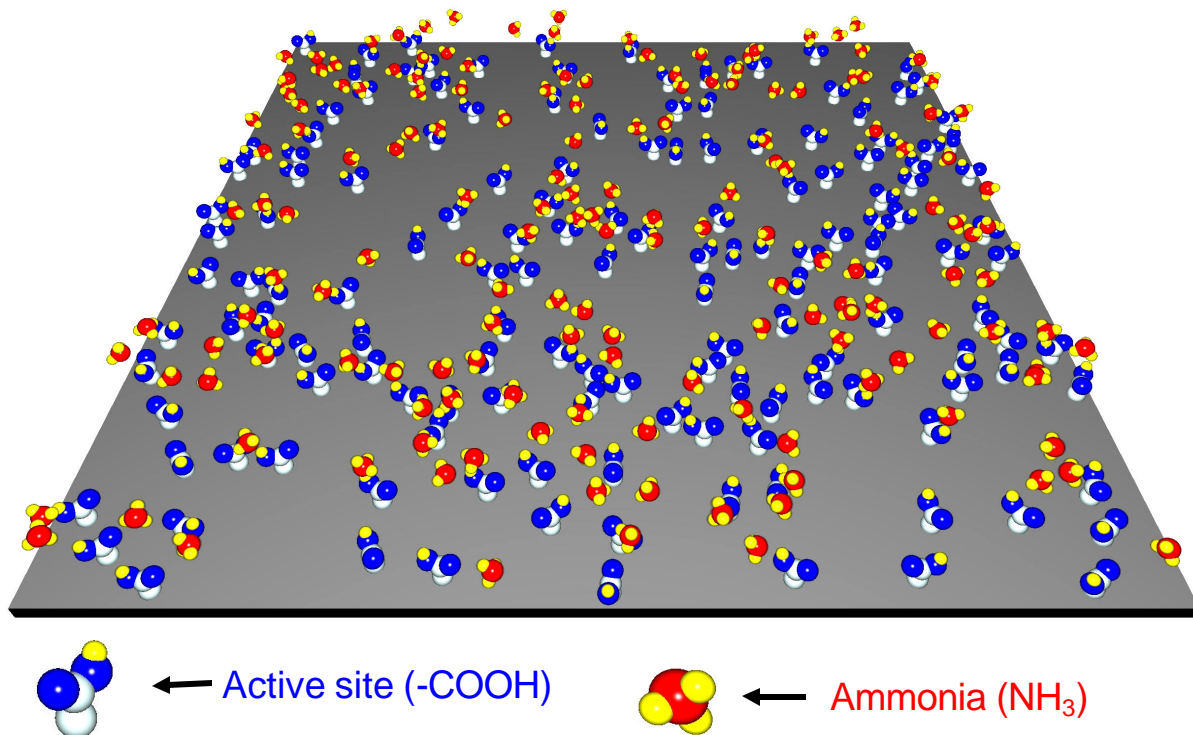


Figure 3.16 The ammonia synthesis reaction in an activated carbon pore. For clarity, the top half of the pore is removed and only the ammonia molecules are shown. The pore width is $H=1.60$ nm, the temperature is 573 K, the bulk phase pressure is 100 bar, and the carboxyl site density is 1.59 sites/nm².

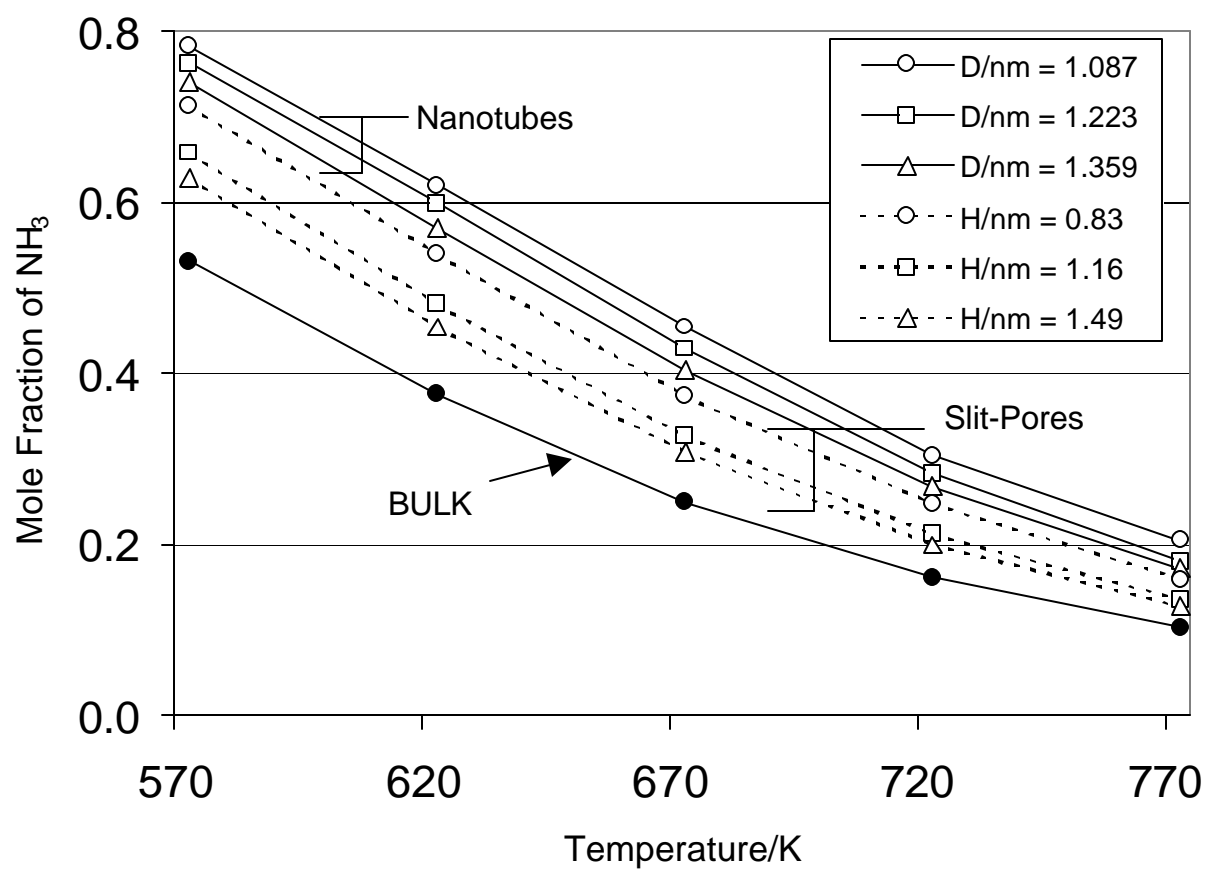


Figure 3.17 RxMC simulations of ammonia synthesis in carbon nanotube bundles, corresponding to a bulk phase pressure of 100 bar. The conversion of ammonia within various slit pores is shown for comparison. The corresponding tube diameters (D) and slit-pore widths (H) are shown in the figure.

CHAPTER 4

Esterification of Acetic Acid

4.1 Introduction

Ethyl acetate is an important industrial solvent, which is typically produced from ethanol and acetic acid in the liquid phase, using a homogeneous catalyst such as hydrochloric acid or sulfuric acid [1].



This reaction, Eq. (4.1), is an equilibrium-limited reaction with a final conversion of about 66-67% in the liquid phase [2-5], depending on the starting ratio of the reactants. The conversion will tend to increase or decrease by a few percent, if the 1:1 stoichiometric ratio of acetic acid to ethanol increases or decreases, respectively. Additionally, there have been several thermodynamic models developed in order to describe the equilibrium [5-8] and kinetics [9-15] of this reaction. Although the esterification reaction is typically conducted in the liquid phase in industry, it is well-known [16] that higher conversions are found when the reaction is conducted in the gas phase. This fact has motivated several experimental studies, as well as our simulation work, to transfer this reaction from the liquid phase to other alternative reaction environments in an effort to increase the equilibrium yield.

In this Chapter, we explore alternative reaction environments, which show potentially higher conversions of ethyl acetate than the liquid phase reaction allows. The two reaction systems that we focus on are ethyl acetate production in a carbon dioxide solvent and within microporous carbons. There is existing experimental evidence [17-22] that the equilibrium conversion of ethyl acetate can be moderately enhanced in both of these alternative environments, as compared to the same reaction in the liquid phase. We would like to confirm these findings, as well as explain the source of the enhanced yield.

Using supercritical fluids, such as supercritical carbon dioxide (scCO₂), as a reaction media has gained considerable attention in recent years, due to the environmental benefits and to the favorable processing conditions. These benefits are due in part to the increased diffusivity, lowered viscosity, and enhanced mass and heat transfer, as compared to traditional organic solvents [23]. However, chemical reactions are expected to behave differently in supercritical fluids than in the gas phase or in traditional liquid phase solvents [24]. If we are able to understand and accurately model this behavior, then we may be able to increase reaction rates, enhance selectivity, and allow more efficient separation processes [25].

A specific effect of using a supercritical solvent, the local density enhancement of the fluid, is expected to influence chemical reactions [26]. In supercritical fluids, the average solvent density in the region around a solute molecule will typically be different from the bulk phase density, and this deviation is often on the order of 50 to 300%. This density enhancement, as well as selective partitioning between solute clusters and the surrounding solvent, can

potentially influence the kinetics as well as the yield of chemical reactions. While we are interested in exploiting this density enhancement to improve chemical reaction yields, the influence of solvent inhomogeneities and cluster effects on chemical reactions is presently not well understood. In order to explain the role of a supercritical solvent on reactions, we have dedicated a large portion of this Chapter to modeling the chemical reaction yield of ethyl acetate in scCO_2 .

In order to evaluate another potentially viable environment for producing higher yields of ethyl acetate, we have studied the conversion of this same reaction, Eq. (4.1), in slit-shaped carbon pores, which is an approximate model for activated carbons. This vapor-phase process, using an activated carbon support, presents an alternative to the traditional liquid-phase process, which could potentially reduce energy costs, minimize unnecessary waste, and reduce reactor corrosion. Microporous carbons have been identified in experiments [21,22] for their unique ability to entrap heteropoly acids (HPAs), which are active catalysts for the esterification of acetic acid. HPAs are highly soluble in polar media, and entrapping these catalysts within a support material, such as activated carbon, is necessary for avoiding difficult separation processes. Additionally, industry has found that esterification is an efficient method for regenerating activated carbon from waste water purification units that have become saturated with acetic acid [19,20]. It has been shown [20] that approximately 90% of the acetic acid in the saturated carbon can be converted to ethyl acetate and recovered.

There are several other alternatives as well for the vapor-phase production of ethyl acetate, but these alternatives will not be considered here. For example, both ion-exchange resins [14] and HPAs entrapped in Y-type zeolites [27] have been used for the esterification of acetic acid. However, HPAs immobilized on activated carbon have shown [22] to be much higher in activity, stability, and selectivity for esterification than zeolites or ion exchange resins currently used in industry. Furthermore, although zeolite catalysts have a high activity, reactions tend to give a variety of undesired by-products due to the higher reaction temperatures used [22], and commonly result in the dehydration of the alcohol or isomerization. However, side reactions are not always seen in zeolites at high temperature. For instance, Santacesaria *et al.* [15] have performed the esterification reaction in decaionized Y zeolites at 423K, and see no traces of the ethyl ether as a byproduct under steady-state conditions. Also, calcined niobic acid has been shown to be an efficient catalyst for vapor-phase esterification [28]. In this study [28], the conversion tends to increase with temperature, which is the opposite of what the equilibrium constant would naturally predict.

In consideration of these previous experimental studies, the goal of this Chapter is to understand the effect of CO₂ and microporous carbons on the production of ethyl acetate, and is organized according to the following outline. In Sections 4.2 and 4.3, we describe our simulation methods and molecular models used to predict the conversion of this reaction. Then in Section 4.4, we present our simulations results of ethyl acetate conversion in the bulk gas phase, in supercritical carbon dioxide, and in two different microporous carbon models. Finally, in Section 4.5 we present the conclusions of our simulation studies.

4.2 Simulation Methods

4.2.1 Reactive Monte Carlo

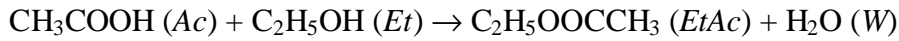
In this study, we use Reactive Monte Carlo (RxMC) simulations [29,30] to predict the yield of acetic acid esterification in the bulk gas phase, adsorbed within carbon slit-pores, and dissolved in supercritical carbon dioxide (scCO₂). This simulation method is essentially the same as the reaction ensemble method developed independently by Smith and Triska [31,32]. Using this flexible Monte Carlo technique, the equilibrium yield can be predicted for reactions that involve a change in the number of moles, multiple simultaneous reaction equilibria, or multi-phase reacting systems [31-38]. Furthermore, the equilibrium conversion can be simulated without specifying the individual chemical potentials or chemical potential differences of the reacting molecules. The only information necessary for predicting reaction equilibria using this technique are the molecular partition functions (q_i) for each of the reacting species, the bond energies for the bonds that are broken or formed, and accurate intermolecular potentials for calculating the configurational energy of the system. The constant pressure version of RxMC is designed to minimize the Gibbs energy of the reacting system, and thus determine the true equilibrium condition, regardless of any rate limitations.

The constant pressure version of RxMC, applied to the esterification of acetic acid, involves the following Monte Carlo trial moves, with the molecular moves, the forward and reverse reaction steps, and volume changes being accepted with the designated probability (P_{acc}):

- (A) **Move/Rotation:** a change in the position, orientation, or dihedral angle of a molecule chosen at random:

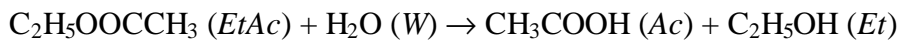
$$P_{acc} = \min [1, \exp(-\mathbf{b}dU)] \quad (4.2)$$

- (B) **Forward Reaction Step:** reactant molecules are chosen at random and changed to product molecules:



$$P_{acc} = \min \left[1, \exp(-\mathbf{b}dU_F) \times \frac{q_{EtAc} q_W}{q_{Ac} q_{Et}} \times \frac{(N_{Et})(N_{Ac})}{(N_{EtAc} + 1)(N_W + 1)} \right] \quad (4.3)$$

- (C) **Reverse Reaction Step:** product molecules are chosen at random and changed to reactant molecules:



$$P_{acc} = \min \left[1, \exp(-\mathbf{b}dU_R) \times \frac{q_{Ac} q_{Et}}{q_{EtAc} q_W} \times \frac{(N_{EtAc})(N_W)}{(N_{Ac} + 1)(N_{Et} + 1)} \right] \quad (4.4)$$

- (D) **Volume Change:** a random change in the system volume in order to maintain a constant pressure:

$$P_{acc} = \min \left[1, \exp \left\{ - \mathbf{b} \left[dU_V + P dV_B - N \mathbf{b}^{-1} \ln \left(V_{B,n} / V_{B,o} \right) \right] \right\} \right] \quad (4.5)$$

In the above equations, $\mathbf{b}=1/k_B T$ is the reciprocal of the Boltzmann constant times the temperature, dU_i are the changes in configurational energy involved in each step, N_i is the number of molecules of component i present in the system, and q_i is the partition function for species i . In the volume change steps, $V_{B,o}$ is the original volume, $V_{B,n}$ is the new system volume, and dV_B is the difference between these two volumes, $V_{B,n}-V_{B,o}$. In order to maintain microscopic reversibility within the reacting system, the forward and reverse reaction steps, labeled (B) and (C) above, must be attempted with an equal probability. During the forward and reverse reaction steps, the newly created molecules are placed in the cavities left by the deleted molecules, which tends to aid in convergence at higher densities. In simulations, these reacting systems were typically equilibrated for 30×10^6 moves and averages taken for 80×10^6 moves, with moves (A), (B), (C), and (D) selected 39.9%, 30%, 30%, and 0.1% of the time, respectively.

4.2.2 Constant Pressure Gibbs Ensemble Monte Carlo

One of the goals of this study was to calculate the equilibrium yield of ethyl acetate when this reaction is allowed to absorb within a microporous carbon support, and compare the equilibrium yield to that in the bulk gas phase. In order to make this type of comparison, we performed two-phase simulations, consisting of a slit-shaped carbon pore and a bulk gas

phase, by implementing a simulation technique called constant pressure Gibbs Ensemble Monte Carlo [39,40]. This two-phase simulation technique is easily combined with the RxMC framework shown previously, by incorporating particle swaps between the bulk phase and the pore phase. The acceptance probabilities for these exchange moves are shown in Eqs. (4.6) and (4.7):

(E) **Bulk to Pore** : random molecule transfer from the bulk phase to the pore phase:

$$P_{acc} = \min \left[1, \exp \left(-\mathbf{b}dU_{N_{B,i}-1} - \mathbf{b}dU_{N_{P,i}+1} \right) \times \frac{N_{B,i}V_P}{(N_{P,i}+1)V_B} \right] \quad (4.6)$$

(F) **Pore to Bulk** : random molecule transfer from the pore phase to the bulk phase:

$$P_{acc} = \min \left[1, \exp \left(-\mathbf{b}dU_{N_{P,i}-1} - \mathbf{b}dU_{N_{B,i}+1} \right) \times \frac{N_{P,i}V_B}{(N_{B,i}+1)V_P} \right] \quad (4.7)$$

In Equations (4.6) and (4.7), $N_{P,i}$ and $N_{B,i}$ represent the number of molecules of type i in the pore and bulk phase, respectively. V_B is the volume of the bulk phase and V_P is the volume of the pore phase. The exponential term in Equations (4.6) and (4.7) accounts for the total change in potential energy associated with the particle transfer. All but one of the molecular species participating in the reaction needs to be swapped between the two phases, as the equilibrium of the last species will be completely satisfied by the RxMC reaction steps within each of the two discrete phases. In order to increase sampling efficiency, only the smaller species should be exchanged between the bulk and the pore. Consequently, in our

simulations only water, acetic acid, and ethanol were exchanged. It is important that for each molecular species being transferred there exists an equal probability of attempting the two exchange steps, (E) and (F) above.

4.3 Simulation Models

In all of the simulations, site-site Lennard-Jones (LJ) plus Coulomb interactions were used to calculate the potential energy between molecule pairs, i and j :

$$u_{i,j} = \sum_a \sum_b \left\{ 4\mathbf{e}_{ia,jb} \left[\left(\frac{\mathbf{s}_{ia,jb}}{r_{ia,jb}} \right)^{12} - \left(\frac{\mathbf{s}_{ia,jb}}{r_{ia,jb}} \right)^6 \right] + \frac{q_{ia}q_{jb}}{r_{ia,jb}} \right\} \quad (4.8)$$

In Eq. (4.8), r is the distance between interaction sites \mathbf{a} and \mathbf{b} located on molecule i and j , respectively. The cross-term LJ parameters between unlike interaction sites, were calculated according to the Lorentz-Berthelot mixing rules: $\mathbf{e}_{ia,jb} = (\mathbf{e}_{ia}\mathbf{e}_{jb})^{1/2}$ and $\mathbf{s}_{ia,jb} = (\mathbf{s}_{ia} + \mathbf{s}_{jb})/2.0$. Additional charge sites, with an elementary charge of q , are positioned on the molecules in order to account for electrostatic interactions and hydrogen bonding.

During the simulations, the LJ potential energy term was calculated between two molecules when their center of mass separation was less than 2.0 nm. The electrostatic part of the potential energy was calculated when this separation distance was less than 4.0 nm.

Although the truncation of the electrostatic potential at a distance of 4.0 nm may lead to small errors in the energy calculation, using Ewald sums [41] to correct for the truncated

potential was not attempted. Ewald sums were avoided due to the high computational cost leading to only a slight gain in accuracy. This was confirmed by Shevade *et al.* [42], who have simulated a qualitatively similar system, the selective adsorption of water/methanol mixtures in carbon pores. They report a slow down of two orders of magnitude by incorporating the Ewald sum method, with an energy difference of less than 1%.

Table 4.1 Summary of potential parameters used in the current RxMC simulations.

Molecule	Site	q/e	s/nm	$e/k_B/K$	Geometry
water ref. [43]	O	0.0	0.315	78.1	O-H: 0.9572 nm
	H	+0.52	0.0	0.0	O-M: 0.015 nm
	M	-1.04	0.0	0.0	$\angle\text{HOH}$: 104.52°
ethanol ref. [44]	CH ₃	0.0	0.3775	104.238	C-C: 0.153 nm
	CH ₂	0.265	0.3905	59.421	C-O: 0.143 nm
	O	-0.70	0.307	85.606	O-H: 0.0945 nm
	H	0.435	0.0	0.0	$\angle\text{CCO}$: 108°, $\angle\text{COH}$: 108.5°
acetic acid ref. [45]	CH ₃	0.08	0.391	80.570	C-C: 0.1520 nm
	C	0.55	0.375	52.874	C=O: 0.1214 nm
	=O	-0.50	0.296	105.749	C-O: 0.1364 nm
	O	-0.58	0.300	85.606	O-H: 0.0970 nm
	H	0.45	0.0	0.0	$\angle\text{COH}$: 107°, $\angle\text{OCO}$: 123°, $\angle\text{CCO}$: 111°
ethyl acetate (this work)	CH ₃	-0.058	0.3775	104.238	CH ₃ -CH ₂ : 0.1512 nm
	CH ₂	0.481	0.3905	59.421	CH ₂ -O: 0.1445 nm
	O	-0.517	0.300	85.606	O-C: 0.1347 nm
	C	0.842	0.375	52.874	C=O: 0.1204 nm
	=O	-0.694	0.296	105.749	C-CH ₃ : 0.1506 nm
	CH ₃	-0.054	0.391	80.570	$\angle\text{CCH}_2\text{O}$: 108°, $\angle\text{COC}$: 117°, $\angle\text{OCO}$: 124°, $\angle\text{O-CCH}_3$: 111°
carbon dioxide ref. [46]	C	0.6512	0.2757	28.129	C-O: 0.1149 nm
	O	-0.3256	0.3033	80.507	
carboxyl groups (on pore surface) ref. [47]	C	0.08	0.340	28.0	C-C: 0.152 nm
	=C	0.55	0.375	52.836	C=O: 0.1214
	=O	-0.50	0.296	105.673	C-O: 0.1364
	O	-0.58	0.300	85.551	O-H: 0.0970
	H	0.45	0.0	0.0	$\angle\text{CC=O}$: 126°, $\angle\text{CC-O}$: 111°, $\angle\text{C-O-H}$: 107°
carbon (pore) ref. [48]	C	0.0	0.340	28.0	

The LJ and coulomb interactions are summarized in Table 4.1 for each molecule participating in the reaction, as well as for the inert carbon dioxide used as a solvent and the carbon associated with the slit-pore model. In addition to the intermolecular interactions, the models for ethanol, acetic acid and ethyl acetate also included an *intramolecular* torsional potential. The form of the torsional potential, Eq. (4.9), was similar for all three models, with different parameters assigned to each molecule, as shown in Table 4.2.

$$V(\Phi) = 0.5V_1(1 + \cos \Phi) + 0.5V_2(1 - \cos 2\Phi) + 0.5V_3(1 + \cos 3\Phi) \quad (4.9)$$

Table 4.2 Coefficients for the intramolecular potential function shown in Eq. (4.9).

Molecule	Dihedral Bond	V_1 (kcal/mol)	V_2 (kcal/mol)	V_3 (kcal/mol)
acetic acid	CCOH	4.98	6.20	0.0
ethanol	CCOH	0.834	-0.116	0.747
ethyl acetate	CCH ₂ OC	0.834	-0.116	0.747
	CH ₂ OCC	4.98	6.20	0.0

Before the RxMC simulations were performed, pure component simulations were used to verify the density, energy, and radial distribution functions of these models (data not shown) by comparing with the references shown in Table 4.1. Excellent agreement was found with the experimental literature data for ethanol, water, and acetic acid.

While reliable models were available in the literature for ethanol, water, and acetic acid (references shown in Table 4.1), a complete molecular model for ethyl acetate could not be found. Therefore, we constructed a model for ethyl acetate by combining the LJ interaction parameters for ethanol and acetic acid with quantum mechanical calculations for the

equilibrium geometry and the charge distribution of an isolated ethyl acetate molecule. The quantum mechanical calculations were performed with *Gaussian 98* [49] using the density functional theory (DFT) method in conjunction with the B3LYP functional. This is a hybrid functional which combines Becke's three parameter exchange functional [50] and the Lee-Yang-Parr correlation functional [51]. The basis set used for the geometry optimization and for calculating the charge distribution (using a Mulliken population analysis) was the 6-311G++(3df,3pd) basis set. This basis set includes three sizes of contracted functions for each orbital, adds diffuse functions to both heavy atoms and hydrogens, and adds polarization functions: 3 d-type and 1 f-type functions on heavy atoms, and 3 p-type and 1 d-type functions on the hydrogens. The DFT results for the approximate charge distribution and the geometry optimization are included in Table 4.1. In order to account for the intramolecular potential for ethyl acetate, we combined the torsional potentials from acetic acid and ethanol (Table 4.2) along with intramolecular LJ interactions between sites separated by more than three bonds. The LJ interactions for ethyl acetate were taken from the ethanol and the acetic acid molecules. Using our approximate model for ethyl acetate, we were able to accurately predict the density of ethyl acetate in the liquid phase by using a Monte Carlo simulation at constant temperature and pressure. At a temperature of 25°C the experimental density in the liquid phase is 0.9006 g/cm³ while the simulated density is found to be 0.9386 g/cm³, which is a difference of around 4%.

The partition functions for water, ethanol, acetic acid, and ethyl acetate used in the RxMC acceptance criteria were also taken from DFT calculations, using the same basis set and

B3LYP functional. The vibrational frequencies and zero-point energies were appropriately scaled by a factor of 0.989, due to the comparisons presented by Bauschlicher and Partidge [52]. The predicted vibration frequencies (unscaled) and rotational constants from these calculations are shown in Table 4.3. The difference in electronic energy between the reactants and products (ΔD_0), including zero-point energy corrections and scaling, was calculated to be 8.366 kcal/mol. This value was adjusted, to a final value of 5.204 kcal/mol, in order to match the experimental conversion in the ideal gas phase (Figure 4.1). The difference between these two values of ΔD_0 is within the limits of accuracy of the DFT calculations, which are generally accepted to be accurate to within a few kcal/mol of experimental measurements.

Table 4.3 Rotational and vibrational constants used in the partition functions.

Molecule	Rotational Temp/K	Vibrational Frequencies/K
water	39.615, 20.684, 13.589	5629.26, 5486.71, 2340.21
ethanol	1.697, 0.448, 0.390	337.61, 397.73, 601.90, 1183.65, 1290.45, 1481.75, 1582.05, 1696.49, 1821.00, 1870.61, 2024.61, 2084.51, 2134.35, 2158.95, 2195.91, 4291.43, 4328.96, 4366.97, 4463.03, 4469.00, 5528.72
acetic acid	0.530, 0.461, 0.255	148.40, 622.43, 681.37, 682.63, 863.98, 1232.26, 1422.11, 1531.63, 1726.87, 1860.11, 2013.54, 2119.87, 2141.75, 2668.07, 4370.60, 4452.17, 4543.18, 5482.75
ethyl acetate	0.406, 0.100, 0.083	77.91, 101.07, 217.82, 276.83, 375.27, 529.77, 620.76, 880.29, 918.38, 1172.71, 1236.66, 1361.33, 1457.52, 1534.86, 1537.78, 1634.74, 1697.85, 1817.34, 1867.36, 2005.67, 2024.96, 2053.59, 2119.09, 2127.82, 2139.87, 2156.87, 2187.73, 2579.65, 4371.65, 4391.48, 4393.84, 4443.04, 4467.54, 4475.41, 4482.85, 4545.01

The interaction between the reacting adsorbate molecules and the carbon slit-pore was modeled with the 10-4-3 Steele potential [48]:

$$U_{ia,c}(z) = 4pe_{ia,c}s_{ia,c}^2\Delta r_c \left[\frac{1}{5} \left(\frac{s_{ia,c}}{H/2 \pm z} \right)^{10} - \frac{1}{2} \left(\frac{s_{ia,c}}{H/2 \pm z} \right)^4 - \frac{s_{ia,c}^4}{6\Delta(H/2 \pm z + 0.61\Delta)^3} \right] \quad (4.10)$$

This model assumes that the carbon pore is constructed of two parallel walls that are infinite in the x-y plane. The structure of these walls is assumed to be that of sheets of graphite, and the surface corrugation is neglected by averaging the carbon potential over the two graphitic pore surfaces. As a result, the interaction potential between an adsorbate molecule and the pore wall is only a function of the z-coordinate, the distance from each pore wall. In Eq. (4.10), H is the width of the pore, defined as the distance between carbon centers on the two opposing walls of the pore, Δ is the experimentally measured interlayer spacing of graphite (0.335 nm), r_c is the experimentally measured density of graphite (2.27 g/cm³), and e and s are the LJ parameters of carbon shown in Table 4.1.

In some of the simulations, carboxyl groups were placed on the surface of the pore in order to mimic the chemical activation process often applied to the experimental materials. In our simulation model, the carboxyl groups were oriented perpendicular to the pore surface, with a random orientation. The carboxyl groups were placed at random positions on the pore

surface, with the physical restriction that the sites could not overlap each other, as shown in Figure 4.2. The potential parameters for the carboxyl sites are taken from ref. [47] and summarized in Table 4.1.

4.4 Simulation Results

4.4.1 Esterification in the Bulk Gas Phase

As with our studies in the previous Chapters, we began by modeling the equilibrium conversion of ethyl acetate in the bulk gas phase, where experimental comparison was possible. This was done in order to verify our molecular models and to refine the electronic contribution (ΔD_0) to the molecular partition functions, as the reaction conversion is particularly sensitive to this parameter.

Hawes and Kabel provide a thorough review of the vapor-phase equilibrium constant of the esterification reaction [8] measured by several different authors. Our simulated conversion of ethyl acetate is compared with the experimental results of Tidwell and Reid [53] and with Hoerig *et al.* [54] in the gas phase, as shown in Figure 4.1. Although Tidwell and Reid did not specifically account for any side reactions, their equilibrium data falls within a few percent of the most accurate equilibrium data assembled by Hawes and Kabel [8].

Additionally, the data from both Tidwell and Reid and Hoerig *et al.* represents two of the largest temperature ranges measured from the data sets compiled by Hawes and Kabel, which was important for the validation of our simulations. In order to achieve close agreement with the experimental data, we refined our value of ΔD_0 (change in ground state electronic energy

between reactants and products) for this reaction from an initial DFT estimate of 8.366 kcal/mol to a final value of 5.204 kcal/mol. This adjustment tends to only affect the y-axis position of our conversion versus temperature curve shown in Figure 4.1, but not the characteristic shape of the curve. After fitting this single parameter, our simulations show excellent agreement with the experimental data over a wide temperature range, at a constant pressure of 1.0 bar. It is noted that calculating the equilibrium constant from thermodynamic tables can lead to errors, due to the sensitive logarithmic dependence on these quantities. The standard entropy and enthalpy changes in reaction are small in comparison to the thermal data employed to obtain them. Thus, we have compared our simulation results only to reliable experimental data.

4.4.2. Esterification in Supercritical Carbon Dioxide

Once we verified our simulation results against experiments in the bulk gas phase, we then began studying the conversion of the esterification reaction in a carbon dioxide solvent. We have found two separate experimental studies in the literature [17,18] which have studied ethyl acetate production in carbon dioxide solvent, and both groups report enhanced equilibrium conversion over the neat reaction.

Blanchard and Brennecke [18] report that the conversion of ethyl acetate can be increased by pressurizing the neat liquid phase reaction with carbon dioxide. They find that the equilibrium yield can be shifted from 63% conversion to 72% conversion at a temperature of 333 K by pressurizing the system to 58.6 bar, through the addition of the CO₂ solvent. The

mole fraction of CO₂ in their system is 0.30. Since the total number of moles in the reaction is conserved, it is not expected that the reaction would be sensitive to the pressure. The authors attribute the observed equilibrium shift to pressure-induced non-ideality in the liquid phase and preferential solubilization of ethyl acetate in the CO₂, which ultimately increases the conversion. Although the conversion is enhanced in this study, it is not clear whether the equilibrium shift is merely due to the increased pressure or to specific interactions with the carbon dioxide. It seems that the equilibrium of the neat reaction at such an elevated pressure (58.6 bar) should also be measured, as a strict comparison.

In a separate study, Hou *et al.* [17] found similar results when measuring the esterification reaction in a CO₂ solvent. They studied the same reaction at a temperature of 333.2 K but with a higher mole fraction of CO₂ of 0.90. The results of Hou *et al.* are more interesting, as the conversion is measured as a function of the total system pressure. At sub-critical conditions, the conversion increased with the applied CO₂ pressure and reaches a maximum (70% conversion) near the critical point of the fluid. As the pressure is further increased beyond the critical pressure, the conversion quickly declines to a value below the sub-critical conversion (62% conversion). This phenomena in the reaction conversion is attributed by the authors to the local density enhancement or clustering which occurs near the critical point of the fluid. This clustering effect is perceived to shift the equilibrium by altering the activity coefficients of the molecules in the system. However, like the previous study [18], it is not clear whether the effect on the reaction conversion is merely due to pressure increases or if there are specific solvent-solute interactions that are responsible for shifting the conversion.

In order to clarify the interpretation of the previous measurements, we have simulated the conversion of ethyl acetate in CO₂ near the critical point of the mixture. In our study, we have performed simulations starting from a mixture of CO₂, ethanol, and acetic acid with an initial mole ratio of 90:5:5, respectively. The carbon dioxide model [46] used in the simulations reproduces the experimental critical point of pure CO₂ ($T_c=304.2$ K and $P_c=73$ bar) within the limits of statistical error. The starting composition of our system is identical to the mixture studied by Hou *et al.* [17]. In our RxMC simulations, we have maintained a constant pressure of 103.3 bar using an NPT ensemble, while varying the system temperature. We started above the critical point, at a temperature of 450 K, and we gradually lowered the temperature until we approached the experimental critical temperature of the fluid, 333.2 K [17]. The simulation results are shown in Figure 4.3.

As the temperature is lowered and the system approaches the critical point, there is a rapid increase in the reaction conversion. This shift in equilibrium conversion is more dramatic than that seen in the gas phase, Figure 4.1. We can explain the behavior of this reaction in the CO₂ solvent by looking at simulation snapshots as the system approaches the critical point. Figure 4.4 shows the configuration of ethyl acetate molecules at a temperature of 450 K in the presence of CO₂. Only ethyl acetate molecules are shown in order to clarify the illustration. The ethyl acetate molecules at 450 K are distributed fairly evenly throughout the system, with only a few associated pairs found. However, the system configuration dramatically changes as the temperature is lowered to 360 K. Figure 4.5 shows the

configuration of ethyl acetate molecules at this lower temperature, again with the other molecular species removed for clarity. At a temperature of 360 K, which coincides with the onset of the enhanced conversion, there is a significant amount of solvent clustering in the system. This is shown in Figure 4.6, as the CO₂ molecules cluster around the reacting solute molecules. Therefore, it is likely that this clustering phenomenon is directly responsible for the equilibrium enhancement, seen in both our simulations and the experimental system [17].

4.4.3 Esterification in Carbon Slit-Shaped Pores

As mentioned in the Introduction, activated carbons have been used successfully to entrap heteropoly acids (HPAs) for the catalytic esterification of acetic acid with ethanol [21,22]. Activated carbons have been utilized for the immobilization of HPAs, due to the undesirably high solubility of HPAs in polar fluids. Using the HPA catalyst in activated carbon, Izumi and Urabe [21] report a conversion of 95% at a reaction temperature of 423K and a conversion of 83% at a temperature of 393K. Additionally, they report that the HPA entrapped in activated carbon results in a much higher selectivity for ethyl acetate (99.5%), as compared to the silica-supported HPA (71.8%), which can yield a significant amount of diethyl ether as a by-product. It is surprising that the equilibrium conversion in this study increases with respect to temperature, as the equilibrium constant would predict the opposite dependence. However, there are two possibilities that may explain this unlikely result. First, selective adsorption of ethanol, acetic acid, or water in the pores may affect the conversion. Second, the results at the lower temperature may not be fully equilibrated, which could underestimate the equilibrium yield at 393 K. If these experiments had also been started

from the other direction (starting from products), the experimental results would be more convincing.

Chu *et al.* [22] have also studied the production of ethyl acetate with HPAs immobilized on activated carbon. Their results are shown in Table 4.4. Again, the experimental conversion increases with respect to temperature, opposite of the results in the ideal gas phase.

However, Chu *et al.* [22] concede that conversions below 85% have not yet reached equilibrium.

Table 4.4 Yield of ethyl acetate in activated carbon as reported by Chu *et al.* [22].

Temperature/K	373.15	383.15	393.15	403.15	413.15	423.15
Conversion %	67.9	69.7	74.9	77.8	83.6	87.3

These two experimental studies [21,22], as well as others [19,20], suggest that HPA/carbon catalysis may be a viable alternative for the production of ethyl acetate. In order to supplement this interest, we have modeled this equilibrium-limited reaction in carbon slit-pores of various widths (H). Our RxMC simulation results of the esterification reaction in carbon slit-pores (activated and unactivated) are shown in Figure 4.7. Figure 4.7 shows the mole fraction of ethyl acetate versus the width of the pore (H) at a constant temperature of 573.15 K and a corresponding bulk phase pressure of 1.0 bar. The simulated mole fraction of ethyl acetate is shown for a slit-shaped carbon pore and for a slit-pore modified by activated sites (carboxyl groups) at a site density of 1.82 sites/nm². The mole fraction of ethyl acetate in a bulk gas phase at the same temperature and pressure, as predicted by our simulations, is shown for comparison.

As compared to the bulk gas phase reaction, the mole fraction within the pore is significantly enhanced. However, the differences in the simulation results between the activated pore and the unactivated pore are rather subtle. The maximum mole fraction of ethyl acetate in the two models is relatively similar, 0.882 for the unactivated smooth pore and 0.898 for the activated pore. However, these maxima correspond to different pore widths (H). This is due to the fact that the protrusion of the carboxyl groups into the pore space effectively reduces the pore width of the activated pore, and shifts the maximum conversion to higher values of H . This would also explain the rapid descent of the ethyl acetate mole fraction at low values of H . At a pore width of 0.80 nm, the activated pore geometrically inhibits ethyl acetate formation, due to the additional protrusion of the carboxyl groups. In the unactivated pore, which is free of carboxyl groups, the pore space is not as restricted and tends to be a more favorable environment for ethyl acetate formation.

Although the mole fraction of ethyl acetate within these carbon pores is significantly enhanced, the overall mole fraction of ethyl acetate (bulk phase + pore phase) is not as dramatically affected. The main contribution to the elevated mole fraction within the pore space appears to be selective adsorption of ethyl acetate from the bulk phase, and as a consequence, the mole fraction of ethyl acetate in the corresponding bulk phase tends to decrease. This effect can be seen by comparing the overall reaction conversion (bulk gas phase + pore phase) with the conversion in an isolated gas phase. This comparison is shown in Figure 4.8 for the unactivated slit-shaped carbon pore and in Figure 4.9 for the activated

carbon pore model at a temperature of 523.15 K and a pressure of 1.0 bar. While it is obvious from Figures 4.8 and 4.9 that the elevated pore phase mole fraction is primarily due to selective adsorption, it is also shown that the selective adsorption is coupled with moderate increases in the overall reaction yield (up to 6%).

Since the pore environment favors the formation of ethyl acetate, the overall reaction yield can be further enhanced by reducing the ratio of the bulk phase volume to the pore phase volume, $V_{\text{bulk}}/V_{\text{pore}}$. This enhancement is illustrated in Figure 4.8, which shows the shift in the overall conversion by reducing the ratio of $V_{\text{bulk}}/V_{\text{pore}}$ from the original value of 1057 to a value of 68, which is achieved by increasing the volume of the pore. Similar enhancements in overall reaction conversion were seen in the activated pore model when the ratio of $V_{\text{bulk}}/V_{\text{pore}}$ was decreased (data not shown).

We have studied the effects of chemical activation further by measuring the overall system conversion versus the carboxyl surface density. Simulation results are shown in Figure 4.10 for a fixed pore width of $H=2.0$ nm, a bulk phase pressure of 1.0 bar, and a temperature of 523.15 K. The overall conversion is shown to increase linearly with respect to increasing surface activation. Figure 4.10 also shows the simulated conversion in an isolated bulk gas phase for comparison. While the addition of carboxyl groups tends to enhance the conversion, this enhancement cannot be attributed to specific interactions between the carboxyl groups and the ethyl acetate molecules. The main cause of the enhancement seems to arise from increased confinement effects. Figure 4.11 shows a simulation snapshot of this

system at the highest surface site density, with only ethyl acetate molecules shown. There are no strong correlations between ethyl acetate and the carboxyl sites, as evidenced by the fairly random ordering of ethyl acetate on the pore surface. Many carboxyl sites are empty and a significant fraction of the ethyl acetate molecules are adsorbed on unactivated areas of the smooth pore surface.

We have also attempted to explain the peculiar temperature dependence of the reaction conversion experimentally measured in carbon pores [21,22] by simulating the esterification reaction at a slightly lower temperature, 473.15 K. Simulation results at a temperature of 473.15 K are compared with those at 523.15 K in Table 4.5. This table shows the average number of molecules in each phase, as well as the mole percent of ethyl acetate in each phase and the total conversion (bulk + pore).

Table 4.5 Simulation results of the esterification reaction in a smooth carbon slit-pore of width $H=2.00$ nm. The average number of molecules in each phase is shown.

Molecule	$T = 473.15$ K		$T = 523.15$ K	
	BULK	PORE	BULK	PORE
acetic acid	70.23	78.82	165.38	12.08
ethanol	143.08	5.98	175.60	1.86
water	703.73	11.21	684.95	1.59
ethyl acetate	316.69	398.26	603.42	83.12
% ethyl acetate	25.7%	80.6%	37.0%	84.3%
% conversion	82.7%		79.5%	

It is interesting to see in Table 4.5 that although the total conversion decreases with temperature, the mole fraction of ethyl acetate in the pore phase increases. The increase in ethyl acetate composition within the pore phase at 523.15 K is directly attributed to selective

adsorption from the bulk gas phase, since the overall conversion at the higher temperature is actually lower. The simulation results shown in Table 4.5 should be considered when interpreting the experimental measurements by Chu *et al.* [22] and by Izumi and Urabe [21]. There are no comments made by either of the experimental groups concerning their measured trend of conversion versus temperature. However, it seems likely that selective adsorption of ethyl acetate within the microporous carbons could explain the surprising experimental observations.

4.5 Conclusions

In this study, we have demonstrated the effects of a supercritical solvent and selective adsorption in carbon micropores on the equilibrium conversion of acetic acid and ethanol to form ethyl acetate. In the bulk gas phase we achieve close agreement with the experimental results [53,54] over a fairly broad range of temperatures. Using the same molecular models as in the bulk gas phase, we have examined the equilibrium behavior of this reaction in 90 mole % CO₂, near the critical point of the mixture. Our RxMC simulations justify the results and suggestions of the experimental studies [17,18]. More specifically, we see increased conversion near the critical point of the fluid, and this maximum in conversion is clearly coupled with clustering of the ethyl acetate molecules in the system. While in this study we have presented only equilibrium reaction conversions, there are several other studies which have found dramatic rate enhancements (up to 30-fold) by conducting other esterification reactions in scCO₂ [55,56].

We have also used RxMC simulations to investigate the equilibrium yield of ethyl acetate in carbon slit-shaped pores, which are approximate models for activated carbon fibers. The simulations predict a moderate increase in the overall yield (6%) by adsorbing the reaction into a carbon pore, and a slightly larger increase when the pore is activated with carboxyl groups. The reaction conversion shows relatively little sensitivity to the pore width, until the pore becomes too narrow to allow the formation of ethyl acetate. Most importantly, we find that ethyl acetate is selectively adsorbed within the carbon pores during the reaction. This aspect could be highly desirable for designing an efficient process for simultaneous reaction and separation. Furthermore, we believe that selective adsorption could explain the surprising experimental results, which show an increase in reaction conversion with increasing temperature, using similar systems and conditions.

References

- [1] R. Koster, B. van der Linden, E. Poels, and A. Blik, *Journal of Catalysis* 204 (2001), 333.
- [2] W. Swietoslowski, *Journal of Physical Chemistry* 37 (1933), 701.
- [3] Lowenheim, F. A. and Moran, M. K. , *Industrial Chemicals*, Wiley: New York, (1975).
- [4] A. Darlington and W. B. Guenther, *Journal of Chemical and Engineering Data* 12 (1967), 605.
- [5] Y. W. Kang, Y. Y. Lee, and W. K. Lee, *Journal of Chemical Engineering of Japan* 25 (1992), 649.
- [6] H. Okur and M. Bayramoglu, *Industrial and Engineering Chemistry Research* 40 (2001), 3639.
- [7] S. Tsvetkov and R. P. Stateva, *Collection of Czech.Chem.Communications* 62 (1997), 558.
- [8] R. W. Hawes and R. L. Kabel, *AIChE Journal* 14 (1968), 606.
- [9] C. Venkateswarlu, M. Satyanarayana, and M. N. Rao, *Industrial and Engineering Chemistry* 50 (1958), 973.
- [10] S. O. Hwang and Y. H. Park, *Bioprocess Engineering* 17 (1997), 51.
- [11] I. Mochida, Y. Anju, A. Kato, and T. Seiyama, *Journal of Catalysis* 21 (1971), 263.
- [12] H. J. Arnikaar, T. S. Rao, and A. A. Bodhe, *Journal of Chromatography* 47 (1970), 265.
- [13] K. Tanaka, R. Yoshikawa, C. Ying, H. Kita, and K. Okamoto, *Catalysis Today* 67 (2001), 121.
- [14] J. Giménez, J. Costa, and S. Cervera, *Industrial & Engineering Chemistry Research* 26 (1987), 198.
- [15] E. Santacesaria, D. Gelosa, P. Danise, and S. Carrá, *Journal of Catalysis* 80 (1983), 427.
- [16] Othmer, K., *Encyclopedia of Chemical Technology*, Wiley: New York, (1958).
- [17] Z. Hou, B. Han, X. Zhang, H. Zhang, and Z. Liu, *Journal of Physical Chemistry B* 105 (2001), 4510.
- [18] L. A. Blanchard and J. F. Brennecke, *Green Chemistry* 3 (2001), 17.

- [19] I. P. Mukhlenov, G. N. Buzanova, M. S. Éttsel, I. A. Kalmykova, and A. M. Osipov, *Journal of Applied Chemistry of the USSR* 61 (1988), 1231.
- [20] K. W. Baierl, B. F. Lueck, and A. J. Wiley, *Technical Association for the Pulp and Paper Industry* 56 (1973), 58.
- [21] Y. Izumi and K. Urabe, *Chemistry Letters* 5 (1981), 663.
- [22] W. Chu, X. Yang, X. Ye, and Y. Wu, *Applied Catalysis A: General* 145 (1996), 125.
- [23] P. G. Jessop, T. Ikariya, and R. Noyori, *Chemical Reviews* 99 (1999), 475.
- [24] O. Kajimoto, *Chemical Reviews* 99 (1999), 355.
- [25] A. Baiker, *Chemical Reviews* 99 (1999), 453.
- [26] S. C. Tucker, *Chemical Reviews* 99 (1999), 391.
- [27] S. R. Mukai, I. Ogino, L. Lin, Y. Kondo, T. Masuda, and K. Hashimoto, *Reaction Kinetics and Catalysis Letters* 69 (2000), 253.
- [28] Z. Chen, T. Iizuka, and K. Tanabe, *Chemistry Letters* 10 (1984), 1085.
- [29] J. K. Johnson, A. Z. Panagiotopoulos, and K. E. Gubbins, *Molecular Physics* 81 (1994), 717.
- [30] Johnson, J. K., *Advances in Chemical Physics*, edited by Ferguson, D. M., Siepmann, I., and Truhlar, D. G., Wiley: New York 105 (1999), 461.
- [31] W. R. Smith and B. Triska, *Journal of Chemical Physics* 100 (1994), 3019.
- [32] M. Lisal, W. R. Smith, and I. Nezbeda, *Journal of Chemical Physics* 113 (2000), 4885.
- [33] C. H. Turner, J. K. Johnson, and K. E. Gubbins, *Journal of Chemical Physics* 114 (2001), 1851.
- [34] W. R. Smith and M. Lisal, *Physical Review E*, (2002, in press).
- [35] C. H. Turner, J. Pikunic, and K. E. Gubbins, *Molecular Physics* 99 (2001), 1991.
- [36] C. H. Turner, J. K. Brennan, J. K. Johnson, and K. E. Gubbins, *Journal of Chemical Physics* 116 (2002), 2138.
- [37] M. Lisal, I. Nezbeda, and W. R. Smith, *Journal of Chemical Physics* 110 (1999), 8597.
- [38] M. Borówko and R. Zagórski, *Journal of Chemical Physics* 114 (2001), 5397.

- [39] A. Z. Panagiotopoulos, *Molecular Physics* 62 (1987), 701.
- [40] S. C. McGrother and K. E. Gubbins, *Molecular Physics* 97 (1999), 955.
- [41] Allen, M. P. and Tildesley, D. J., *Computer Simulation of Liquids*, Oxford: New York, (1987).
- [42] A. V. Shevade, S. Jiang, and K. E. Gubbins, *Molecular Physics* 97 (1999), 1139.
- [43] W. L. Jorgensen, S. Chandrasekhar, J. D. Madura, R. W. Impey, and M. L. Klein, *Journal of Chemical Physics* 79 (1983), 926.
- [44] W. L. Jorgensen, *Journal of Physical Chemistry* 90 (1986), 1276.
- [45] J. M. Briggs, T. B. Nguyen, and W. L. Jorgensen, *Journal of Physical Chemistry* 95 (1991), 3315.
- [46] J. G. Harris and K. H. Yung, *Journal of Physical Chemistry* 99 (1995), 12021.
- [47] A. V. Shevade, S. Jiang, and K. E. Gubbins, *Journal of Chemical Physics* 113 (2000), 6933.
- [48] Steele, W. A., *Interaction of Gases with Solid Surfaces*, Pergamon: Oxford, (1974).
- [49] Frisch, M. J., Trucks, G. W., Schlegel, H. B., Scuseria, G. E., Robb, M. A., Cheeseman, J. R., Zakrzewski, V. G., Montgomery, J. A., Stratmann, R. E., Burant, J. C., Dapprich, S., Millam, J. M., Daniels, A. D., Kudin, K. N., Strain, M. C., Farkas, O., Tomasi, J., Barone, V., Cossi, M., Cammi, R., Mennucci, B., Pomelli, C., Adamo, C., Clifford, S., Ochterski, J., Petersson, G. A., Ayala, P. Y., Cui, Q., Morokuma, K., Malick, D. K., Rabuck, A. D., Raghavachari, K., Foresman, J. B., Cioslowski, J., Ortiz, J. V., Stefanov, B. B., Liu, G., Liashenko, A., Piskorz, P., Komaromi, I., Gomperts, R., Martin, R. L., Fox, D. J., Keith, T., Al-Laham, M. A., Peng, C. Y., Nanayakkara, A., Gonzalez, C., Challacombe, M., Gill, P. M. W., Johnson, B. G., Chen, W., Wong, M. W., Andres, J. L., Head-Gordon, M., Replogle, E. S., and Pople, J. A., *Gaussian 98 (Revision A.1)*, Gaussian, Inc., Pittsburgh, PA, (1998).
- [50] A. D. Becke, *Journal of Chemical Physics* 98 (1993), 5648.
- [51] C. Lee, W. Yang, and R. G. Parr, *Physical Review B* 37 (1988), 785.
- [52] C. W. Bauschlicher Jr. and H. Partridge, *Journal of Chemical Physics* 103 (1995), 1788.
- [53] H. C. Tidwell and E. E. Reid, *Journal of the American Chemical Society* 53 (1931), 4353.

- [54] H. F. Hoerig, D. Hanson, and O. L. Kowalke, *Industrial and Engineering Chemistry* 35 (1943), 575.
- [55] J. B. Ellington and J. F. Brennecke, *Journal of the Chemical Society D - Chemical Communications* 13 (1993), 1094.
- [56] H. Nakaya, K. Nakamura, and O. Miyawaki, *Journal of the American Oil Chemists Society* 79 (2002), 23.

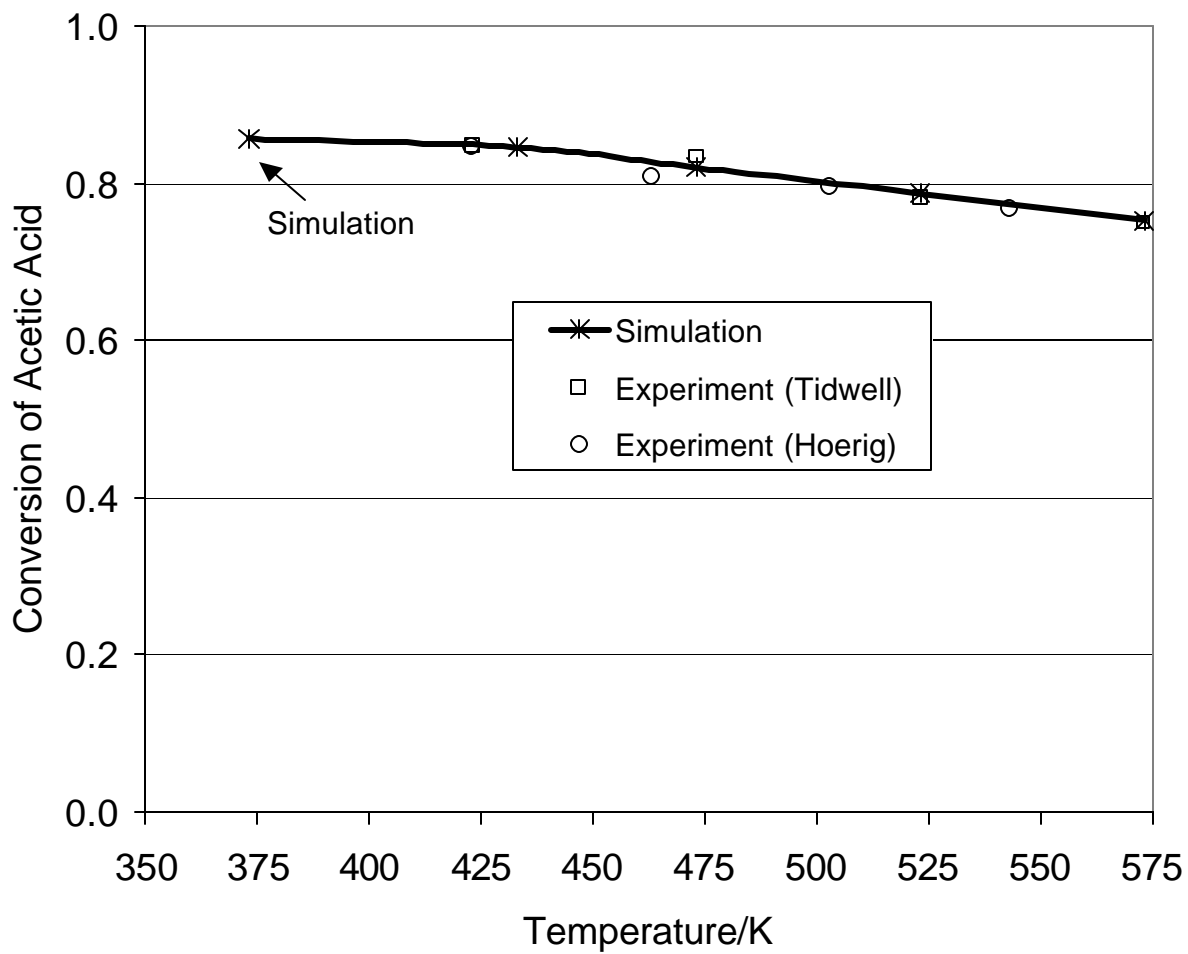


Figure 4.1 Conversion of acetic acid to ethyl acetate in the bulk gas phase at a total pressure of 1.0 bar. Our simulated conversion is shown along with the experimental measurements of ref. [53] and [54].

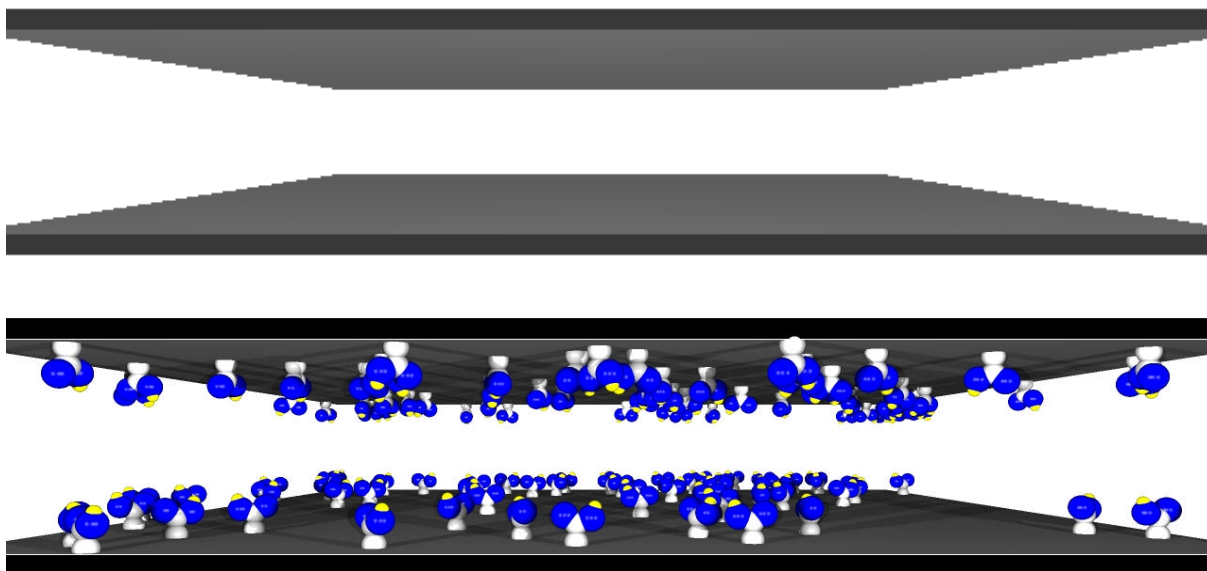


Figure 4.2 Illustration of the smooth slit-shaped carbon pore (top) and the slit-shaped carbon pore activated with carboxyl groups (bottom). In both types of pores, the carbon walls are modeled with the 10-4-3- Steele potential [48].

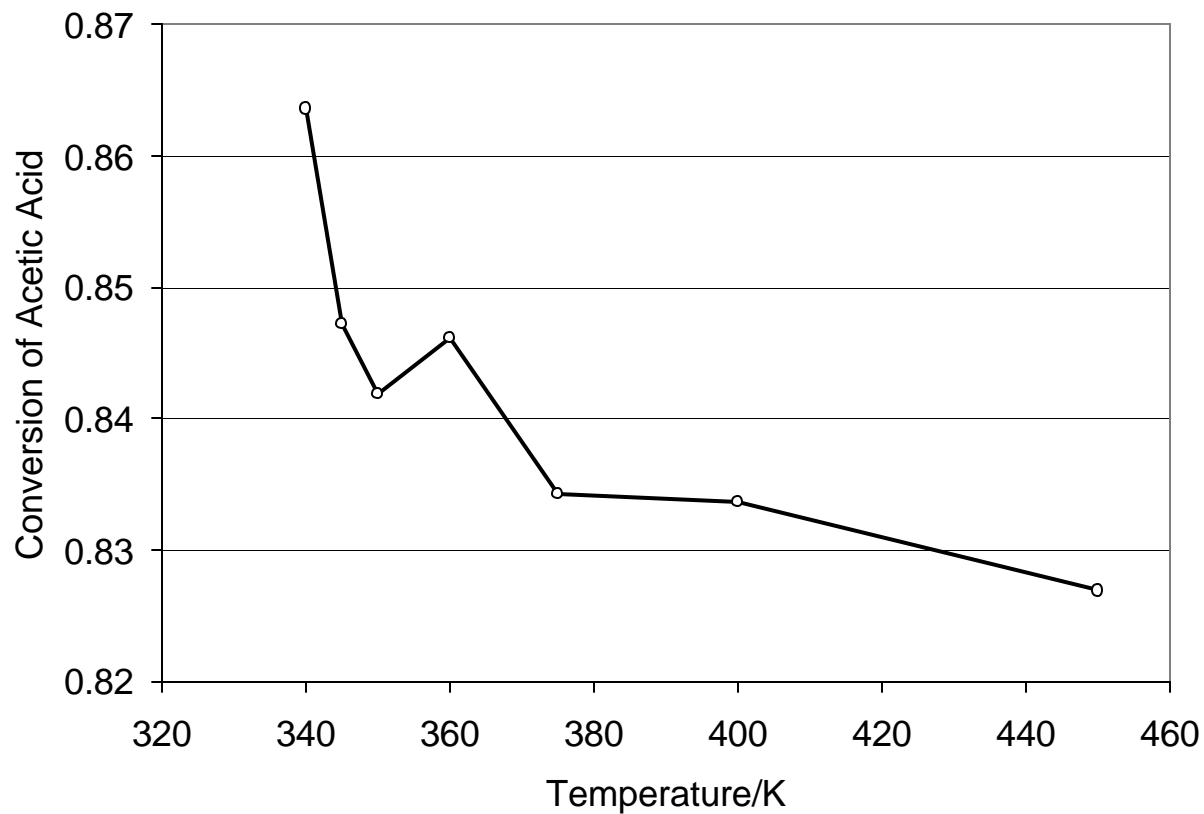


Figure 4.3 Equilibrium conversion of acetic acid to ethyl acetate in 90 mole % CO₂. The total system pressure is 103.3 bar. The experimental critical point of this mixture is measured to be at a temperature of 333.2 K and a pressure of 103.3 bar [17].

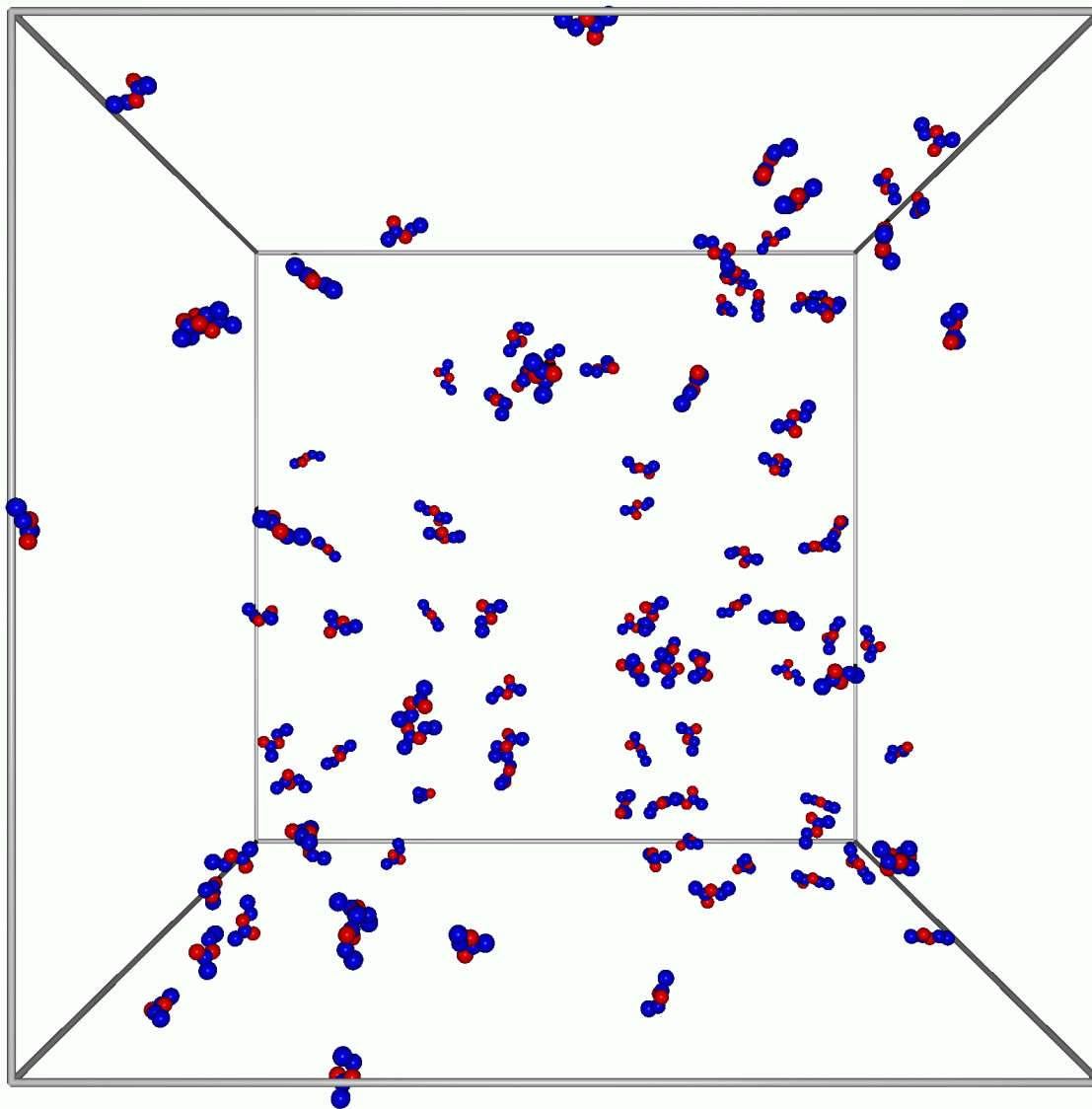


Figure 4.4 Simulation snapshot of the esterification reaction in 90 mole % CO_2 at 450 K. For clarity, only ethyl acetate molecules are shown. Oxygen sites are shown in red, while the carbon-containing interaction sites are shown in blue.

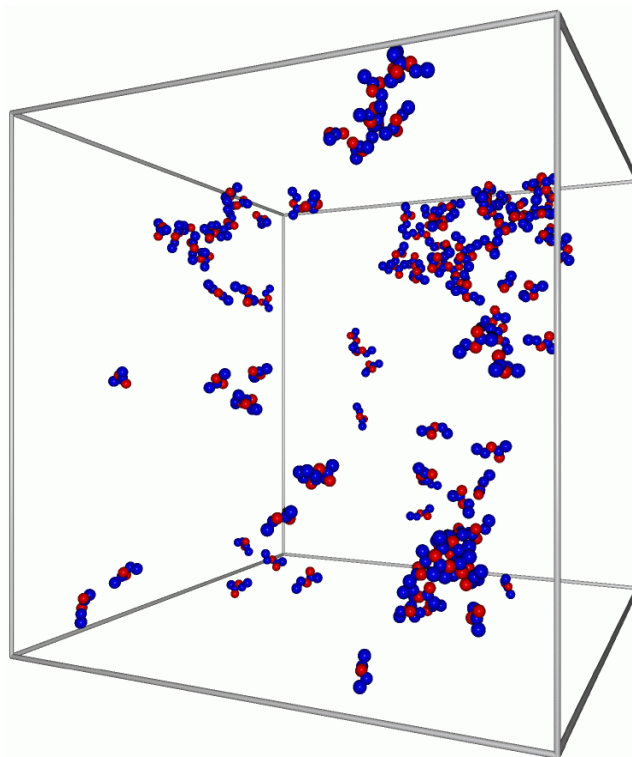
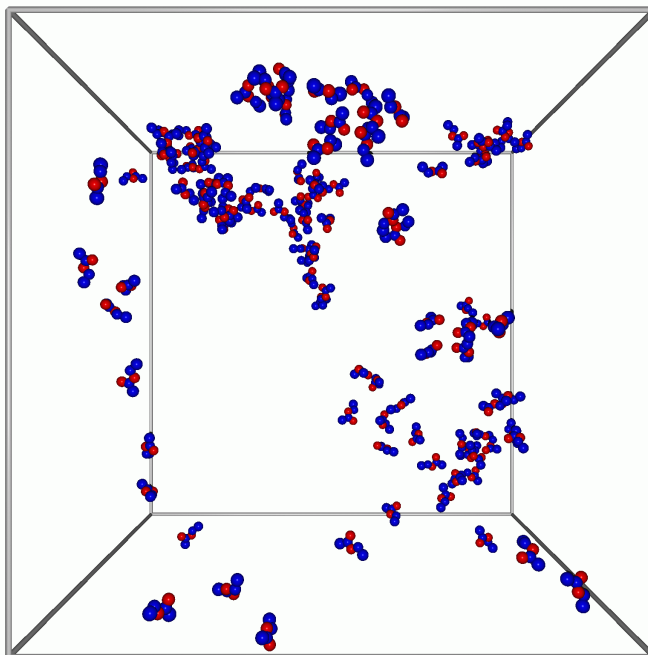


Figure 4.5 Simulation snapshot of the esterification reaction in 90 mole % CO₂ at 360 K. For clarity, only ethyl acetate molecules are shown. Snapshots are identical but with different orientations, showing significant clustering in the fluid.

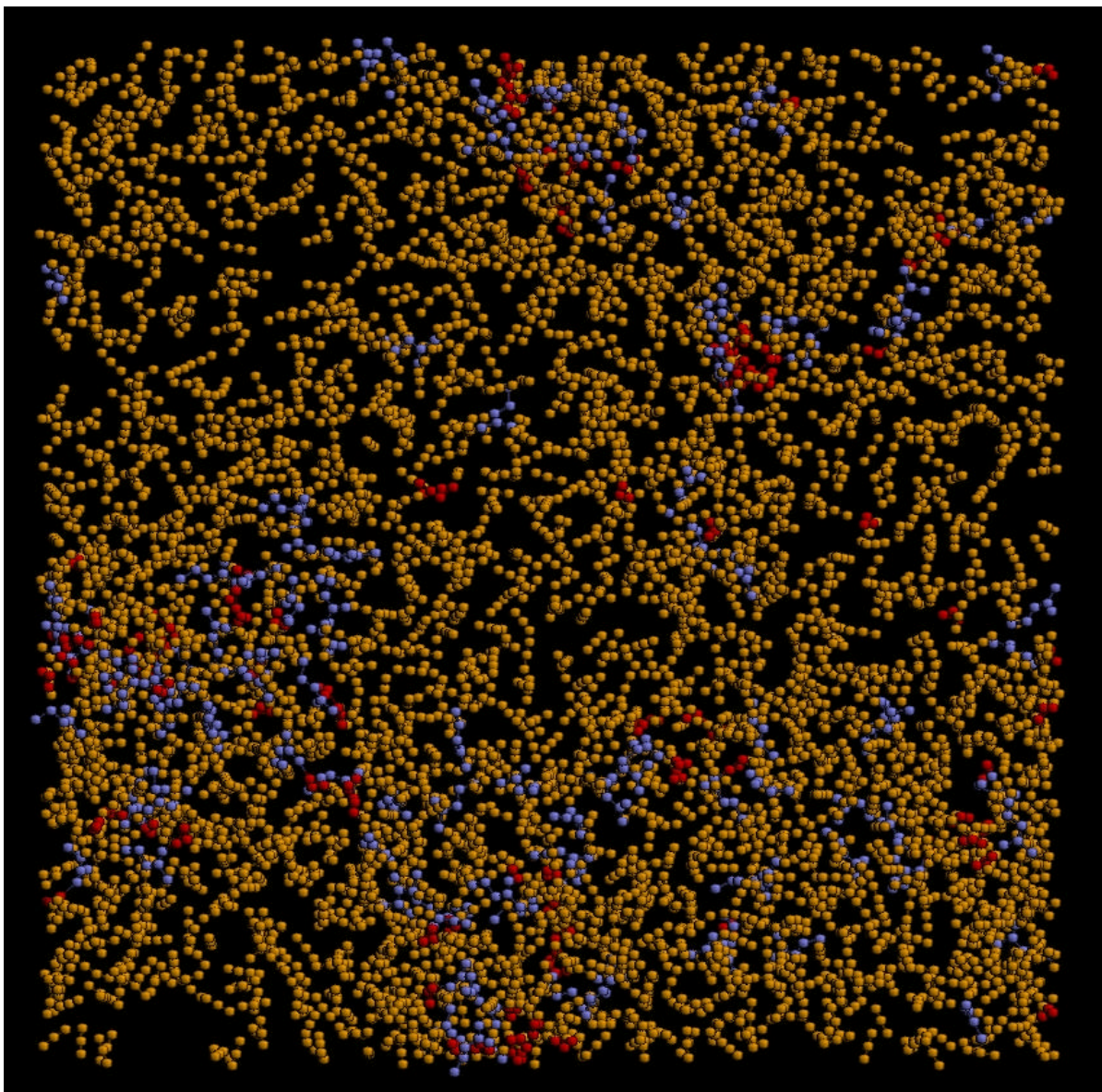


Figure 4.6 Simulation snapshot of the esterification reaction in 90 mole % CO₂ at 360 K and 103.3 bar. Carbon dioxide is shown in orange, water is shown in red, and ethyl acetate is shown in blue. The ethanol and acetic acid are removed for clarity.

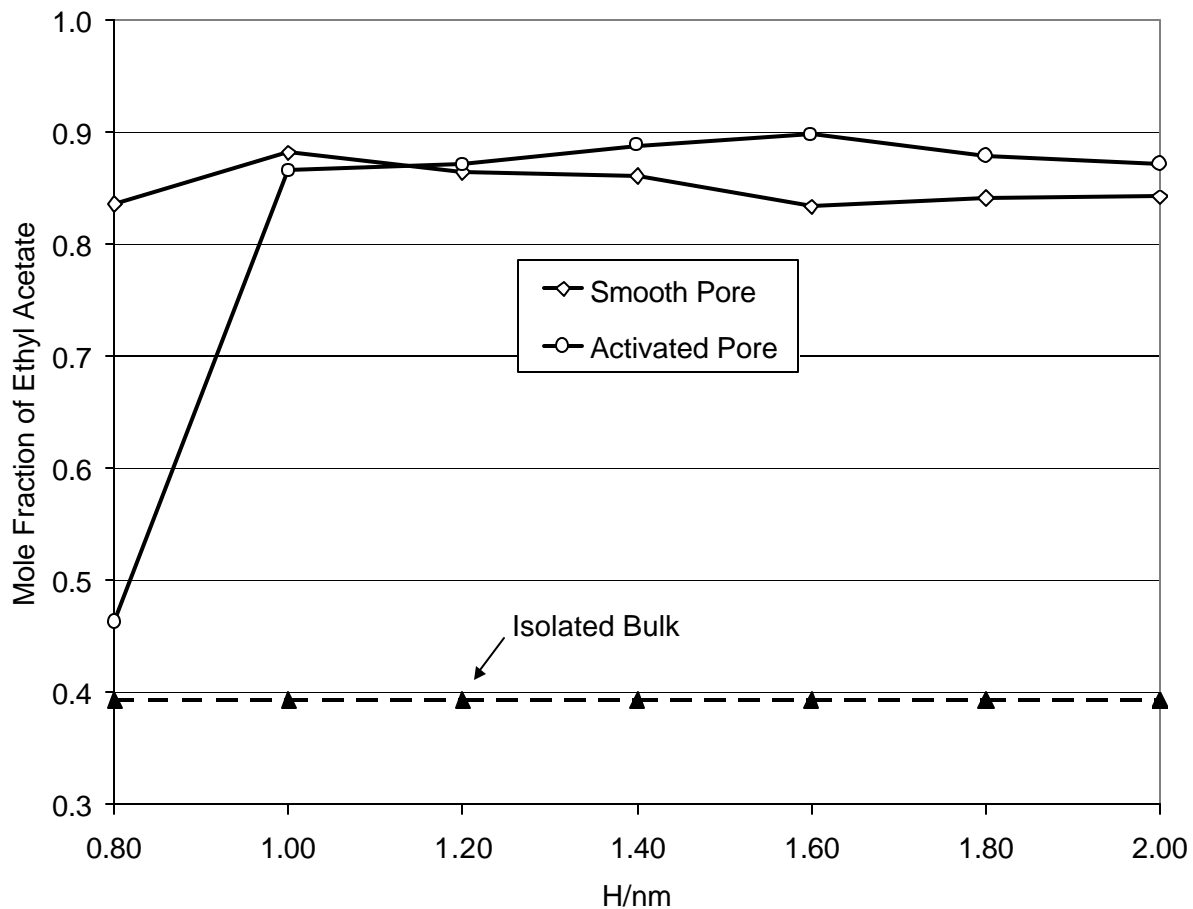


Figure 4.7 Mole fraction of ethyl acetate in the carbon slit pores (activated and unactivated) of a two-phase system. The mole fraction of ethyl acetate is plotted versus the pore width (H) at a temperature of 523.15 K and a bulk phase pressure of 1.0 bar. For comparison, the mole fraction of ethyl acetate in a bulk phase at the same temperature and pressure is included.

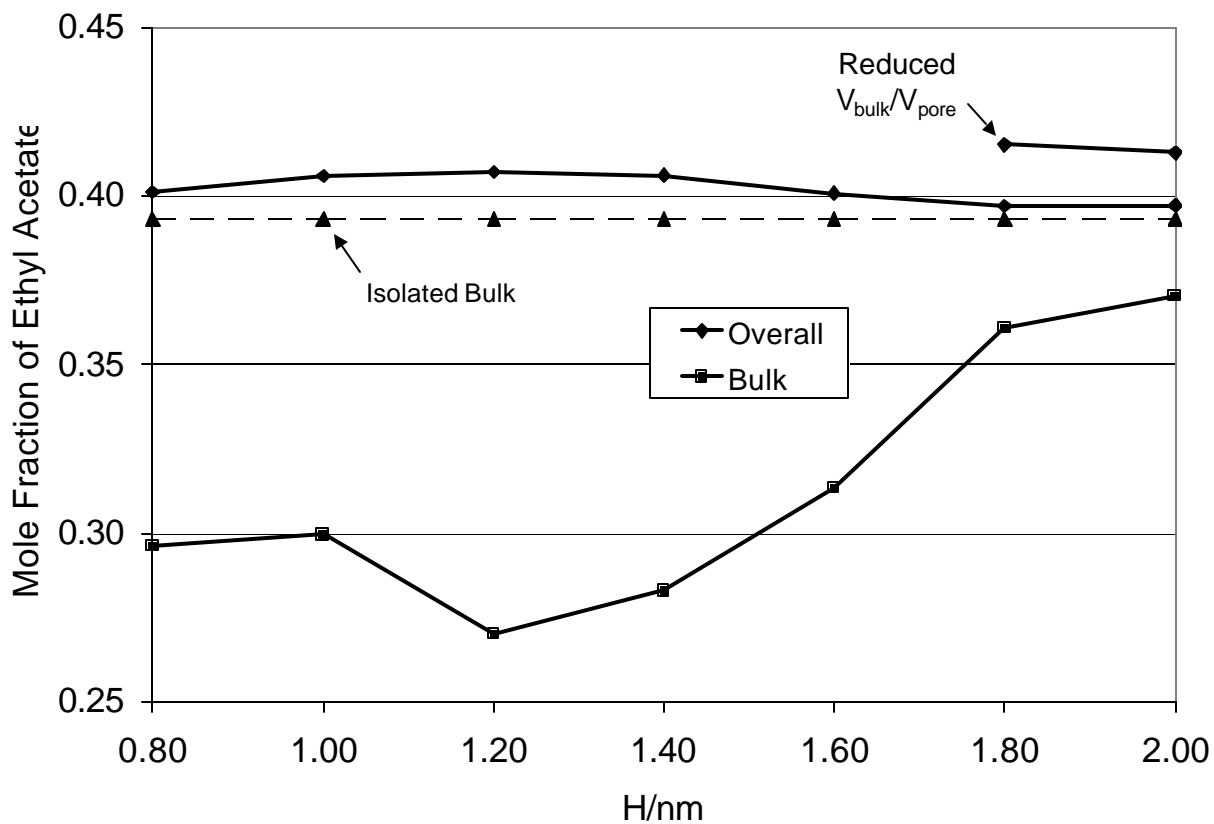


Figure 4.8 Mole fraction of ethyl acetate corresponding to the two-phase RxMC simulations in the unactivated carbon slit-pore. The temperature is 523.15 K and the gas phase pressure is 1.0 bar. For comparison, the mole fraction of ethyl acetate in an isolated bulk gas is shown.

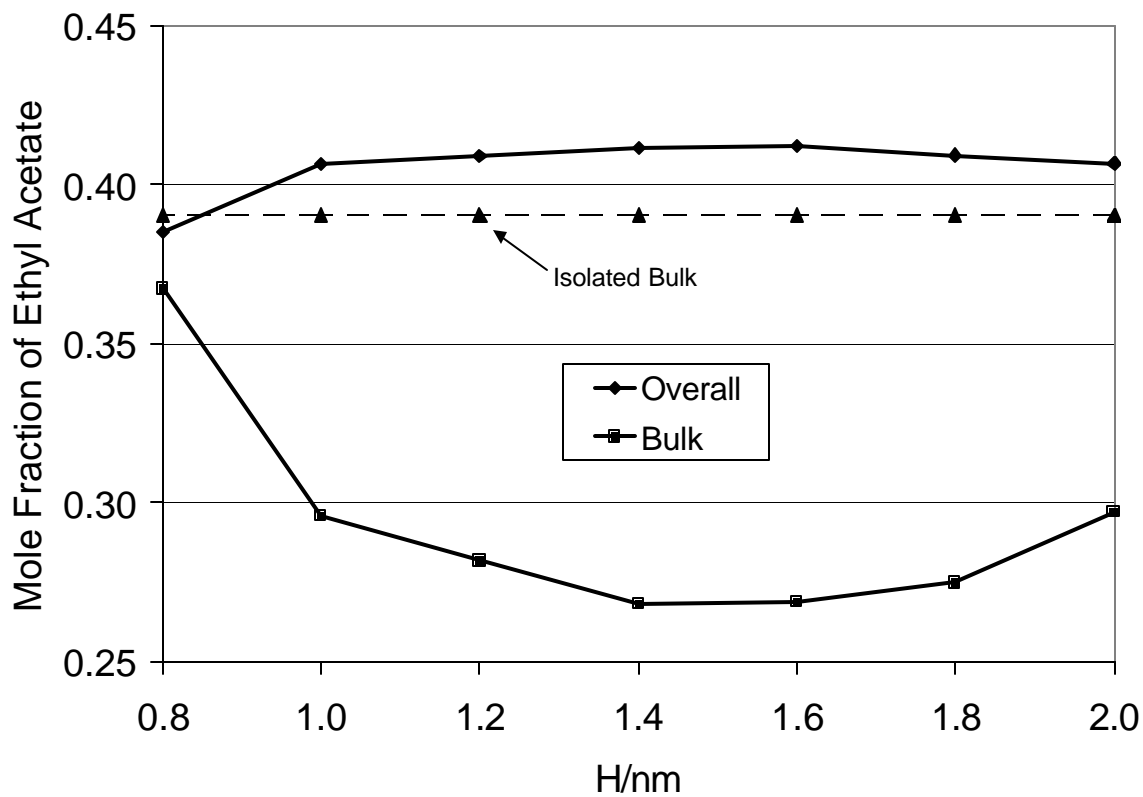


Figure 4.9 Mole fraction of ethyl acetate corresponding to the two-phase RxMC simulations in the activated carbon slit-pore (1.82 sites/nm^2). The temperature is 523.15 K and the gas phase pressure is 1.0 bar. For comparison, the mole fraction of ethyl acetate in an isolated bulk gas is shown.

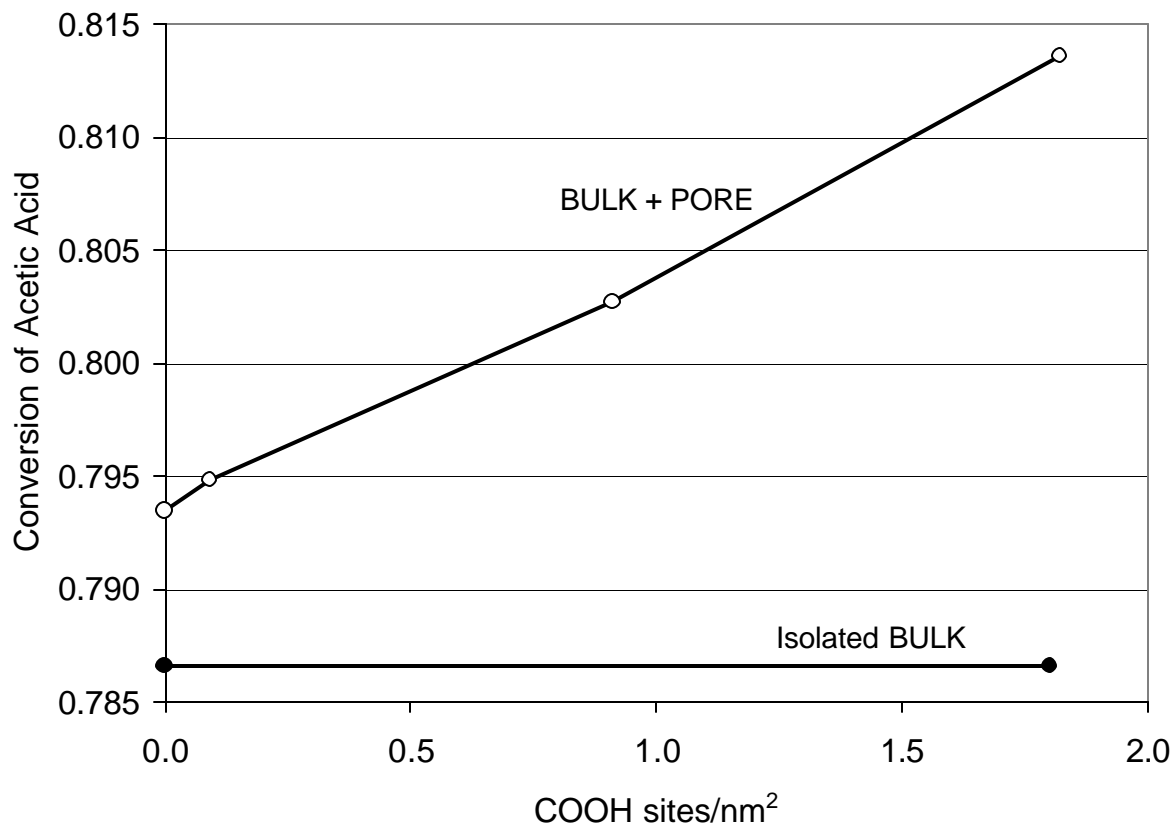


Figure 4.10 Total conversion (bulk + pore) of acetic acid to ethyl acetate with a pore of width $H=2.00$ nm. The system temperature is 523.15 K and the bulk phase pressure is 1.00 bar.

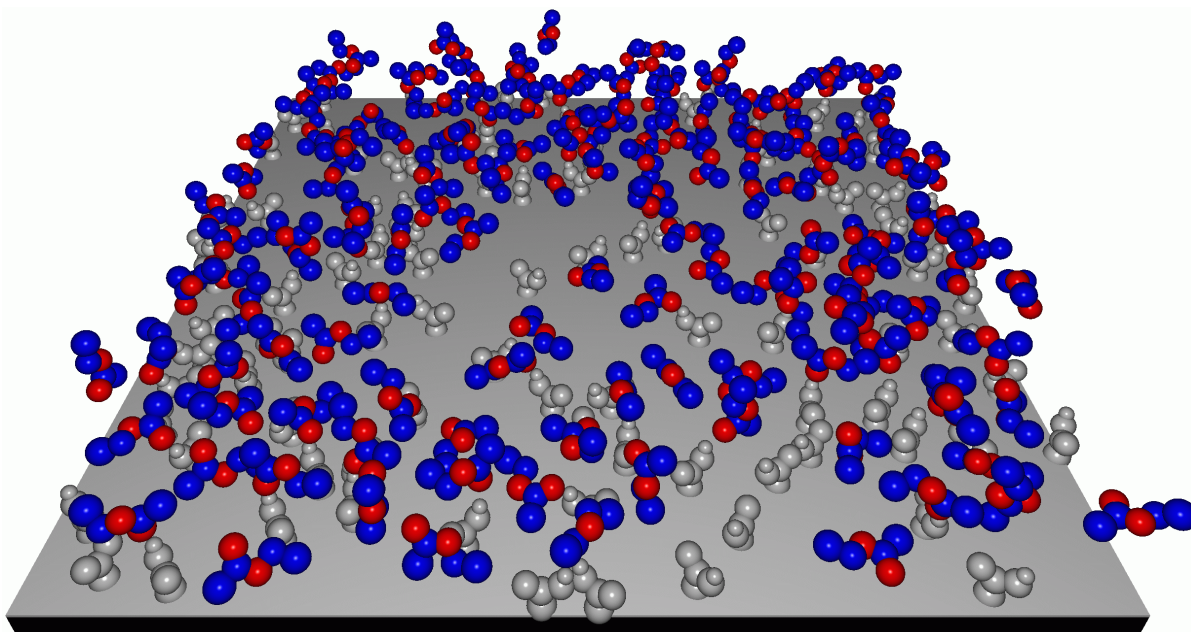


Figure 4.11 Simulation snapshot of the esterification reaction in an activated carbon pore of width $H=2.0$ nm. The carboxyl site density is 1.82 sites/nm² and the temperature is 523.15 K. The top half of the pore is removed and only ethyl acetate molecules are shown for clarity. The carboxyl sites are shown in gray, and the oxygen atoms within ethyl acetate are shown in red.

CHAPTER 5

Effect of Confinement on Reaction Kinetics

5.1 Introduction

An important class of catalysts in use today is *supported catalysts*, in which the catalytic or active material is dispersed over a less active support material. Typically, the support material is highly porous, with pore widths of the order of a few nanometers, and is characterized by a high surface area. Confinement effects in these porous materials are known to be large for both phase [1] and chemical [2,3] equilibria. In the latter case, increases in yield due to confinement in activated carbon fibers of up to two orders of magnitude have been predicted from molecular simulations [2] and have also been found in experiments [4]. Likewise, we expect that reaction rates in the porous medium may differ substantially from those in the bulk phase due to increased density of the pore phase, selective adsorption of some constituents, preferred molecular orientation near the walls, changes in diffusion rates, shape-selectivity of the transition state, etc. Surprisingly, there seems to have been little, if any, fundamental investigation of these effects. An understanding of these effects is needed for the design of appropriate catalysts for a given reaction.

Almost all fundamental research on catalysis has focused on the interaction of the reactants with the catalyst surface. For the present discussion, it is convenient to refer to such interactions as "chemical" ones, by which we mean that they are sufficiently strong to significantly change the

electronic structure of the atoms and molecules involved. These types of interactions are best studied with quantum mechanical techniques, such as *ab initio* methods or density functional theory (DFT). However, in supported catalysis we may anticipate a further significant effect of confinement on the reaction rate due to the finite size and reduced dimensionality of the adsorbed phase, and to the strong interactions of the reacting species with the pore walls. We refer to these latter interactions (repulsion, dispersion, electrostatic, etc.) as "physical" forces to distinguish them from the chemical interactions with the catalyst. While the values of these forces can be found using quantum mechanical simulations, they can be approximated accurately using classical simulation techniques, as will be demonstrated in this Chapter.

Gaining an understanding of confinement effects on reaction kinetics from experiments is very difficult because of problems associated with observing the confined phase, characterization of the pore structure, and separation of the "physical" effects of confinement from "chemical" interactions with the catalyst. However, molecular simulation is an appropriate tool for such investigations because these problems do not arise, and system parameters can be precisely controlled and manipulated. Reaction rate constants can be estimated using either classical or quantum mechanical calculations. While quantum mechanical approaches are the most accurate, the computational demands of these methods limit the size of the system to a small number of molecules (typically < 32 molecules), too small to study confinement effects. With a few exceptions, such approaches usually neglect intermolecular force contributions or include these forces in an approximate way. An overview of the current methods available for predicting reaction rate constants is presented in

Chapter 1, with the approaches segregated according to the level of approximation (continuum, classical, or quantum mechanical).

In this Chapter we present a new classical-level approach to the prediction of rate constants that allows us to address the influence of porous confinement or other highly non-ideal environments on reaction rates. We develop this method within the framework of transition-state theory [5] for calculating bimolecular rate constants under a wide range of conditions. The method is based on the quasi-equilibrium hypothesis, which assumes that the reactants (A) and the transition state (TS) complex are in direct chemical equilibrium: $2A \leftrightarrow TS \rightarrow B$. With this assumption, the Reactive Monte Carlo (RxMC) method [6] is used to determine the concentration of the activated species, which can then be directly related to the bimolecular rate constant. A requirement of the simulations is that the structure of the transition state and the activation energy barrier must be determined *a priori* from quantum mechanical and electronic structure methods. Once this is determined, any geometric or energetic distortion of the transition state from neighboring molecules or from the pore walls is ignored, although these details can be calculated separately and incorporated if found to be significant. Furthermore, the method currently neglects dynamic collision effects, which can be an important consideration when refining the value of the reaction rate constant [7]. The methodology is computationally efficient so that large systems can be simulated, on the order of 10^6 atoms. Most importantly, effects on the reaction rates caused by non-ideal environments (high pressures, various solvent types, solid surfaces, or confinement in porous solids, etc.) are implicit to the methodology. Therefore, corrections for non-ideal behavior of reacting systems made to standard transition-state

theory expressions (*e.g.*, by estimating free energies of solvation or by calculating activity coefficients of the reacting species and the transition state) are not required.

An outline and validation of the transition-state theory-Reactive Monte Carlo methodology (TS-RxMC) are given in Sections 5.2 and 5.3, respectively. To demonstrate the flexibility of this technique, an application of the method to the decomposition reaction, $2\text{HI} \rightarrow \text{H}_2 + \text{I}_2$, in various non-ideal environments is presented in Section 5.4. Finally, in Section 5.5 we discuss some further applications and possible future improvements to the current method.

5.2. Methodology

5.2.1 Transition-State Theory Background

The foundations of transition-state theory (TST) and the fundamental assumptions of the method were developed in the 1930's by Eyring [5] and Evans and Polanyi [8]. The application of transition-state theory to bimolecular reactions generally hinges on two conditions:

1. The free energy activation barrier (E^*) to form the transition state must be high compared to $k_B T$, where T is the temperature of the reacting system and k_B is the Boltzmann constant.

and

2. The coupling of the system to the reaction coordinate must be strong enough to dissipate roughly $k_B T$ energy from the product in time comparable to the velocity of the reaction coordinate [9].

The repercussions of Condition (1) above have been examined with the following conclusions [10].

If the ratio of the activation energy to $k_B T$ is greater than about 5, *i.e.*, $E^* \geq 5k_B T$, then the quasi-equilibrium hypothesis (chemical equilibrium between the reactants and the transition state) is a good approximation. Furthermore, this approximation will become exact in the limit of zero temperature.

At lower temperatures quantum mechanical effects can become significant due to tunneling of reactants through the activation barrier (which invariably increases the observed rate constant).

However, if tunneling effects are neglected, TST gives the lower bound to the predicted reaction rate constant.

Another challenge encountered when applying TST to predict reaction rate constants is that of accounting for the re-crossing of the activation barrier by the products to regenerate reactants.

Condition (2) above minimizes this possibility. Product re-crossing occurs because of a low activation barrier or by dynamic collisions of solvent molecules with product molecules and leads to a decrease in the reaction rate. The reaction considered in this chapter, $\text{HI} + \text{HI} \leftrightarrow (\text{HI})_2^\ddagger \rightarrow \text{H}_2 + \text{I}_2$, is carried out at temperatures high enough to avoid significant quantum tunneling effects, yet low enough ($E^* \sim 37k_B T$) so that Condition (1) is not violated.

Further complications of applying TST involve defining the relative positions of the dividing surface (the saddle point of the potential energy surface) and calculating the activation energy barrier (E^*). Knowledge of the position of the dividing surface for a chemical reaction - which typically lies close to the free energy activation barrier of the transition state - is crucial for accurate calculations. Typically, the dividing surface is chosen to minimize the value of the TST rate constant, and therefore it corresponds to the maximum in the free energy along the path between reactants and products. Finally, calculating properties of the transition state are difficult because the transition state is never seen in experiment. Calculations of the activation energy, geometry and vibrational energies of the transition state can all be performed with either *ab initio* or DFT calculations.

5.2.2 Transition-State Theory: Fundamental Expressions

The fundamental finding of Eyring's original work [5] is the following expression for the standard state rate constant,

$$k^\circ = \mathbf{k} \frac{k_B T}{h} e^{-\Delta G^\circ/RT} = \mathbf{k} \frac{k_B T}{h} \frac{q^\ddagger}{q_1 \cdots q_n} V^{(n-1)} e^{-E^*/RT} \quad (5.1)$$

where ΔG° is the standard Gibbs free energy of formation, h is the Planck constant and R is the universal gas constant. This expression relates the standard state rate constant, k° , to the change in the Gibbs free energy required to form the transition state. For gas reactions, the standard state is taken to be the pure ideal gas at unit pressure (1 bar) for each reactant and the transition state. The

symbol k represents corrections due to any re-crossing of the products through the dividing surface and has a value between 0 and 1. The value of k depends on the specific reaction and the conditions of the system; $k=1$ yields the upper bound of the reaction rate predicted by TST, *i.e.*, when re-crossing effects are neglected.

The expression for the rate constant can also be formulated in terms of molecular partition functions, also shown in Eq. (5.1), where E^* is the activation energy barrier, q^\ddagger is the transition state partition function and $q_1\dots q_n$ are the reactant partition functions, and V is the system volume. While Eq. (5.1) is convenient for predicting ideal gas kinetics, it cannot account for high-pressure effects, solvation effects, and general non-idealities contributing to the rates of chemical reactions. Despite a lengthy history of applying TST to condensed-phase systems, the accurate prediction of rate constants in condensed phases still presents a formidable challenge. The difficulty results from the complexity of including the non-ideal nature of the system into the rate constant calculation, as well as the challenge of accurately evaluating the interaction energies.

5.2.3 Derivation of the TS-RxMC Working Expression

The simulation method presented in this work is based on an equilibrium solvation approach together with fundamental aspects of equilibrium thermodynamics; any effects due to solvent dynamics are neglected. The derivation of the working expression for the TS-RxMC method begins with the seminal work of Eyring, reflected in Eq. (5.1). This general TST expression is recast into a form more appropriate for combination with the Reactive Monte Carlo simulation method.

The exponential term of Eq. (5.1) can be rewritten in terms of an equilibrium constant (K_a^\ddagger) based on the quasi-equilibrium between the reactants and the transition state. The standard Gibbs free energy change is related to the equilibrium constant by Eq. (5.2).

$$\Delta G^\circ = -RT \ln K_a^\ddagger \quad (5.2)$$

K_a^\ddagger in Eq. (5.2) is defined as

$$K_a^\ddagger = \frac{a^\ddagger}{a_1 \cdots a_n} = \frac{\mathbf{g}^\ddagger c^\ddagger}{(\mathbf{g}_1 \cdots \mathbf{g}_n)(c_1 \cdots c_n)} \quad (5.3)$$

where a is the activity, \mathbf{g} is the activity coefficient, c is the molar concentration, and ‡ denotes the transition state while 1...n denotes the reactant species, where n=1 for unimolecular reactions and n=2 for bimolecular reactions. Substituting Eqs. (5.2) and (5.3) into Eq. (5.1), the rate constant can be re-written as

$$k^\circ = \mathbf{k} \frac{k_B T}{h} K_a^\ddagger \quad (5.4)$$

If the reaction is modeled as an ideal gas reaction at unit pressure the expression for the rate constant would then reduce to Eq. (5.5), where x_i is the mole fraction of component "i" in the fluid mixture.

$$k^\circ = \mathbf{k} \frac{k_B T}{h} \frac{x^\ddagger}{x_1 \cdots x_n} \quad (5.5)$$

The equilibrium constant for a non-ideal gas reaction or for a reaction in solution is not as easily obtained. The observed rate constant, k_{obs} , as defined by Eyring [5], is related to the rate constant at standard state conditions, k° , through the following relation:

$$k^\circ = \mathbf{k} \frac{k_B T}{h} \frac{c^\ddagger}{c_1 \cdots c_n} \frac{\mathbf{g}^\ddagger}{\mathbf{g}_1 \cdots \mathbf{g}_n} = k_{obs} \frac{\mathbf{g}^\ddagger}{\mathbf{g}_1 \cdots \mathbf{g}_n} \quad (5.6)$$

A common approach to dealing with reactions in condensed phases is to calculate the reaction rate at the standard state (k°) and then estimate reactant and transition state activity coefficients. By rearrangement of Eq. (5.6), the observed reaction rate constant (k_{obs}) can then be calculated. The main limitation of this approach is that the activity coefficients of the reactants and the transition state must be determined. While this calculation may be straightforward for reactions in homogeneous environments, it is not possible to make accurate calculations of activity coefficients in the

heterogeneous environments of many solvent types or porous solids. Alternatively, the free energy of solvation of the reactants and the transition state can be approximated in separate simulations and then added to the ideal gas free energy of activation. In this Chapter, we present a method for avoiding the need to calculate activity coefficients or the free energy of solvation. We do this in a single simulation by directly evaluating the equilibrium between the reactants and transition state by use of the RxMC method.

5.2.4 Reactive Monte Carlo Method

Reactive Monte Carlo (RxMC) is a simulation technique for calculating the properties of chemically reactive systems. It can be used to predict equilibrium concentrations of reaction components in one- or two-phase systems [2,3,6,11-17] by performing Monte Carlo sampling of forward and reverse reaction steps of a predefined reaction. Neither the values nor the calculation of the chemical potentials or chemical potential differences are required. The RxMC method is formulated in terms of chemical potentials rather than activities, but the quantities are interchangeable by the relation $a_i \equiv \exp[(\mathbf{m}_i - \mathbf{m}_i^\circ) / RT]$, where \mathbf{m}_i is the chemical potential of species i and \mathbf{m}_i° is the chemical potential of species i in the standard state. In addition, the RxMC method does not constrain the values of the chemical potentials beyond the requirement of chemical equilibrium, which is implicit to TST. This results in a reacting system that obeys:

$$\left(\sum_i n_i \mathbf{m}_i \right)_{\text{products}} = \left(\sum_i n_i \mathbf{m}_i \right)_{\text{reactants}} \quad (5.7)$$

where n_i is the stoichiometric coefficient of species i .

For the purposes of combining transition-state theory formalism with the RxMC method, k_{obs} from Eq. (5.6) is written in terms of the concentrations as

$$k_{obs} = k^\circ \frac{g_1 \cdots g_n}{g^\ddagger} = \mathbf{k} \frac{k_B T}{h} \frac{c^\ddagger}{c_1 \cdots c_n} \quad . \quad (5.8)$$

RxMC simulations can be performed to determine the equilibrium concentrations of the reactants $c_1 \cdots c_n$ and the transition state c^\ddagger . As evident from Eq. (5.8), the need to calculate the activity coefficients of reacting components has been eliminated. Deviations of the reacting medium from ideality which influence the reaction rate are manifested in the equilibrium concentrations within the fluid mixture. These concentrations are influenced by the non-ideal interactions prescribed in the simulation, for example, by imposing a high pressure on the system or by including pore walls in the simulation cell.

5.2.5 Outline of Methodology

An algorithm for applying the transition-state theory-Reactive Monte Carlo method to the calculation of rate constants is as follows:

Step 1: For the chosen reaction, the following information is required:

- (A) Intermolecular potentials for the reactants and the transition state
- (B) Molecular partition functions for the reactants and the transition state
- (C) Value of the activation energy barrier (E^*) required to create a transition state

The molecular partition functions and model parameters for the reactants are readily available and can be taken from standard sources [18-20]. However, knowledge of the transition state geometry and the activation energy barrier must be determined from quantum mechanical calculations *a priori*. Fortunately, recent research efforts have provided potential energy surfaces and transition states for a plethora of reactions [21]. After the transition state structure and partition functions (rotational, vibrational, electronic) have been determined, intermolecular potentials for the transition state can then be constructed by an amalgam of standardized atomic potentials [18-20].

Step 2: Perform a Reactive Monte Carlo simulation to calculate the equilibrium concentrations of the reactants and the transition state. The simulations involve the following trial moves, with the appropriate transition probability [6] applied to each. The transition probabilities for these moves are similar to the ones prescribed in the previous chapters.

- (A) **Move/Reorientation:** a random change in the position or orientation of a randomly selected molecule

- (B) **Forward Reaction Step:** $2\text{HI} \rightarrow (\text{HI})_2^\ddagger$, reactant molecules are changed to product molecules
- (C) **Reverse Reaction Step:** $(\text{HI})_2^\ddagger \rightarrow 2\text{HI}$, product molecules are changed to reactant molecules
- (D) **Volume Change:** a random change in the volume that maintains the imposed pressure (constant pressure simulations only)

For application of the RxMC scheme to the calculation of rate constants, the term "product molecules" refers to the transition state (TS) molecule. If the probability of forming the transition state (*i.e.*, move (B)) is found to be extremely low due to the activation barrier (as it should be), the simulations need to be biased in order to accumulate statistically-reliable Monte Carlo averages. The biasing technique is described in detail in the next section.

Step 3: Substitute the accumulated averages of the reactants and transition state concentrations into Eq. (5.8), and calculate the observed reaction rate constant. The rate constant must be appropriately corrected for any biasing introduced in Step 2.

5.2.6 Biased TS-RxMC Simulations

Since one of the requirements in the TST formalism is that the activation barrier be large ($E^* \geq 5k_B T$), the acceptance probability of creating the TS (defined as a forward reaction step) in the RxMC scheme will be prohibitively low under moderate thermodynamic conditions. Thus,

accurately measuring the concentration of the TS will be difficult within simulations of reasonable length. This is apparent in the acceptance criterion expression for the forward reaction:

$$P \propto \exp\left(\frac{-E^*}{k_B T}\right) \quad (5.9)$$

where P is the probability of the forward reaction occurring and E^* is the activation energy barrier. To increase the probability of forming the transition state, the activation energy barrier can be carefully adjusted. The adjustment to the activation energy barrier can be included directly into the acceptance criteria given in Eq. (5.9) as:

$$P_{bias} \propto \exp\left(\frac{-E^*}{k_B T}\right) \exp\left(\frac{E_{adj}}{k_B T}\right) \quad (5.10)$$

It is obvious from Eq. (5.10) that a positive value of E_{adj} will increase the probability of the forward reaction step. After the equilibrium concentrations of the reactants and the transition state have been determined from the RxMC simulations, corrections must be made in the final calculation of the reaction rate constant. The correction can be made directly into the expression for k_{obs} given in Eq. (5.10) as:

$$k_{obs} = \mathbf{k} \frac{k_B T}{h} \times \frac{c^\ddagger}{c_1 \cdots c_n} \times \exp\left(\frac{-E_{adj}}{RT}\right) \quad (5.11)$$

Note that the sign preceding the E_{adj} term is now negative. Although the choice of E_{adj} is somewhat arbitrary, its upper and lower limits nevertheless should be sensibly bound. The calculated transition state concentration in a reacting mixture is typically extremely small. This feature should be preserved in the simulation so that the properties of the fluid are not altered by the presence of TS molecules. In the current simulations, E_{adj} has been altered so that the molar concentration of the TS is less than 1% of the fluid concentration. Thorough tests have been performed to show that with such an E_{adj} value the reaction rate constant is independent of the amount of bias introduced in a simulation. These results are shown in Section 5.3.

5.3 Verification of the TS-RxMC Method

The methodology presented in this work is validated from two perspectives. First, the method is shown to accurately predict experimentally measured reaction rates, within the limits of classical behavior. And second, the method is demonstrated to be thermodynamically self-consistent. These verification tests are applied to the decomposition reaction: $2\text{HI} \rightarrow \text{H}_2 + \text{I}_2$. Extensive experimental [22] and theoretical [23] investigations have been carried out for the HI decomposition reaction. Furthermore, the reaction is known to have no complicating side reactions, and the activation barrier for the reaction, ~ 42 kcal/mol [7], is much greater than $5k_B T$ at moderate conditions. Finally,

critical to the validation of the methodology presented here, this reaction exhibits a significant change in the reaction rate as the pressure is varied.

5.3.1 Prediction of Experimentally Measured Reaction Rates

The constant-pressure Gibbs ensemble method [24,25] (described in previous Chapters) is used in conjunction with RxMC to find the equilibrium composition for the reaction, $2\text{HI} \leftrightarrow (\text{HI})_2^\ddagger$, where $(\text{HI})_2^\ddagger$ is the transition state. The HI molecule and $(\text{HI})_2^\ddagger$ are modeled as single-site Lennard-Jones (LJ) spheres, each with an ideal dipole. The intermolecular parameters are summarized in Table 5.1, where m is the ideal dipole assigned to each molecule [26]. The intermolecular potential for the transition state has been approximated by assuming the transition state geometry shown in Figure 5.1 [23]. The trapezoidal geometry of the $(\text{HI})_2^\ddagger$ complex used in the current simulations has been confirmed with semiempirical valence-bond calculations [27], but it is noted that a collinear transition state structure has also been suggested [28].

Table 5.1 Intermolecular potential parameters for the $2\text{HI} \leftrightarrow (\text{HI})_2^\ddagger \rightarrow \text{H}_2 + \text{I}_2$ reacting system.

Molecule	s (nm)	e/k_b (K)	$m/(4\pi\epsilon_0\epsilon\sigma^3)^{0.5}$	Reference
HI	0.413	313	0.0205	[23]
$(\text{HI})_2^\ddagger$	0.5169	513	0.0172	[23]
H_2	0.2928	37	0.0	[19]
I_2	0.4982	550	0.0	[19]

The TS-RxMC simulations for the HI decomposition reaction were typically equilibrated for 1×10^6 moves and averages were taken over 4×10^6 moves. The LJ interaction potential was cut off after

2.0 nm and the electrostatic potential cutoff was 4.0 nm, without applying long-range corrections. The standard Lorentz-Berthelot mixing rules were used for the interaction between unlike species: $\sigma_{ij}=0.5(\sigma_i+\sigma_j)$ and $\epsilon_{ij}=(\epsilon_i\epsilon_j)^{0.5}$. The simulation box contained a total of approximately 2,000 molecules. For the two-phase (bulk + pore) simulations, presented in Section 5.4, the same potentials are used, but the system size was increased. The pore size was adjusted so that there was an even distribution of molecules between the bulk and the pore phases.

The TS-RxMC method was used to calculate the rate constant of the hydrogen iodide decomposition reaction in the bulk phase over a range of pressures from 1 to 300 bar. The concentrations determined in the simulations were used to calculate the rate constant at a specified pressure relative to the standard state rate constant (1 bar pressure). The TS-RxMC data are plotted in Figs. 5.2 and 5.3. For comparison purposes, the data are presented in the same manner as in the original work of Kistiakowsky [22]. Figure 5.2 corresponds to a temperature of 573.15 K, and Fig. 5.3 to a temperature of 594.55 K, and the simulation pressures corresponding to several different HI concentrations are shown. Quantitative agreement with the experimental data at low HI concentrations is inconclusive due to considerable scatter of the experimental data. However, excellent quantitative agreement between the TS-RxMC simulations and the experimental data is found at moderate to high HI concentrations. More importantly, the TS-RxMC simulations are able to accurately capture the overall dependence of the rate constant on the HI concentration, including the more than 50 fold increase in (k/k_0) at the highest pressure considered in the simulations (300 bar).

A theoretical treatment of the HI decomposition reaction has been carried out previously. Based on an application of the Brønsted-Bjerrum equation to non-ideal gas mixtures [23], the rate constant can be expressed as

$$k_{obs} = k^o \frac{f_{HI}^2 Z}{f_{(HI)_2^\ddagger}} \quad (5.12)$$

where f_{HI} and $f_{(HI)_2^\ddagger}$ are the fugacity coefficients of the reactant and the transition state, respectively, and Z is the compressibility factor of the mixture. Fugacity coefficients were evaluated from the second and third virial coefficients [29]. A comparison of the calculations of Eckert and Boudart with the TS-RxMC simulation results is shown in Fig. 5.4. Excellent agreement is found for both temperatures at low concentrations, while at higher concentrations Eq. (5.12) slightly over predicts the relative reaction rate constants.

Kistiakowsky provided an interpretation of the dependence of the HI decomposition rate on the pressure from arguments based on the van der Waals equation of state. Kistiakowsky reasoned that since the rate increased faster than the square of the system density, then the increase must be due to the non-ideality of the gas mixture [22]. From the TS-RxMC perspective, this interpretation is encouraging because it implies that the simulation method is capturing essential features of non-ideal reaction kinetics.

The implementation of the TS-RxMC method is justified when theoretical expressions, such as Eq. (5.12), for predicting non-ideal phenomena are not available. For example, the prediction of non-ideal reaction behavior in disordered porous solids is especially critical to the design of support catalysts. However, simple expressions analogous to Eq. (5.12) are not presently available for such systems.

5.3.2 Test of TS-RxMC Self-Consistency

Next we demonstrate that the TS-RxMC methodology is thermodynamically self-consistent. By definition, at equilibrium, the forward and reverse rates should be equal. Also, by definition, the equilibrium constant can be determined from the ratio of the rate constants. As a test of the self-consistency of the TS-RxMC method, the forward and reverse rate constants were calculated at the equilibrium condition of the HI decomposition reaction. We have assumed that the reverse reaction is bimolecular and that the transition state is identical to that of the forward reaction. With these assumptions, it should be possible to reproduce the concentration equilibrium constant:

$$K_c \equiv \frac{k_+}{k_-} = \frac{[(\text{HI})_2^\ddagger]/[\text{HI}]^2}{[(\text{HI})_2^\ddagger]/\{[\text{H}_2][\text{I}_2]\}} = \frac{[\text{H}_2][\text{I}_2]}{[\text{HI}]^2} \quad (5.13)$$

where the brackets indicate the concentration of each species measured during the equilibrium RxMC simulations, K_c is the concentration equilibrium constant, and the k_+ and k_- are the forward and reverse rate constants measured in the TS-RxMC simulations.

The first step was to use the original version of RxMC to predict the equilibrium composition of the complete hydrogen iodide decomposition reaction, $2\text{HI} \leftrightarrow \text{H}_2 + \text{I}_2$, over a range of pressures. As this reaction is a mole-conserving reaction, there was only a small variation of the equilibrium composition with pressure. Next, TS-RxMC simulations in the forward direction were performed for fluid compositions equal to the equilibrium RxMC simulations, approximately 95% HI, 2.5% H_2 , 2.5% I_2 , and <1% TS. The LJ parameters for the H_2 and I_2 intermolecular potential are shown in Table 5.1. These simulations were carried out at a temperature of 573.15 K, over the pressure range of 1 to 250 bar, and the corresponding forward rate constant was measured in each simulation. Analogous simulations were performed for the reverse reaction, and the reverse reaction rate constant at each pressure was measured. The equilibrium constant of the hydrogen iodide decomposition reaction is plotted in Figure 5.5 over the pressure range studied. The results in Figure 5.5 are taken as an average of 2 runs of 5×10^6 MC steps at each pressure. There is excellent agreement in the value of the equilibrium constant between the RxMC simulations and the ratio of the forward and reverse TS-RxMC simulations, as all points lie within one standard deviation of the mean value. This exercise demonstrates the thermodynamic consistency of the TS-RxMC method.

5.3.3 Biased TS-RxMC Simulations

To determine the influence of the biasing on the rate constant calculation, tests have been performed on the HI decomposition reaction and on the reaction $\text{H}_2 + \text{D} \leftrightarrow \text{H}_2\text{D} \rightarrow \text{HD} + \text{H}$. The partition functions [30] and the molecular model parameters [31] for the H_2 exchange reaction were taken from standard sources. The results of these tests are shown in Figures 5.6 and 5.7. The simulated reaction rate constant relative to the standard state reaction rate constant is plotted in Figs. 5.6 and 5.7 versus the amount of biasing introduced in the simulation. The standard state rate constant was determined directly from Eq. (5.1). Error bars in Fig. 5.6 represent one standard deviation of the mean for each data point. Both sets of simulations were performed at a pressure of 1 bar, and the temperatures in the simulations were 450 K and 573.15 K for the H_2 exchange reaction and the HI decomposition reaction, respectively. In order to calculate the standard deviation and average values, five separate simulations were performed corresponding to each value of E_{adj} , with 4×10^6 Monte Carlo steps in each simulation.

The studies show that the average values of the reaction rate constants are independent of the choice of E_{adj} , while the statistical uncertainty is found to improve greatly by increasing the value of E_{adj} . It is important to reiterate that the value of E_{adj} be reasonably bound. If the value is too high, the mole fraction of TS becomes too large. Such large values are unrealistic and could affect the properties of the fluid. Therefore, we have kept the value of E_{adj} bound so that the TS mole fraction is never greater than 1%. An initial series of short simulations were performed to determine the value of E_{adj} needed to maintain a composition of less than 1% TS for each simulation run.

5.4 Effects of Strong Intermolecular Forces and Confinement

TS-RxMC simulations of the HI decomposition reaction were performed in several different inert solvents as well as in microporous carbons. These environments can have significant effects on the reaction kinetics. If the transition state interacts more favorably with the surrounding solvent than the reactants, the reaction rate is expected to increase. However, if the transition state complex does not interact favorably with the solvent molecules, the reaction rate is expected to decrease. Analogous conjectures based on the interaction between the transition state and the pore wall can be made for reactions occurring in porous materials. Furthermore, reactions with a negative value for the activation volume should be expected to exhibit rate increases with increasing pressure or density.

5.4.1 Solvation Effects

TS-RxMC simulations of the HI decomposition reaction ($2\text{HI} \leftrightarrow (\text{HI})_2^\ddagger$) have been performed in a variety of different solvents: N_2 , CCl_4 , CH_4 , CO_2 and NH_3 over a wide range of pressures (1-250 bar). The solvents were intentionally chosen to explore a wide range of solvation effects, including non-polar and polar fluids. The solvent molecules were modeled using site-site Lennard-Jones potentials, with point charges distributed on those molecules in which electrostatic forces contribute significantly to the overall interaction energy. A summary of the molecular interaction parameters for the solvents used in the simulations is given in Table 5.2.

Table 5.2 Solvent parameters corresponding to a site-site LJ plus point charge potential. The column "*bl*" refers to the distance of an interaction site from the molecule center. All of the multi-site molecules were linear except NH₃, which has a HNH bond angle of 110.9°.

Molecule	Site	<i>bl</i> (nm)	σ (nm)	ϵ/k_b (K)	q (e)	Reference
CO ₂	1	0.1149	0.3033	80.507	-0.3256	[32]
	2	0.0	0.2757	28.129	+0.6512	
	3	0.1149	0.3033	80.507	-0.3256	
N ₂	1	0.055	0.332	36.4	-0.40505	[33]
	2	0.0	0.0	0.0	+0.8101	
	3	0.055	0.332	36.4	-0.40505	
NH ₃	1	0.0	0.332	36.4	0.0	[34]
	2	0.10124	0.225	21.1	+0.485	
	3	0.10124	0.225	21.1	+0.485	
	4	0.10124	0.225	21.1	+0.485	
	5	0.0156	0.0	0.0	-1.455	
CH ₄	1	0.0	0.381	148.1	0.0	[35]
CCl ₄	1	0.0	0.588	323	0.0	[19]

The TS-RxMC predictions of the reaction rate in different inert solvents are shown in Figure 5.8.

The activation energy barrier of the transition state was assumed to remain unaffected by the different solvents. Likewise, it is assumed that the solvent does not alter the structure of either the reactants or the transition state. The presence of the solvents in the reacting mixture had only a moderate effect on the reaction rate compared to the pure HI fluid, with the largest influence found at the higher pressures. Furthermore, the reaction showed negative effects in three of the five solvents, *i.e.*, the reaction rate was retarded (up to a maximum of about 25%) when N₂, CH₄, and NH₃ were present in the reacting mixture. The solvents which accelerated the reaction rate (CO₂ and CCl₄) were found to be at a higher density than the solvents that decreased the reaction rate (N₂, CH₄, and NH₃), given the same pressure. Therefore, the density is believed to be the main factor influencing the reaction rate constants in the different solvents studied.

The modest effect on the rate when the solvent is present can be attributed to the similarity of the structures and intermolecular potentials of the reactant and transition state molecules. Since HI and $(\text{HI})_2^\ddagger$ are quite similar in molecular nature, solvent molecules have a similar interaction with each species. It is expected that the surrounding solvent would have a more dramatic effect on the reaction rate in cases where the nature of the reactants and the transition state are very different. For example, if two nonpolar molecules react and pass through a transition state that has a large dipole, one would expect that such a reaction would be kinetically favored in a polar solvent.

5.4.2 Effect of Confinement in Carbon Pores

A two-phase reacting system consisting of a pore phase and a bulk phase at constant pressure [24,25] was used to study the kinetics of hydrogen iodide decomposition in carbon pores [2]. Standard RxMC trial moves (particle displacements and rotations, forward reactions and reverse reactions) are performed in each phase. Equilibria between the pore and bulk phases is established through particle exchanges of the reactant and transition state molecules between the two phases. The particle exchanges ensure that the chemical potential of each species is equal in both phases.

The two-phase TS-RxMC method was used to study the HI decomposition reaction confined in a microporous carbon and in carbon nanotubes. The microporous carbon was modeled as a slit-like pore with two infinite parallel walls in the x - y plane separated by a distance H in the z -direction. Each of the two walls is taken to be the basal plane of a graphite surface comprised of Lennard-

Jones atoms. The 10-4-3 Steele potential [35] was used to describe the interaction energy between a fluid particle and the pore wall. The usual potential parameters were taken for the carbon atoms [35], and the Lorentz-Berthelot combining rules were used to estimate unlike-pair potential parameters between the carbon walls and the reacting adsorbate molecules. TS-RxMC simulations were performed at several different pore widths ranging from 1.0 nm to 1.75 nm. The width of the pore is defined as the distance between the plane through the centers of the carbon atoms that form the surface layers on opposing walls.

The effect of the pore width on the reaction rate constant is shown in Figure 5.9 for pressures up to 200 bar and a temperature of 573.15 K. The pressures correspond to the bulk phase pressure in equilibrium with the pore. For comparison, the reaction rate dependence on the pressure for the reaction in the pure bulk HI fluid is also shown. The effects on the reaction are much more dramatic than the solvation effects (Fig. 5.8). The reaction rate was found to increase by a factor of 5 at a pressure of 1 bar and a factor of 13 at a pressure of 200 bar in the 1.00 nm pore, as compared to the bulk fluid at the same temperature and pressure. A physical interpretation of the appreciable acceleration of the reaction rate in the carbon pores is based on the enhanced energetics that the reacting fluid mixture experiences. In general, a confined fluid mixture (reacting or non-reacting) is at a higher density than the corresponding bulk fluid because of the favorable interactions between the wall and the fluid. However, the pore walls also impose spatial limitations on the fluid mixture and may selectively adsorb some components. For the HI decomposition reaction, the transition state is a smaller molecule than the two independently reacting HI molecules. The density within the

pores is higher than in the bulk phase, and consequently, the contracted transition state structure is energetically favored over the reacting molecules inside the pore.

The density increase within the pore phase accounts for only a fraction of the observed rate increase. This is apparent when the rate constant in the bulk phase and in the pore phase is plotted versus the corresponding density in each phase. The density within the pore phase is calculated using the accessible volume, with the accessible pore width defined as the carbon-center to carbon-center distance minus the Lennard-Jones diameter of a carbon atom: $V_{\text{pore}} = L \times W \times (H - \sigma_C)$. The large increase in the reaction rate constant within a pore of width 1.75 nm, as compared to the bulk phase at the same average density, is shown in Figure 5.10. This suggests that in addition to increasing the reaction rate by the density enhancement, the strong physical interactions with the pore walls tend to favor the formation of the transition state. The same results are seen in the pores of smaller width as well.

At higher pressures the density of the reacting fluid mixture in the pore changes only slightly so that little further effect of confinement is observed, and the rate constant seems to increase at a rate similar to the bulk fluid (see Fig. 5.9). Comparing the pore widths of 1.00 nm and 1.25 nm with the wider pores, one can see a significant increase in the reaction rate. In the 1.00 nm and 1.25 nm wide pores, the size of the $(\text{HI})_2^\ddagger$ molecule is commensurate with the width of the pore and shows a single deep minimum in the potential well. The potential for the HI molecules, by contrast, is divided into two smaller potential wells, with a minimum located against each pore wall. The single, deep

potential well for the transition state tends to favor the formation of the activated complex and leads to significant increases in the reaction rate constant.

Two-phase simulations of the HI decomposition reaction were also performed in bundles of single-walled carbon nanotubes. The nanotubes were modeled using site-site LJ potentials to account for the interaction with the reacting adsorbate molecules, with the LJ parameters for carbon taken from Steele [35]. Two nanotube models were used: (8,8) nanotubes and (10,10) nanotubes, according to the standard convention [36], with diameters of 1.09 nm and 1.36 nm, respectively. The nanotube diameter is defined as the diameter of a circle that passes through the center of the carbon atoms composing the nanotube walls. These individual nanotubes were arranged in a hexagonal array (see Fig 2.1), and adsorption and reaction were allowed within the nanotubes and in the interstitial spaces between the nanotubes. The closest approach of any two carbon centers on neighboring nanotubes is 0.34 nm, the LJ diameter of carbon.

The simulated reaction rate constants for the HI decomposition reaction are shown in Figure 5.11 for the two nanotube bundles. The (8,8) nanotube model shows a particularly strong catalytic effect on this reaction, with a 13 fold increase in the rate constant at a pressure of 1 bar and rising to a factor of 47 at a pressure of 200 bar. The sharp increase in the rate constant found in the (8,8) model is interesting, since the density of reacting molecules within the two nanotube models is very similar. Therefore, it seems that the increased catalytic effect of the (8,8) nanotube is mainly due to the physical interaction with the pore walls that favors the formation of the transition state.

The TS-RxMC simulations have demonstrated that the effect of the microporous support material on the rate of a chemical reaction can be remarkable, and consequently should be an integral part of the design of catalytic support materials. Likewise, Figures 5.9 and 5.11 illustrate that reactions occurring in porous materials can result in much higher reaction rates as compared to the corresponding bulk phase reaction. These molecular simulations suggest strong potential benefits for reducing operational costs as well as eliminating safety concerns of high-pressure processes.

5.5 Discussion

The capacity of substances to enter into chemical reactions is primarily determined by the chemical structure of the reacting molecules, but is also strongly affected by the reacting medium and the experimental conditions. Reaction kinetics under non-ideal conditions can deviate significantly from ideal gas behavior, for example, when reactions occur in nano-sized spaces or under high pressure. At present, however, the nature and direction of the changes imposed by external forces on reaction rate kinetics is unclear. The method presented in this Chapter provides a way to determine the influence of such non-ideal conditions and environments on reaction kinetics in a rather straightforward and efficient manner, using classical Monte Carlo simulations.

Good agreement with experiment [22] was found for the rate constant for the hydrogen iodide decomposition reaction over a range of pressures (1-300 bar). The reaction rate was only moderately affected by the solvents studied. This is to be expected since HI and the transition state

interact only weakly with the solvents. If there was a significant charge separation along the reaction coordinate, we would expect the polarity of the solvent to show more dramatic effects. The most dramatic results were seen for the HI decomposition reaction in slit-shaped carbon pores and in carbon nanotubes. The reaction rate was found to increase by a factor of 47 in the (8,8) nanotubes at a pressure of 200 bar, as compared to the bulk fluid. These simulations illustrate that the effect of confinement and simple fluid-wall "physical" forces on the rate of a chemical reaction can be large, even in the absence of "chemical" catalysis. These fluid-wall interactions can catalyze reactions by increasing the density of the reacting fluid and by enhancing formation of the transition state complex in these confined spaces.

The methodology presented in this Chapter is a Monte Carlo-based approach capable of predicting the rates of reactions that obey the fundamental assumptions of transition-state theory. Reaction rates can be measured in any type of non-ideal environment (within pores, on planar surfaces, ionic liquids, supercritical fluids, *etc.*). A key advantage of the TS-RxMC method over currently available methods for calculating reaction rates is that large reacting systems, containing millions of molecules or more, can be studied in a single simulation. Thus, intermolecular contributions (ideal or non-ideal in nature) are accounted for explicitly within the simulation, and subsequent corrections to account for non-ideal reacting media are not required.

It is important to note that the structure and geometry of the transition state, and the value of the activation energy barrier, must be known before TS-RxMC simulations can be performed. This is not a significant drawback since advances in quantum mechanical methods have provided a great deal of potential energy surface information. In this work, the activation energy barrier is assumed to be constant within the different heterogeneous environments. Likewise, dynamic collision effects as well as any geometric or energetic distortion of the transition state from neighboring or solvent molecules are ignored, which may be important [7]. The consequences of these assumptions are unknown at present and may prove important for certain phenomena, such as the chemisorption of molecules on a surface. Finally, although non-ideal effects influencing reaction rates can be manifested through equilibrium thermodynamic phenomena, the rates of reactions in solution can be limited by the diffusion of the reactant molecules into the solvation shell. It should be noted that because the RxMC is a Monte Carlo method, the TS-RxMC algorithm cannot rigorously investigate these types of diffusion-limited processes.

The method presented here has been derived for bimolecular reactions only. Care is needed in making extensions of the method to unimolecular reactions. In a gas-phase unimolecular reaction at low pressure, a Boltzmann population of transition states (for unimolecular reactions the transition state is the vibrationally excited molecule) cannot be maintained for TST to be valid. Since the TST expression (Eq. (5.1)) assumes an equilibrium population of reactant states, it cannot be applied to

unimolecular reactions at low pressure. In the high pressure region, the Boltzmann population of the transition state is maintained, and TST gives the high-pressure rate constant as:

$$k_{uni,P=\infty}^o = \mathbf{k} \frac{k_B T}{h} \frac{q^\ddagger}{q_1} \exp^{-E^\ddagger / RT} \quad (5.14)$$

Therefore, the TS-RxMC method for unimolecular reactions is limited to applications at higher pressures. However, the calculation of the rate constant could provide insight into the experimentally observed high-pressure rate constant.

Application of TST to gas-phase trimolecular reactions such as the recombination, $A+B+M \rightarrow AB+M$ (where A and B are atoms and M is a molecule) are not possible. The reaction can proceed along a variety of trajectories, and thus no single configuration of A, B and M exists that can be chosen as the transition state. It should be noted that the application of the TS-RxMC method to unimolecular and trimolecular reactions is limited by the assumptions of transition-state theory and not the TS-RxMC methodology. A powerful advantage of the TS-RxMC method, however, is that the simulated system can contain multiple reactions occurring simultaneously. This implies that if complex higher order reactions can be separated into a combination of bimolecular or unimolecular reactions, then the TS-RxMC method could be applied accordingly.

References

- [1] L. D. Gelb, K. E. Gubbins, R. Radhakrishnan, and M. Sliwinska-Bartkowiak, *Reports on Progress in Physics* **62** (1999), 1573.
- [2] C. H. Turner, J. K. Johnson, and K. E. Gubbins, *Journal of Chemical Physics* **114** (2001), 1851.
- [3] C. H. Turner, J. Pikunic, and K. E. Gubbins, *Molecular Physics* **99** (2001), 1991.
- [4] K. Kaneko, N. Fukuzaki, K. Kakei, T. Suzuki, and S. Ozeki, *Langmuir* **5** (1989), 960.
- [5] H. Eyring, *Journal of Chemical Physics* **3** (1935), 107.
- [6] J. K. Johnson, A. Z. Panagiotopoulos, and K. E. Gubbins, *Molecular Physics* **81** (1994), 717.
- [7] R. N. Porter, D. L. Thompson, L. B. Sims, and L. M. Raff, *Journal of the American Chemical Society* **92** (1970), 3208.
- [8] M. G. Evans and M. Polanyi, *Transactions of the Faraday Society* **31** (1935), 875.
- [9] D. Chandler, *Journal of Chemical Physics* **68** (1978), 2959.
- [10] Laidler, K. J., *Theories of Chemical Reaction Rates*, McGraw-Hill, New York, (1969).
- [11] W. R. Smith and M. Lisal, *Physical Review E*, (2002, in press).
- [12] Johnson, J. K., *Advances in Chemical Physics*, edited by Ferguson, D. M., Siepmann, I., and Truhlar, D. G., Wiley: New York **105** (1999), 461.
- [13] M. Lisal, W. R. Smith, and I. Nezbeda, *Journal of Chemical Physics* **113** (2000), 4885.
- [14] M. Borówko and R. Zagórski, *Journal of Chemical Physics* **114** (2001), 5397.
- [15] W. R. Smith and B. Triska, *Journal of Chemical Physics* **100** (1994), 3019.
- [16] M. Lisal, I. Nezbeda, and W. R. Smith, *Journal of Chemical Physics* **110** (1999), 8597.
- [17] M. Lisal, W. R. Smith, and I. Nezbeda, *Journal of Physical Chemistry B* **103** (1999), 10496.
- [18] McQuarrie, D. A., *Statistical Mechanics*, HarperCollins: New York, (1976).

- [19] Hirschfelder, J. O., Curtiss, C. F., and Bird, R. B., *Molecular Theory of Gases and Liquids*, Wiley: New York, (1954).
- [20] W. L. Jorgensen and C. J. Swenson, *Journal of the American Chemical Society* **107** (1985), 569.
- [21] C. J. Cramer and D. G. Truhlar, *Reviews in Computational Chemistry* **6** (1995), 1.
- [22] G. B. Kistiakowsky, *Journal of the American Chemical Society* **50** (1928), 2315.
- [23] C. A. Eckert and M. Boudart, *Chemical Engineering Science* **18** (1963), 144.
- [24] S. C. McGrother and K. E. Gubbins, *Molecular Physics* **97** (1999), 955.
- [25] A. Z. Panagiotopoulos, *Molecular Physics* **62** (1987), 701.
- [26] L. Monchick and E. A. Mason, *Journal of Chemical Physics* **35** (1961), 1676.
- [27] L. M. Raff, L. Stivers, R. N. Porter, D. L. Thompson, and L. B. Sims, *Journal of Chemical Physics* **52** (1970), 3449.
- [28] J. B. Anderson, *Journal of Chemical Physics* **100** (1994), 4253.
- [29] J. M. Prausnitz, *AIChE Journal* **5** (1959), 3.
- [30] Levine, I. N., *Physical Chemistry*, McGraw-Hill: New York, (1988).
- [31] J.-P. Bouanich, *Journal of Quantitative Spectroscopy and Radiative Transfer* **47** (1992), 243.
- [32] J. G. Harris and K. H. Yung, *Journal of Physical Chemistry* **99** (1995), 12021.
- [33] C. S. Murthy, K. Singer, M. L. Klein, and I. R. McDonald, *Molecular Physics* **41** (1980), 1387.
- [34] A. Cheng and W. A. Steele, *Journal of Chemical Physics* **92** (1990), 3858.
- [35] Steele, W. A., *Interaction of Gases with Solid Surfaces*, Pergamon: Oxford, (1974).
- [36] P. M. Ajayan and T. W. Ebbesen, *Reports on Progress in Physics* **60** (1997), 1025.

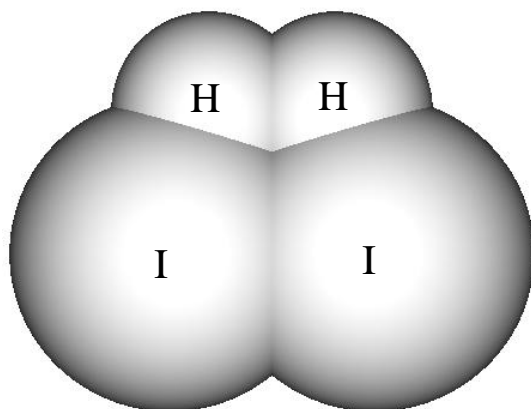


Figure 5.1 Structure of transition state taken from ref. [23].

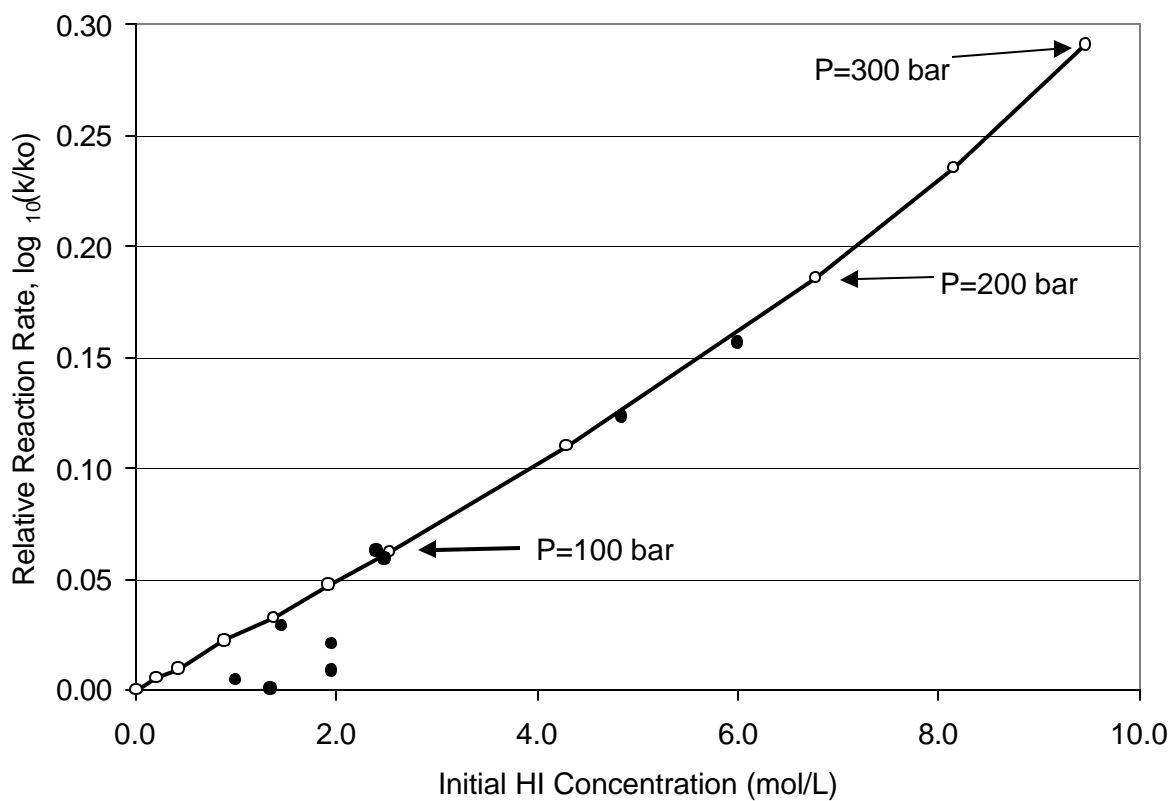


Figure 5.2 TS-RxMC simulations (○) and experimental measurements [22] (●) of the rate constant for the hydrogen iodide decomposition reaction at 573.15 K. The simulated pressure is shown corresponding to different concentrations.

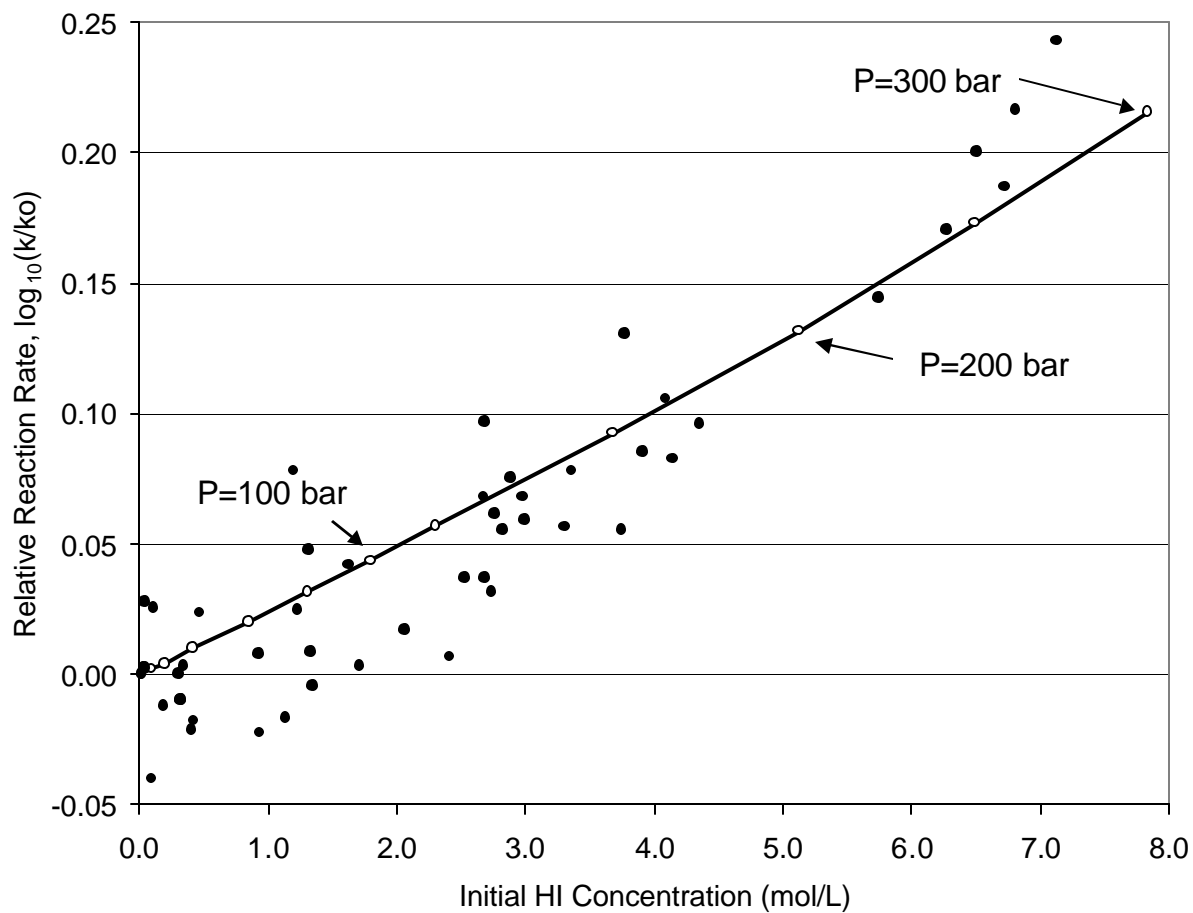


Figure 5.3 TS-RxMC simulations (○) and experimental measurements [22] (●) of the rate constant for the hydrogen iodide decomposition reaction at 594.55 K. The simulated pressure is shown corresponding to different concentrations.

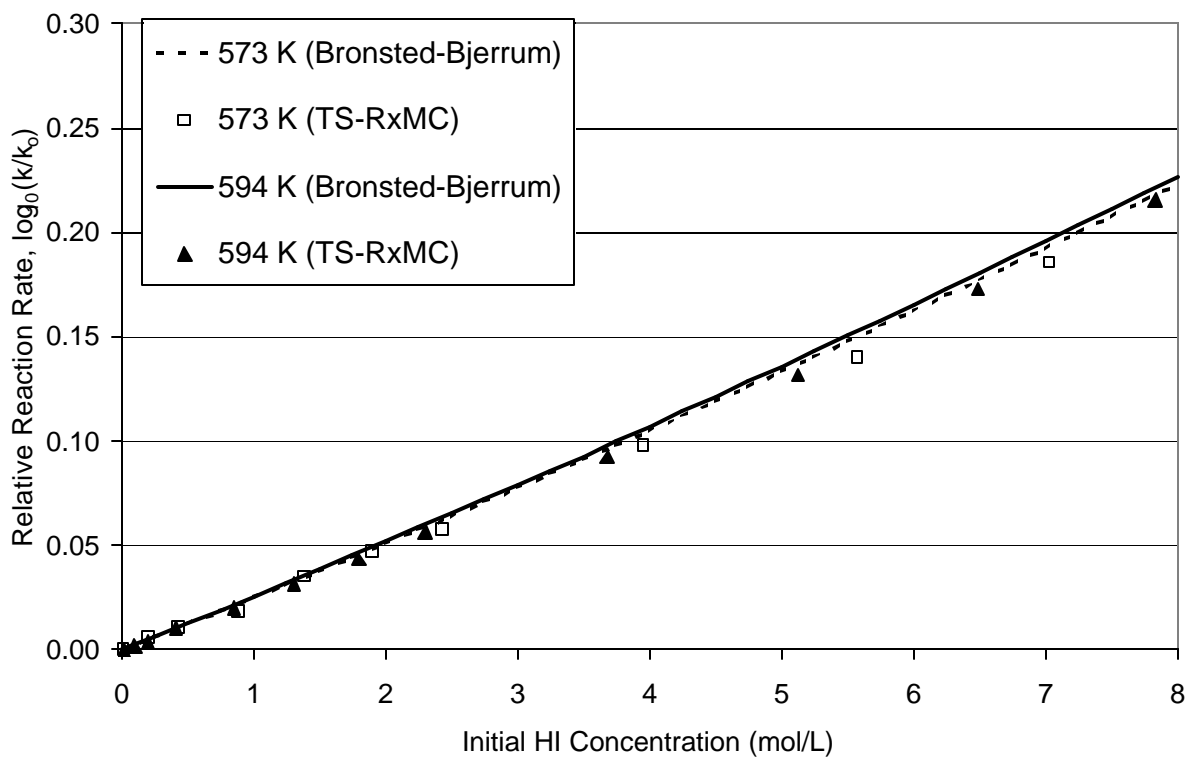


Figure 5.4 Comparison of TS-RxMC simulations with calculations of Eckert and Boudart [23].

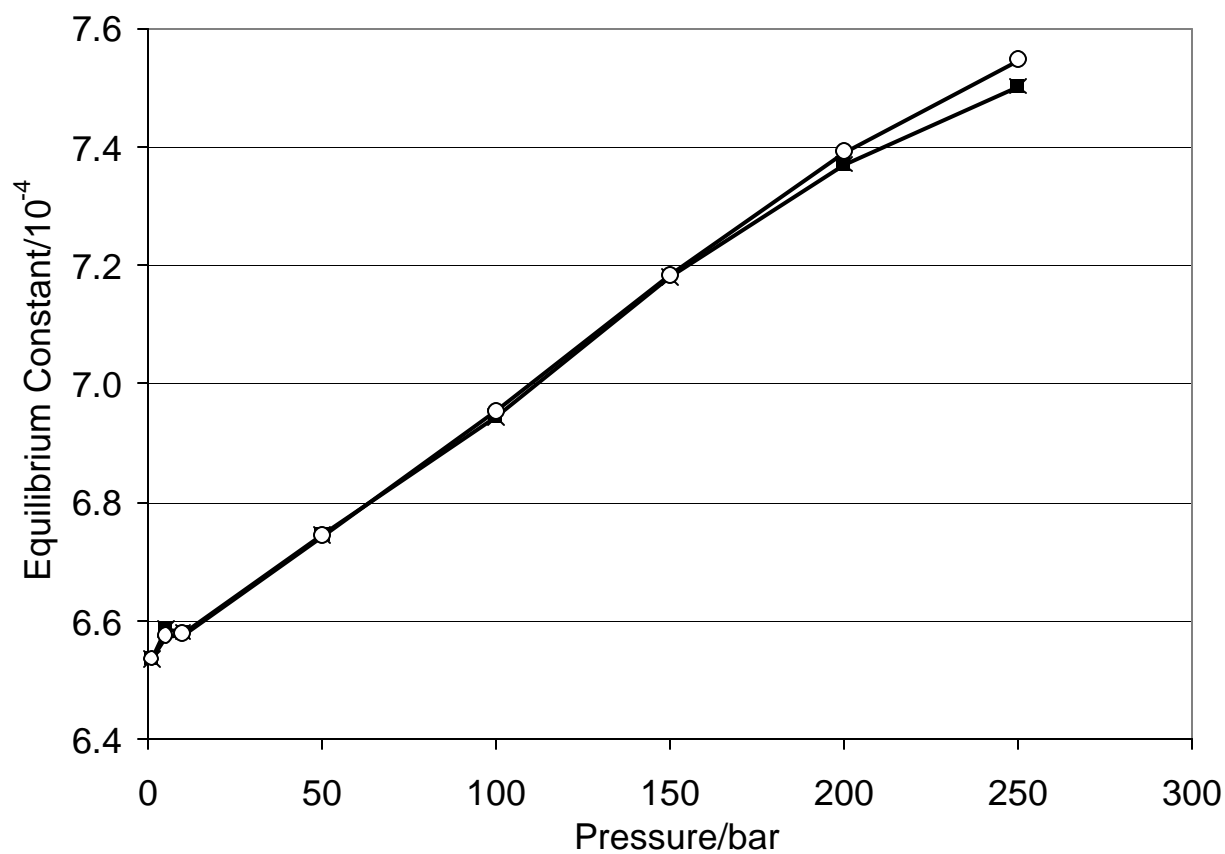


Figure 5.5 Equilibrium constant, K_c , of the HI decomposition reaction at 573.15 K. Results from RxMC equilibrium simulations are represented by \blacksquare , and results from the TS-RxMC kinetic simulations are represented by \circ .

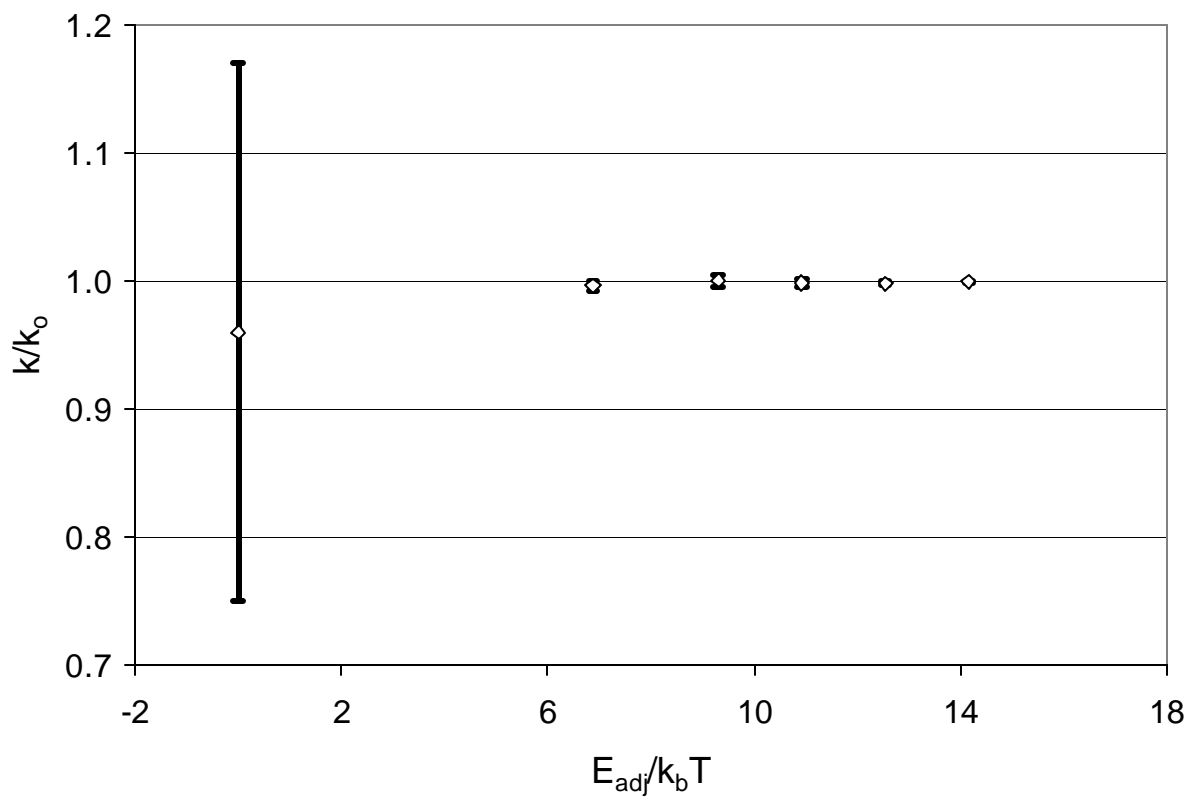


Figure 5.6 Effect of adjusting the activation energy barrier on accuracy of method for the H_2 exchange reaction at 450 K.

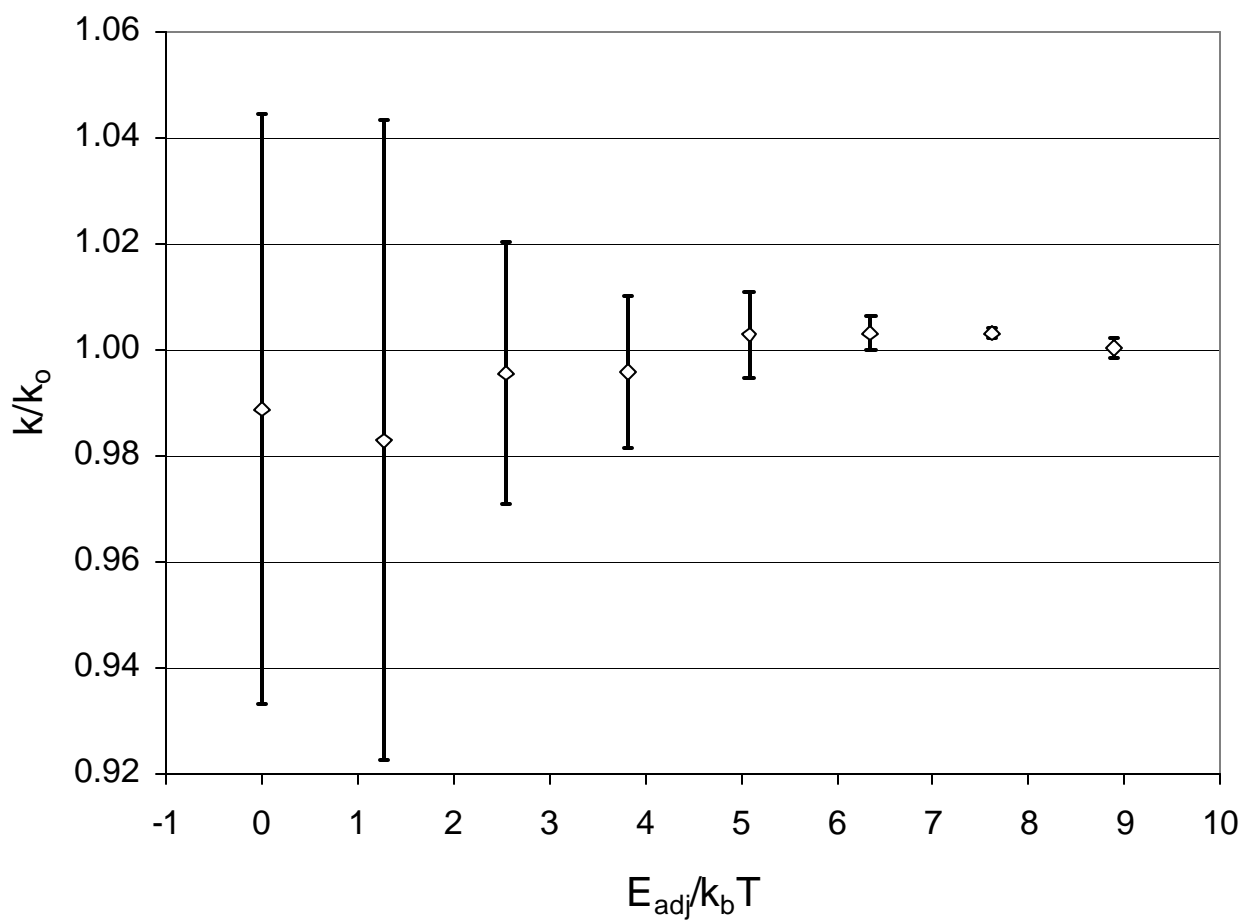


Figure 5.7 Effect of adjusting the activation energy barrier on accuracy of method for the HI decomposition reaction at 573.15 K.

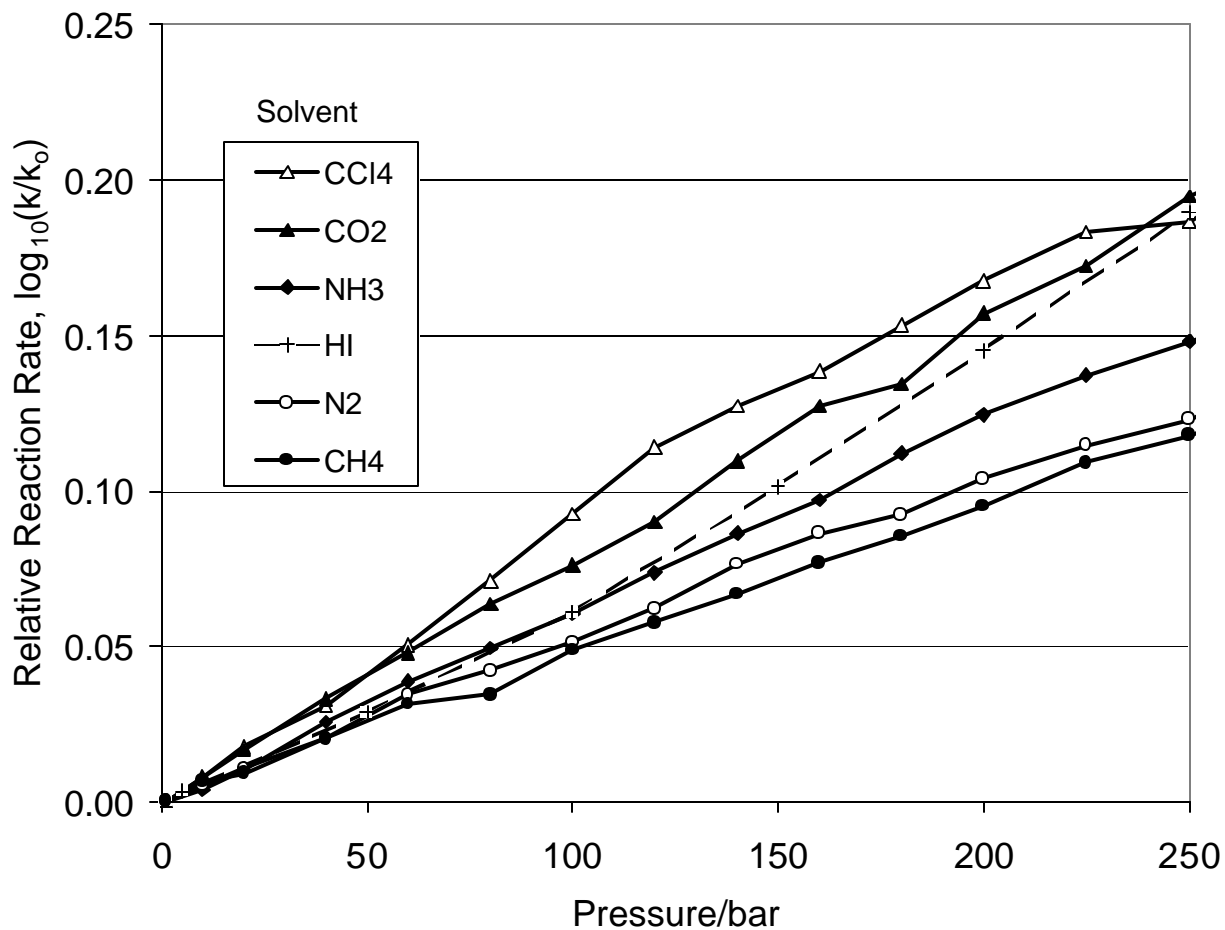


Figure 5.8 TS-RxMC simulations of hydrogen iodide decomposition in different inert solvents. The temperature is 573.15 K. The reaction is retarded by NH₃, N₂, and CH₄, while CO₂ and CCl₄ solvents are predicted to marginally increase the reaction rate constant.

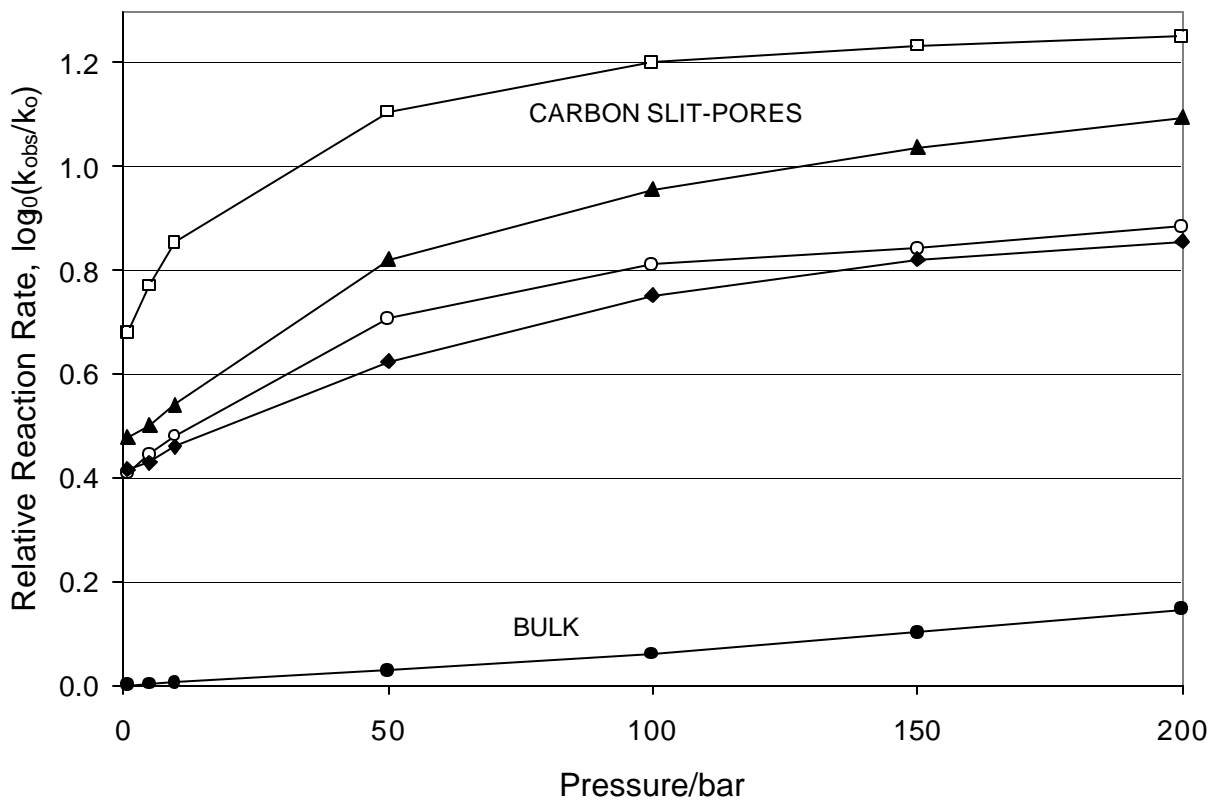


Figure 5.9 TS-RxMC simulations of the hydrogen iodide decomposition rate at 573.15 K in the bulk phase (●) and in carbon micropores of various widths: 1.00nm(□), 1.25nm(▲), 1.50nm(○), and 1.75nm(◆).

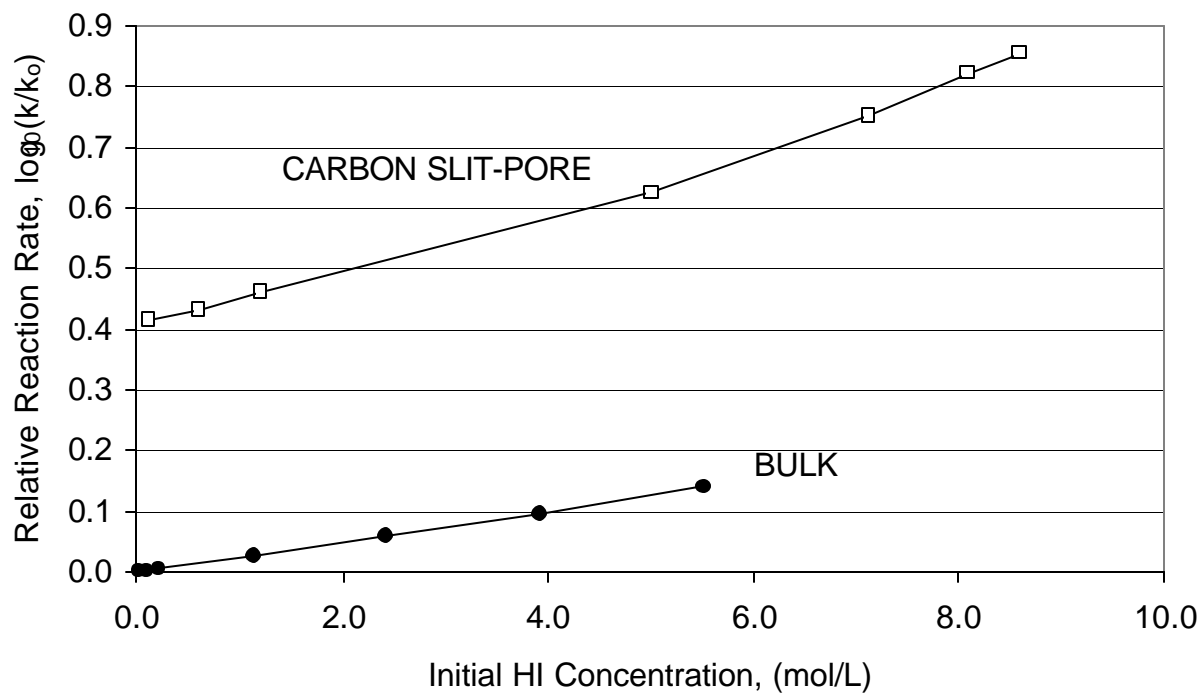


Figure 5.10 TS-RxMC simulations of hydrogen iodide decomposition at 573.15 K in a slit-pore of width $H/nm=1.75$ (\square) and in the bulk phase (\bullet). At equal average densities, physical interactions with the pore walls catalyze the reaction.

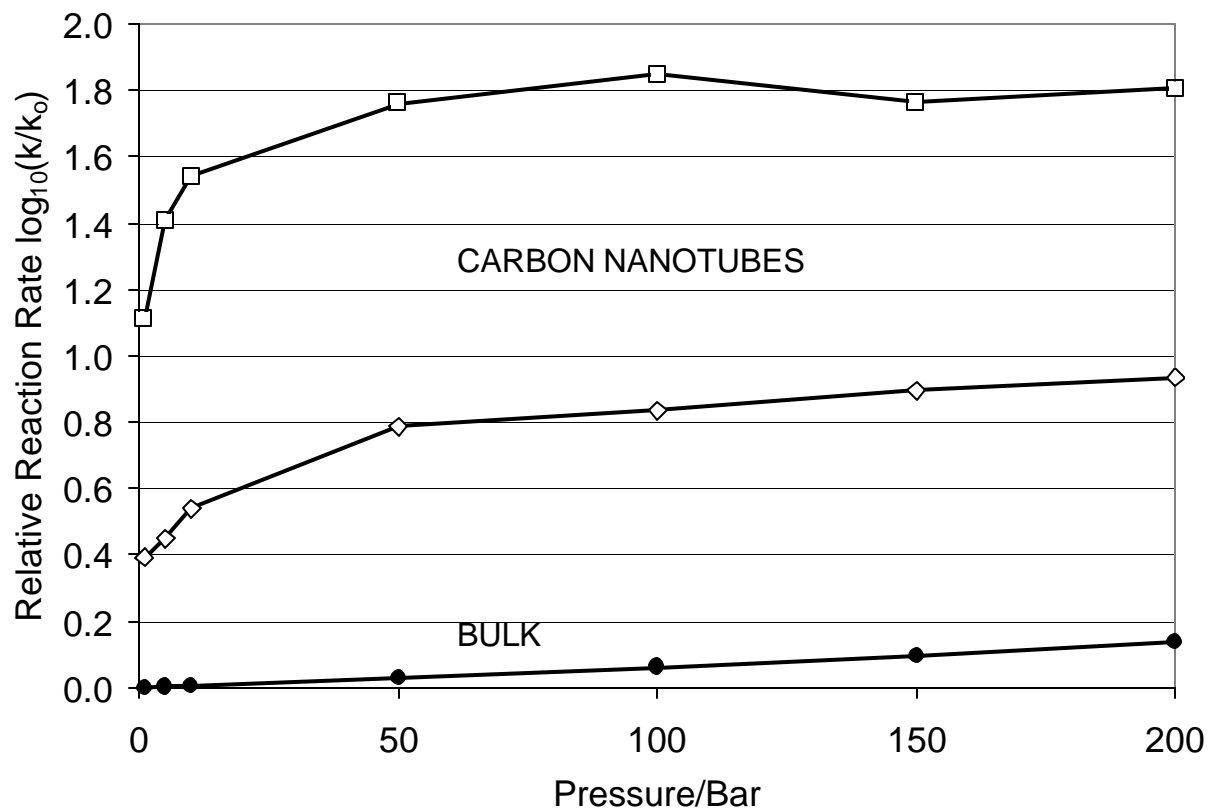


Figure 5.11 TS-RxMC simulations of the hydrogen iodide decomposition rate at 573.15 K in the bulk phase (●) and in carbon nanotubes of different diameter: (8,8) nanotube (□) and (10,10) nanotube (◇).

CHAPTER 6

Conclusions and Future Work

6.1 Reaction Equilibria

We have used Monte Carlo simulations to predict the behavior of chemical reactions within porous materials, where experimental observation is difficult or even impossible. Where experimental comparison is available, we have found qualitative agreement with our simulation results. Our work represents the first attempt at using molecular simulations to predict chemical reaction equilibria and kinetics in confinement, and we have found the effects to be dramatic.

First, we have shown that chemical reaction equilibria within porous carbons can be significantly different from that in the bulk gas or liquid phases. We have shown that nitric oxide dimerization and ammonia synthesis can be enhanced by factors of 40 and 1.6, respectively, when the reaction occurs within carbon pores of 1.0 to 2.0 nm in width. Additionally, we have found that selective adsorption can be an important factor in determining reaction yield within a carbon micropore. This was demonstrated with the ammonia synthesis reaction in a slit-shaped carbon pore, and magnified when active sites (in the form of carboxyl groups) were added to the pore surface. The importance of selective adsorption was also demonstrated with the esterification of acetic acid. The carbon pore slightly enhanced the yield of ethyl acetate, while at the same time

selectively adsorbing this species at a high concentration, revealing a route for efficient product separation and purification.

There are several opportunities for continuing the study of chemical reaction equilibria in confinement. While we have studied only isolated reactions in porous carbons, the behavior of competing or parallel reactions in confinement is relatively unknown and difficult to measure experimentally. Additionally, as mentioned in Chapter 1, enantiomeric separations using confinement has been studied experimentally, but a molecular simulation study of this nature is still lacking. To improve the accuracy and reliability of these reaction equilibria studies, it is important to include a greater amount of molecular detail from *ab initio* studies in porous materials. It is expected that molecular geometry, vibrational frequencies, and bond energies could be distorted within pores, and this possibility should be incorporated within these molecular simulations.

6.2 Reaction Kinetics

A new method has been demonstrated for predicting rate constants within heterogeneous environments, such as microporous carbons. This method was demonstrated to be thermodynamically consistent and accurate for describing the kinetics of hydrogen iodide decomposition. Furthermore, this new method was used to show the significant enhancements in reaction rate possible due to the physical interactions within carbon slit-pores and carbon nanotubes. In the future, the validity of this method could be refined by incorporating dynamic collision effects with the surrounding molecules and the pore

walls, as these effects have been ignored in our study. As with the equilibrium studies, there should be *ab initio* results incorporated within these simulations, in order to describe the change in the molecular structure, energetics, and transition state species within the pore phase.